Detector Contamination Monitoring System for Finnish Radiation Early Warning Network

Msc Thesis, 6.11.2020

Author:

Ville Bogdanoff

Supervisors:

Sakari Ihantola
Radiation and Nuclear Safety Authority (STUK)

Paul Greenlees
University of Jyväskylä, Department of Physics

Tiivistelmä

Bogdanoff, Ville
Detector Contamination Monitoring System for Finnish Radiation Early Warning Network
Pro gradu -tutkielma
Fysiikan laitos, Jyväskylän yliopisto, 2020, 103 sivua

Tässä pro gradu -tutkielmassa kehitettiin ilmaisimen pinnan kontaminaation mittausjärjestelmää Suomen ulkoisen säteilyn valvontaverkon uuden sukupolven säteilymittausaseman gammailmaisimeen. Ydinvoimalaonnettomuuksissa ja ydinräjähdyksissä ilmakehään voi vapautua suuria määriä radioaktiivisia aineita, jotka voivat kiinnittyä gammailmaisimen ulkopinnalle. Pinnalle kiinnittyneet radioaktiiviset aineet voivat aiheuttaa virheellisiä mittaustuloksia. Pintakontaminaation mittausjärjestelmä toteutettiin ohuella muovituikeaineella, jonka avulla ilmaisimen ulkopuolelle kiinnittyneiden radioaktiivisten aineiden lähettämää beetasäteilyä mitattiin ja näin ilmaisimen kontaminaatiotasoa voitiin arvioida. Tässä tutkielmassa kontaminaatiomittausjärjestelmästä kehitettiin kaksi konfiguraatiota ja tutkimuksissa määritettiin kunkin konfiguraation beetasäteilyn havaitsemistehokkuus sekä tutkittiin muovituikesignaalin vaimenemisesta johtuvaa valonkeräystehokkuuden heikentymistä. Lisäksi tutkielmassa demonstroitiin pulssimuotoanalyysitekniikoiden käyttöä tuikesignaalien erottelemiseksi phoswich-tyyppisissä monituikekidejärjestelmissä.

Tutkielmassa ohuella muovituikeaineella havaittiin olevan erittäin hyvä beetasäteilyn havaitsemistehokkuus. Kuitenkin tutkituissa konfiguraatiossa valonkeräys muovituikemateriaalista jäi todella heikoksi, mikä heikensi muovituikesignaalin näkymistä valomonistinputkella. Jatkotutkimuksissa valonkeräystehokkuutta muovituikeaineesta tulisi parantaa, mikäli kontaminaatiomittausjärjestelmä otettaisiin käyttöön Suomen säteilyvalvontaverkossa.

Avainsanat: Muovituikeaine, säteilyvalvontaverkko, radioaktiivinen kontaminaatio, phoswich

Abstract

Bogdanoff, Ville
Detector Contamination Monitoring System for Finnish Radiation Early Warning Network
Master's thesis
Department of Physics, University of Jyväskylä, 2020, 103 pages.

This MSc thesis demonstrated a contamination monitoring system to be installed in the detector of the next generation radiation monitoring stations planned for the Finnish radiation early warning network. Severe nuclear incidents can result in a large-scale release of airborne radioactive contamination, which can be deposited on the outer surfaces of the detector and could falsify the data collected with the gamma-ray detector. The contamination monitoring system was based on using a thin plastic scintillator to measure the beta radiation emitted by the deposited radionuclides. In this thesis, two viable configurations were developed to demonstrate the contamination monitoring system. Experiments were done to determine the beta counting efficiency and light collection of each configuration. As the detector will contain a novel phoswich based gamma-ray detector, pulse shape discrimination techniques were investigated for the separation of scintillation signals.

The thin plastic scintillator was found to be very efficient for detecting beta radiation. Moreover, the demonstrated configurations suffered a tremendous loss of scintillation light and resulted in a weak signal to be measured. A means to improve the light collection efficiency should be researched if the system is incorporated into the detector in the future.

Keywords: Plastic scintillator, radiation early warning network, radioactive contamination, phoswich

Preface

I want to thank Maarit Muikku at Radiation and Nuclear Safety Authority (STUK) for providing me the opportunity to work on this interesting thesis subject and all my great colleagues at STUK for their support and encouragement. I would also like to thank my supervisors Dr. Sakari Ihantola and Prof. Paul Greenlees, for their guidance and productive feedback and the staff at the Helsinki Institute of Physics Detector Laboratory and the University of Jyväskylä, Department of Physics for providing me assistance and services to support this thesis.

Finally, I would like to thank my wife for enduring the absence of me working away from home.

In Helsinki on November 6th 2020

Ville Bogdanoff

Contents

Tiivistelmä **3**

Abstract **5**

Preface **7**

1 Introduction **11**

2 Radiation Early Warning Networks **13**
2.1 Finnish Radiation Early Warning Network 13
2.2 Development of a Next Generation Radiation Monitoring Station . . 15

3 Airborne Radioactive Contamination **17**
3.1 Radionuclide Composition of Contamination 17
3.2 Atmospheric Transport of Airborne Contamination 18
3.3 Deposition of Airborne Radioactive Contamination 20

4 Plastic Scintillators **23**
4.1 Particle Interactions in Plastic Scintillators 23
4.2 Scintillation Mechanism in Plastic Scintillators 26
4.3 Properties of Plastic Scintillators 27
4.4 Light Collection and Scintillation Mounting 30

5 Detector Contamination Monitoring System **35**
5.1 Proposed Configurations 35
5.2 Experimental Set-ups and Research Objectives 37

6 Materials and Methods **39**
6.1 Equipment 39
6.1.1 Scintillating Materials 39
6.1.2 Electronics 41

6.1.3 Radiation Sources 42
6.2 Scintillator Test System 43
6.3 Triple-Layer Phoswich Design 46
6.4 Cylindrical Phoswich Design 47
6.5 Pulse Shape Discrimination 49

7 Measurement Results 53
7.1 Preliminary Studies 53
7.1.1 Time Coincidence Analysis 53
7.1.2 Impact of Reflector Material 56
7.1.3 Impact of Scintillator Polishing 62
7.1.4 Impact of Scintillator Orientation 65
7.2 Studies with the Top Monitoring Configuration 72
7.2.1 Signal Separation Using Pulse Shape Discrimination 72
7.2.2 Impact of the Gamma-ray Detector 80
7.3 Studies with the Side Monitoring Configuration 85
7.3.1 Impact of Scintillator Shaping and Uniformity of Light Collection 85

8 Conclusions 91

References 93

A Python Script for Estimation of the Light Collection Capability 99

B Asymmetric Least Squares Method for Background Subtraction 101

1 Introduction

Radiation Early Warning Networks (REWN) are an essential part of emergency preparedness for nuclear accidents. The Finnish REWN, which was initially established around 60 years ago, has undergone many upgrades over its history, with the most recent modernization having occurred over a decade ago.

At present, due to the aging of equipment in the Finnish REWN, the Radiation and Nuclear Safety Authority in Finland (STUK) has undertaken a strategy of updating and modernizing the Finnish REWN. As part of this strategy, the Monitoring and Situation Assessment Laboratory at STUK has started a research project called DEFACTO (DEtector for Fallout and Air Concentration moniTOring) to develop a novel radiation detector to be installed in the Finnish REWN in the future. This novel detector, in addition to external dose rate monitoring and radionuclide identification, will be capable of differentiating between airborne radioactive contamination and ground contamination, i.e., nuclear fallout. Such information would be crucial for maintaining comprehensive situational awareness during wide-scale nuclear incidents.

Major nuclear incidents such as accidents in nuclear installations or nuclear weapon detonations can result in a widescale spread of airborne radioactive contamination, which can be deposited on the surface of the detector. This surface contamination could compromise the collected data and, in the worst case, weaken the ability of the detector to differentiate between radioactive components. There are three practical means of countering the surface contamination issue. The first method involves ways of measuring the contamination level of the detector. Secondly, deposited radionuclides could be removed physically with various decontamination procedures. The third method consists in inhibiting radioactive substances from depositing the detector by using superhydrophobic coatings.

This thesis focuses on the first method by introducing a contamination monitoring system to be incorporated into the novel detector. With the integrated contamination monitoring system, surface contamination could be measured continuously, leading to more accurate monitoring of external radiation levels.

Most of the radionuclides released in nuclear incidents undergo beta-decay. For

that reason, the contamination levels of the detector can be estimated by measuring the beta radiation emitted from the outer surface of the detector. The contamination monitoring system would be built by equipping the detector with a plastic scintillator, which is highly sensitive for measuring beta radiation, and by making plastic scintillator thin enough, such that the system will have a limited effect on the performance for gamma-ray detection.

Two configurations of the contamination monitoring system is proposed: top-monitoring and side-monitoring configurations. In the top-monitoring configuration, the plastic scintillator is attached on top of the gamma-ray detector, and contamination is measured from the upper surface of the detector through a circular-shaped beta window. In the side-monitoring configuration, the plastic scintillator is wrapped in a hollow cylinder-shape around gamma-ray detector, and contamination is measured from the side surface of the detector through ring-shaped beta windows.

In this thesis, the contamination monitoring system is demonstrated in practice with various test setups. Simple setups, containing only the plastic scintillator and a photomultiplier tube, is used to research the means of improving the performance of plastic scintillator. More complex setups, also including the gamma-ray detector, is built to simulate top-monitoring and side-monitoring configurations. These realistic setups is used to research the possibility of separating three scintillator signals using pulse shape discrimination methods and also to study the impact of the gamma-ray detector on the performance of plastic scintillator.

2 Radiation Early Warning Networks

A Radiation Early Warning Network (REWN) is a nation-wide system of linked stations that measure external radiation levels of the environment. REWN's are used as an early warning tool to detect and warn abnormal levels of atmospheric radioactivity. They are thus an essential part of emergency preparedness for nuclear accidents by providing quantitative and positional information on the spread of radioactive substances. With this data, proper preparedness measures such as emergency evacuation can be directed in affected areas.

REWN's are deployed by several countries around the world, with one of the most extensive networks operated by Germany, with a total of 1800 radiation measuring stations installed [1]. Most REWN stations measure ambient gamma dose rate using Geiger-Muller (GM) detectors. However, there are more sophisticated stations deployed that have spectrometric capabilities for radionuclide identification and air sampling capabilities for detecting trace amounts of airborne radioactive contaminants. REWN's are often fully automated to produce continuous, real-time radiation monitoring data for authorities.

2.1 Finnish Radiation Early Warning Network

The Finnish REWN dates back to the early 1960s when the Cold War was at its peak. Extensive nuclear testing carried out by the Soviet Union at the Novaya Zemlya Test Site, around 1000 kilometers from the Finnish border, raised public concern, which paved the way to the establishment of the nation-wide REWN. The first network contained only a few dozen manually operated monitoring stations and was administrated by Finnish Defence Forces and Ministry of Interior [2], [3].

Before the Chernobyl disaster in 1986, the Finnish REWN had grown to a size consisting of over 400 monitoring stations. While REWN provided valuable data during the Chernobyl accident, it was soon realized that there was a demand for automated radiation monitoring stations. A radiation monitoring network, with continuous monitoring capability and near real-time transmission of data, would be a

valuable tool for maintaining comprehensive situational awareness during wide-scale nuclear incidents.

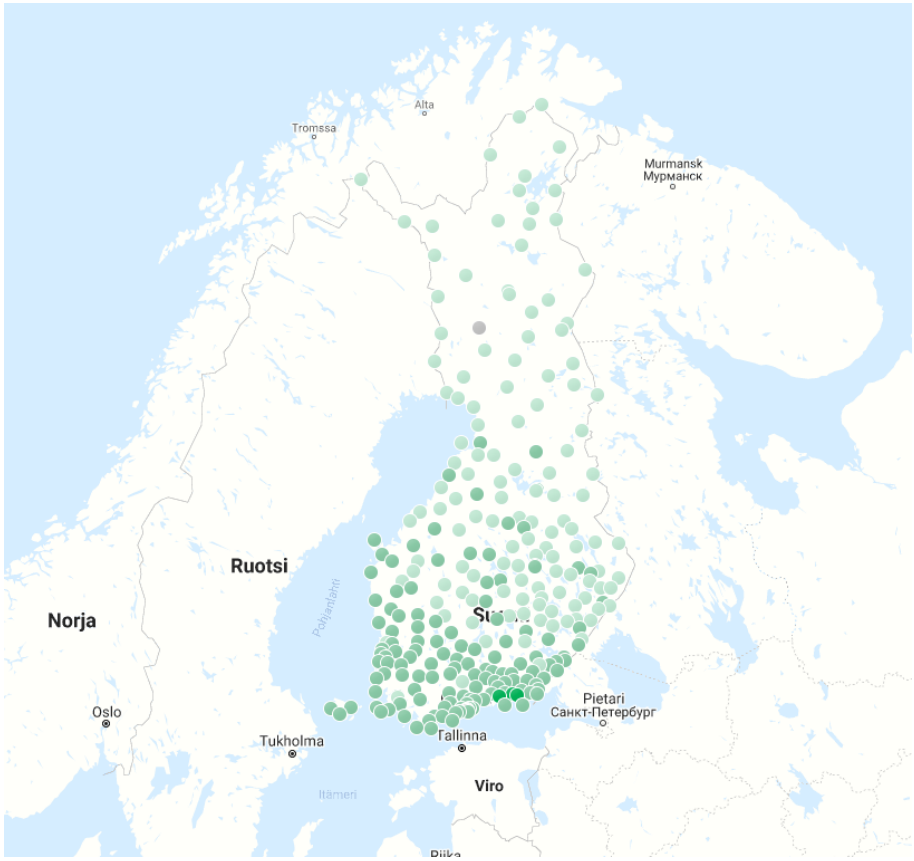

Figure 1. Locations of the radiation monitoring stations in the Finnish REWN [4].

Automatization of the REWN started in the early 1990s. First automated stations were deployed in 1990, and the REWN was fully automated by the year 1999. Today, the Finnish REWN consisting of around 260 monitoring stations (see Fig. 1), is operated by the Radiation and Nuclear Safety Authority (STUK). Each monitoring station has two stationary GM-detectors (one for low dose rate measurement and one for high dose rate) and one portable survey meter for verification purposes. Furthermore, the network includes 20 spectrometric stations equipped with $LaBr_3$ scintillators and eight air sampling stations. Monitoring is performed continuously, and data is transferred in ten-minute intervals to STUK via the VIRVE-network, which is a nation-wide public safety network.

2.2 Development of a Next Generation Radiation Monitoring Station

DEtector for Fallout and Air Concentration moniTOring or DEFACTO is a research project carried out by STUK with the collaboration of Helsinki Institute of Physics (HIP), Instituto de Estructura de la Materia – CSIC, and Finnish Defence Forces (FDF) to modernize the existing Finnish REWN. The primary purpose of the DEFACTO project is to build a prototype detector that could be used to replace outdated sensors in the Finnish REWN. The DEFACTO detector is planned to have the following features:

1. Radionuclide identification
2. Dose rate monitoring
3. Differentiation between airborne radioactive contamination and ground contamination
4. Monitoring of contamination on surfaces of the system
5. Determination of altitude of radioactive release plume passing monitoring station
6. Fully automatic and reliable data collection and processing
7. Compact, low power, cost-effective, and robust device.

The conceptual design of the DEFACTO detector system is shown in Fig. 2. The system will include a phoswich detector, which is a scintillator containing two or more different scintillating materials optically coupled to the same photosensor. By combining scintillation materials with varying decay times, scintillation signals can be separated in a phoswich detector using pulse shape discrimination techniques (discussed more in Section 6.5). With a vertically aligned phoswich detector and carefully placed collimator, the direction from which the detected radiation has come can be estimated: the upper scintillator measures airborne radioactive contamination, and the lower scintillator measures ground contamination.

This thesis focuses on developing a contamination monitoring system for the DEFACTO prototype detector. During severe nuclear and radiation incidents, a

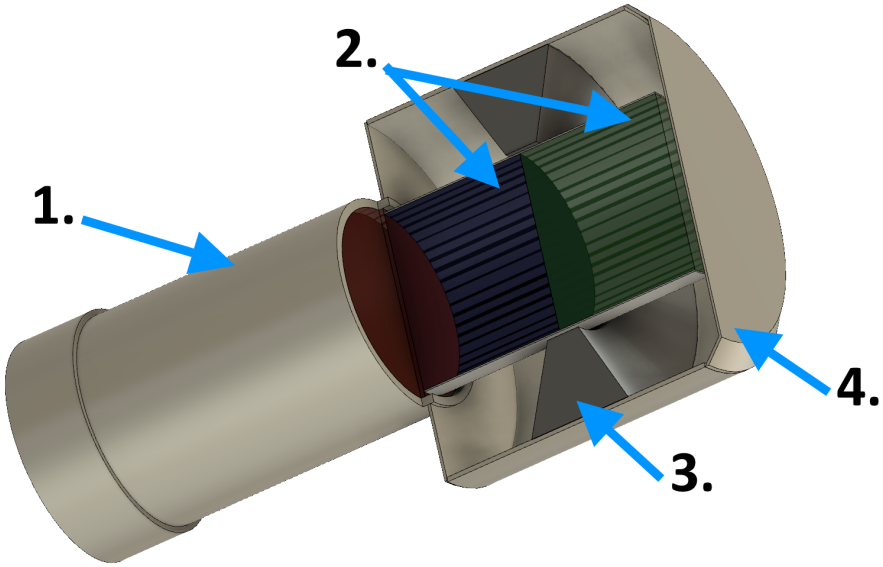

Figure 2. Cross-sectional view of the DEFACTO detector. 1 - Photomultiplier tube and other electronics, 2 - Phoswich scintillator, 3 - Collimator ring, 4 - Detector housing.

significant amount of airborne radioactive contamination can be deposited on the surface of the detector. This surface contamination could substantially weaken the ability of the detector to differentiate between the radioactive components because gamma radiation originating from the surface contamination cannot be separated from the gamma radiation from airborne or ground contamination. By equipping the detector with an integrated contamination monitoring system, surface contamination could be measured continuously, leading to more accurate monitoring of external radiation levels. The contamination monitoring system would also decrease the maintenance workload in the Finnish REWN during the accident because, without such a system, the detector housing would need to be physically decontaminated regularly.

3 Airborne Radioactive Contamination

Airborne radioactive contamination is an undesirable presence of radioactive substances in the atmosphere, which can rapidly spread even on a global scale and present a threat to people and the environment. Airborne radioactive contamination causes radiation doses primarily through inhalation and external irradiation, but also indirectly through the ingestion of contaminated food and drink. Airborne radioactive contamination can also be deposited on surfaces, which can cause problems for instruments measuring the radiation.

The dispersion of airborne radioactive contamination can result from multiple types of incident. The most severe incidents are nuclear power plant accidents and the use of nuclear weapons that can cause a wide-scale spread of airborne contaminants. During the atomic age, there were several nuclear accidents and over 2000 nuclear weapons detonations whose effects can still be detected as elevated levels of radiation in the environment.

Other possible scenarios for more localized dispersion of airborne contamination are an intentional release of radionuclides through conventional explosives (often called a 'Dirty Bomb') and accidents at handling or transporting of radioactive sources. Also, the re-entry of a nuclear-powered satellite can present a significant contamination risk if it crashes in urban areas. At least one such accident has occurred in the past when Soviet reconnaissance satellite Cosmos 954 carrying around 50 kg of ^{235}U failed to boost into planned orbit and crashed into Northern Canada [5].

3.1 Radionuclide Composition of Contamination

Airborne radioactive contamination released in nuclear incidents originates from the fission reaction that is used to create energy in nuclear power plants and nuclear weapons. In the fission process, uranium or plutonium nucleus absorbs a neutron, which excites the compound nucleus into a metastable nuclear isomeric state. This compound nucleus is rapidly broken into lighter elements called fission products. These products are mostly neutron-rich nuclei, which undergo beta minus decay,

where the excess neutron is converted into a proton, an electron, and an electron antineutrino.

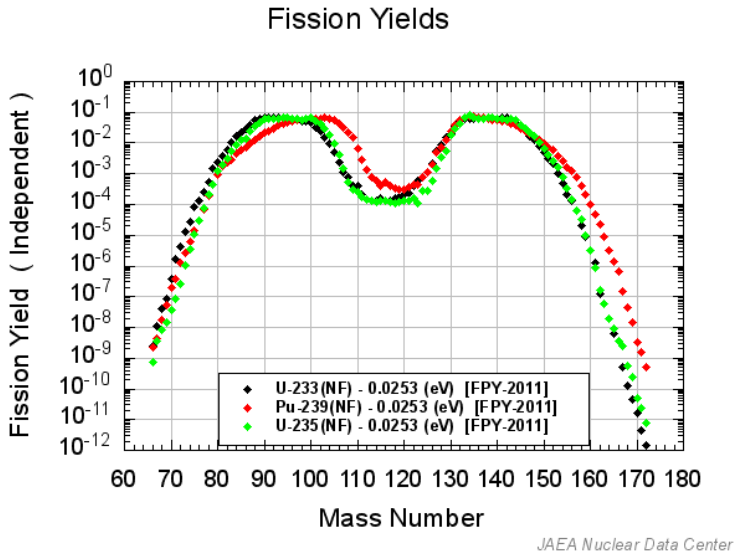

Figure 3. Yields of fission-produced radionuclides of the most common fissile isotopes used in nuclear power plants and nuclear weapons [6].

Fig. 3 depicts the fission product yields of the most commonly used nuclear fuels in fission reactors or nuclear weapons: ^{233}U, ^{235}U, ^{239}Pu. As the figure shows, most probable product yields are in the atomic mass number of 90 to 100 and 130 to 140. Tables 1 and 2 show the most common radionuclides released in the Chernobyl accident and the global nuclear weapons testing combined. As can be seen, most nuclides disintegrate via beta minus decay.

3.2 Atmospheric Transport of Airborne Contamination

Atmospheric transport of airborne radioactive contamination can be divided into dispersion and deposition processes. Dispersion, which refers to the spreading of contamination in the atmosphere, is a complex process that depends primarily on the incident type, atmospheric conditions, and size distribution of released radionuclides.

In severe nuclear reactor accidents, most contamination originates from a nuclear core meltdown in which fission products are vaporized into the atmosphere and can reach a height of a few kilometers. Once vaporized, most of the radionuclides condensate onto the surfaces of natural aerosol particles in the atmosphere. Some

Table 1. Release of radionuclides in the Chernobyl accident [7]

Radionuclide	Half Life	Estimated Release (PBq)	Decay Mode
^{85}Kr	10.72 a	33	β^-
^{133}Xe	5.25 d	6500	β^-
^{131}I	8.04 d	1760	β^-
^{134}Cs	2.06 a	47	β^-
^{137}Cs	30 a	85	β^-
^{89}Sr	50.5 d	115	β^-
^{90}Sr	29.12 a	10	β^-
^{103}Ru	39.3 a	168	β^-
^{106}Ru	368 d	73	β^-
^{95}Zr	64 d	84	β^-
^{239}Np	2.36 d	400	β^-
^{141}Ce	32.5 d	84	β^-
^{144}Ce	284 d	50	β^-
^{238}Pu	87.74 a	0.015	α
^{239}Pu	24065 a	0.013	α

Table 2. Global release of radionuclides in atmospheric nuclear testing [7]

Radionuclide	Half Life	Estimated Release (PBq)	Decay Mode
^{3}H	12.33 a	186	β^-
^{54}Mn	312.2 d	3.98	β^+
^{55}Fe	2.73 a	1.53	EC
^{89}Sr	50.6 d	117	β^-
^{90}Sr	29.12 a	0.622	β^-
^{91}Y	58.5 d	120	β^-
^{95}Zr	64 d	148	β^-
^{103}Ru	39.3 a	247	β^-
^{106}Ru	368 d	12.2	β^-
^{131}I	8.04 d	675	β^-
^{5137}Ce	30 a	0.948	β^-
^{140}Ba	12.75 d	759	β^-
^{141}Ce	32.5 d	263	β^-
^{144}Ce	284 d	30.7	β^-

radionuclides in airborne radioactive contamination are in a gaseous form such as noble gases ^{85}Kr and ^{133}Xe. ^{131}I can be in both forms: gaseous and aerosol.

In nuclear weapon detonations, the level of airborne radioactive contamination depends on detonation altitude. In air bursts, which happen at high altitudes, minimal fallout is formed, but it can reach a height of tens of kilometers and thus can spread on a global scale [8]. However, most fallout is formed in ground bursts, which happen on or near the ground. In ground bursts, the ground material is vaporized and drawn into the cloud, where the material is contaminated with fission products or is activated by neutron flux. The resulting nuclear fallout has a relatively large size distribution of contamination particles and thus is more localized than in air bursts.

In addition to the incident type, dispersion of airborne contamination is also influenced by the prevailing atmospheric conditions, mainly by wind speed and direction, but also through temperature variations.

Lastly, the range of airborne contamination is ultimately governed by the size distribution of aerosol particles, which affects the vertical movement of contamination in the atmosphere. Downward movement of contamination is governed mainly by gravitational settling and Brownian motion, which is the random motion of particles due to collisions with other particles. The gravitational settling velocity depends on the particle size distribution: more massive particles descend faster, and thus their range is shorter. As for smaller particles, their vertical movement is primarily governed by Brownian motion, which enables a more extended range for contamination.

3.3 Deposition of Airborne Radioactive Contamination

Deposition is the process of removal of airborne radioactive contamination from the atmosphere to ground or other surfaces. Deposition can be divided into wet deposition and dry deposition. Wet deposition is a process where the airborne radioactive contamination is dissolved in rain, snow, or fog droplets and is then brought down to the ground by precipitation. If contaminated rainwater or snow is accumulated on the surface of the detector in an radiation early warning network, it can cause significant contamination levels, especially on the upper surface of the detector and could compromise the collected data. However, rainwater can also wash the deposited contamination from the surface of the detector.

Dry deposition is the accumulation of airborne radioactive contamination in

dry weather due to various mechanisms, including gravitational sedimentation, Brownian or turbulent diffusion, impaction, electrostatic forces, and thermodiffusion. The dry deposition mechanism is highly dependant on the aerodynamic diameter of the particle: for aerosol particles with a diameter below 1 µm, Brownian or turbulent diffusion is the primary deposition mechanism. For particles of a few µm impaction starts to dominate, and gravitational sedimentation is the primary deposition mechanism for particles sized over 10 µm. Build-up of static electric discharge on electronic devices can facilitate deposition of airborne contamination, especially with the 0.1 to 1 µm sized aerosol particles [9].

During the Chernobyl accident, most radioactive aerosol particles reaching Finland had a diameter of less than 1 µm [9, p. 61], and therefore diffusion was the primary dry deposition mechanism. For contamination of a detector in a radiation early warning network, diffusion would cause evenly contaminated surfaces of the detector. However, if the nuclear incident were to occur closer to Finland, the size of the contamination particles would be larger, which would increase the likelihood that deposition would happen by gravitational sedimentation. Gravitational sedimentation would result in uneven contamination of the detector, with the top of the detector receiving more contamination than the sides of the detector. For this reason, the detector surface contamination might be more reasonable to measure from the top surface of the detector.

4 Plastic Scintillators

Scintillators are a group of materials that are used in the detection of ionizing radiation. When the ionizing radiation interacts with scintillator, it produces a brief emission of light called scintillation. Scintillator materials are commonly grouped into two main categories: inorganic and organic. Inorganic scintillators cover a wide variety of materials ranging from noble gases to glasses and alkali halides, such as sodium iodide (NaI) and cesium iodide (CsI).

Organic scintillator crystals are aromatic hydrocarbons which consist of varying numbers of benzene rings. Pure organic scintillators are rarely used, but they are usually dissolved into liquid solvents to form liquid scintillators. Organic scintillators can also be solved into polymer bases to form plastic scintillators (PS), which can be molded into different shapes and sizes. Typical organic crystals used in PS are 2-phenyl-5-(4-biphenylyl)-1,3,4-oxadiazole (PBD), p-terphenyl (PPP), and 1,4-di-(5-phenyl-2-oxazolyl)-benzene (POPOP), and the most common polymer base materials are polystyrene, and polyvinyl toluene (PVT) [10, p. 164].

4.1 Particle Interactions in Plastic Scintillators

Plastic scintillators can be used for the detection of ionizing photon radiation as well as charged particles and fast neutrons. The interaction of charged particles in contrast to photons, is based on different interaction modes in plastic: charged particles interact directly via Coulomb forces while photons mainly interact via photoelectric effect, Compton scattering, and pair production. The photoelectric effect takes place when an incident photon interacts with material transferring all of its energy to an inner shell electron of the target atom. This energy transfer leads to the emission of photoelectrons in which the kinetic energy is equal to incident photon energy minus electron binding energy.

In contrast to the photoelectric effect, in Compton scattering, the incident photon only partly transfers energy to a loosely bound outer shell electron resulting in an ejected electron and scattered photon. In pair production, an incident photon is

converted into an electron-positron pair and is the dominant mode of interaction for high energy photons. Fig. 4 shows the dominant interaction mode for different photon energies and atomic number (Z) of absorbers. As the figure depicts, in materials with low Z-number such as plastics, pair production is only possible with photon energies over 40 MeV. In the photon energy range of 50 keV to 10 MeV that is relevant for this thesis, the most significant interaction is Compton scattering.

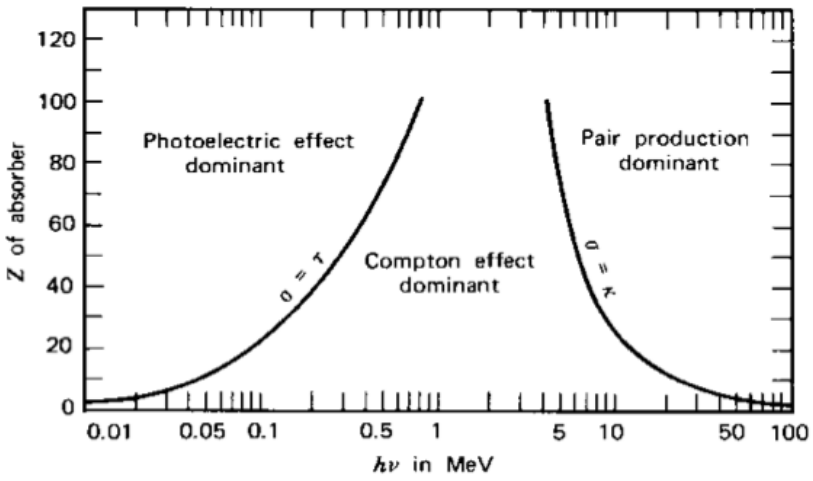

Figure 4. Gamma-ray interaction modes for different photon energies and the atomic number of absorber material. From Ref. [11]

In this thesis, the focus is on the detection of charged particles, more exclusively electrons using a plastic scintillator. Electrons interact via Coulomb forces in the plastic scintillator. Interactions can be divided into elastic and inelastic interactions: Elastic interactions take place when electrons interact with the atomic nucleus via Coulomb forces and deviate from the incident path without losing a significant amount of its energy. Backscattering is a form of elastic interaction where the path of electrons is deviated back towards the incident direction due to Coulomb forces between the particle and electrons in the matter. The probability of backscattering is dependant on electron energy, the atomic number of incident matter, and the angle between beam and incident surface. Regarding the detector contamination monitoring system, some of the incident electrons are backscattered from the beta window and reflector, reducing the number of particles that can be detected in the scintillator. Therefore, backscattering must be taken into consideration with the final design of the detector contamination monitoring system.

In inelastic interactions, electrons lose their kinetic energy in collisions with

atomic electrons. Due to collisions with objects of equal masses, electrons lose a significant amount of energy in every collision and thus follow a zig-zag path inside matter. An equation theorized by Bethe [12] can be used to calculate collisional energy loss per unit length for electrons:

$$-\left(\frac{dE}{dx}\right)_c = \frac{2\pi e^4 NZ}{m_0 v^2}\left(\ln\frac{m_0 v^2 E}{2I^2(1-\beta^2)} - (\ln 2)\left(2\sqrt{1-\beta^2} - 1 + \beta^2\right) + (1-\beta^2) + \frac{1}{8}\left(1-\sqrt{1-\beta^2}\right)^2\right) \tag{1}$$

where N and Z are number density and the atomic number of matter, $\beta = v/c$, E m_0, e, and v are electron energy, rest mass, charge, and velocity, and I is the average excitation and ionization potential of the absorber.

In addition to collisional energy loss, a small amount of energy is lost in the form of bremsstrahlung, the electromagnetic radiation produced by the deceleration of electrons. This radiative energy loss is a result of the theory that any charged particle will radiate energy when being decelerated either by magnitude or orientation. The amount of bremsstrahlung is dependant on the atomic number of matter and energy of the electron. Equation described by Seltzer and Berger [13] can be used to calculate radiative energy loss:

$$-\left(\frac{dE}{dx}\right)_r = \frac{NEZ(Z+1)e^4}{137 m_0^2 c^4}\left(4\ln\frac{2E}{m_0 c^2} - \frac{4}{3}\right) \tag{2}$$

Total energy loss or stopping power for electrons is a combination of both collisional and radiative losses:

$$\frac{dE}{dx} = \left(\frac{dE}{dx}\right)_c + \left(\frac{dE}{dx}\right)_r \tag{3}$$

Using the above equation and integrating inverse of total stopping power with respect to energy, we can plot electron CSDA (continuous-slowing-down approximation) range in the plastic scintillator. CSDA range is the average path length that charged particle travels in the matter while depositing all its kinetic energy. For PVT based plastic scintillator, the CSDA range in the function of electron energy is depicted in Fig. 5. From the plot, we can estimate of the maximum energy deposited

by an electron in 1 mm of PVT, which is about 335 keV. By knowing the maximum energy deposited, we can now say that electrons with kinetic energy below 335 keV are entirely stopped in 1 mm of PS. Above that energy, particles can penetrate through.

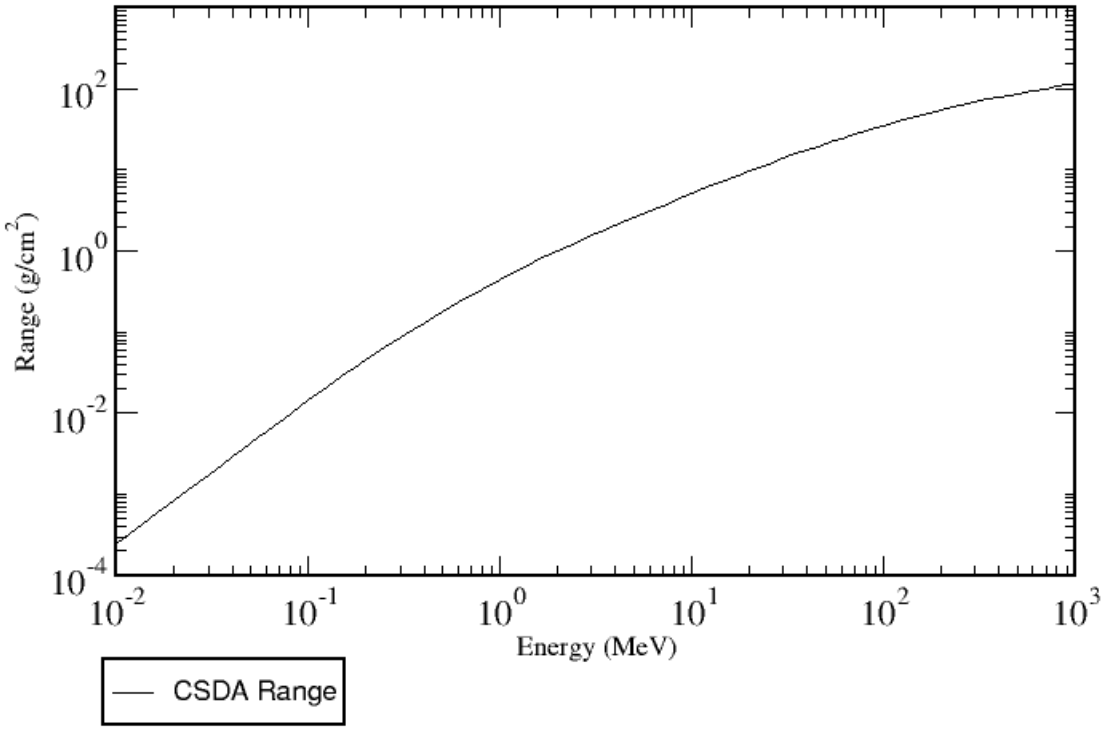

Figure 5. Electron CSDA range in the PVT-based plastic scintillator plotted against the electron energy. From Ref. [14]

4.2 Scintillation Mechanism in Plastic Scintillators

The scintillation mechanism in plastic scintillators is based on the process of fluorescence, a phenomenon where matter first absorbs radiation and then emits light. Fluorescence in plastic scintillators is a result of molecular electronic transitions in the pi-electron structure of an organic scintillation molecule. An example of the pi-electron structure of an organic molecule is shown in the Jablonski diagram in Fig. 6. Pi-electrons are electrons that form pi-bonds, a covalent chemical bond of two overlapping p-orbitals. Pi-electrons, while usually in the ground state at room temperature, can be excited into a higher energy state. The energy needed for this excitation or transition comes from the interaction of a pi-electron and an

incident photon or charged particle. The transition usually occurs between singlet states, where electron spins are paired, i.e., has the opposite spin between excited and ground state. Rarer are transitions between singlet and triplet states, where electron spins are parallel. Singlet to triplet transitions lead to a change in electronic state, where only forbidden transitions are available. Forbidden transitions progress at a lower rate, and therefore the electron can remain in the excited state for a more extended period leading to prolonged emission of light, which is a phenomenon called phosphorescence. The lifetime of a phosphorescent transition can be as much as 10^{-3} seconds as compared to the lifetime of the fluorescent transition of few nanoseconds [11, p. 224-225].

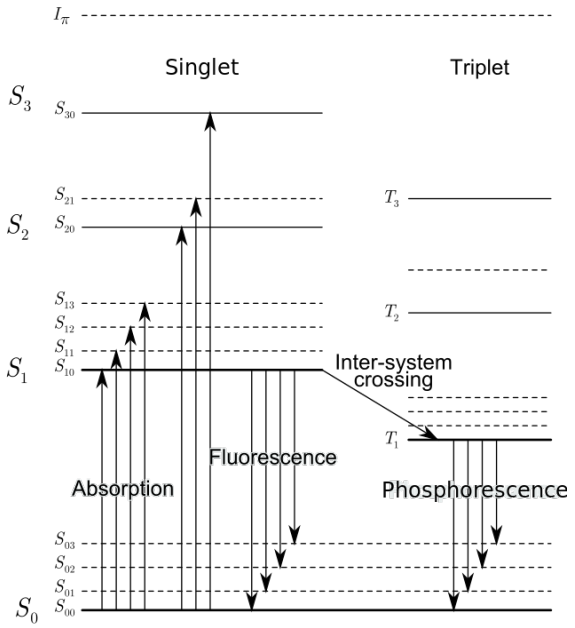

Figure 6. Example of Jablonski diagram showing the pi-electron structure of an arbitrary organic molecule. From Ref. [11]

4.3 Properties of Plastic Scintillators

Plastic scintillators have inferior light yield compared to inorganic scintillators. Light yield or light output indicates how many photons are created in the scintillator per energy unit equivalent of the incident particle. For example, the light yield of Eljen EJ-212 PS used in this thesis is 10000 photons per 1 MeV electron equivalent 3. In contrast, for typical NaI(Tl) scintillator, the light yield is approximately 45000 photons per MeV electron equivalent [15]. The relative energy resolution of

scintillators can be roughly estimated to be proportional to the square root of its light yield. Thus, the relative energy resolution of PS is around two times lower than NaI(Tl).

Despite lower light yield, plastic scintillators have several desired properties. One of the most important properties of plastic scintillators is its easy processing and shaping. Plastic scintillators can be shaped in any form and can even be made as paint to be easily applied to surfaces. Also, plastic scintillators generally feature a rapid signal decay time, which is usually in the range of several hundred picoseconds to a few nanoseconds. The signal decay time is the time of transition from excited singlet or triplet state to the ground state. Because of the fast decay time, plastic scintillators are an ideal choice to be combined with an inorganic scintillator that has a slow decay time. The variation of decay times enables the separation of scintillation signals using Pulse Shape Discrimination (PSD) techniques, discussed more in Section 6.5. Last but not least, plastic scintillators are very cheap compared to some inorganic scintillation materials.

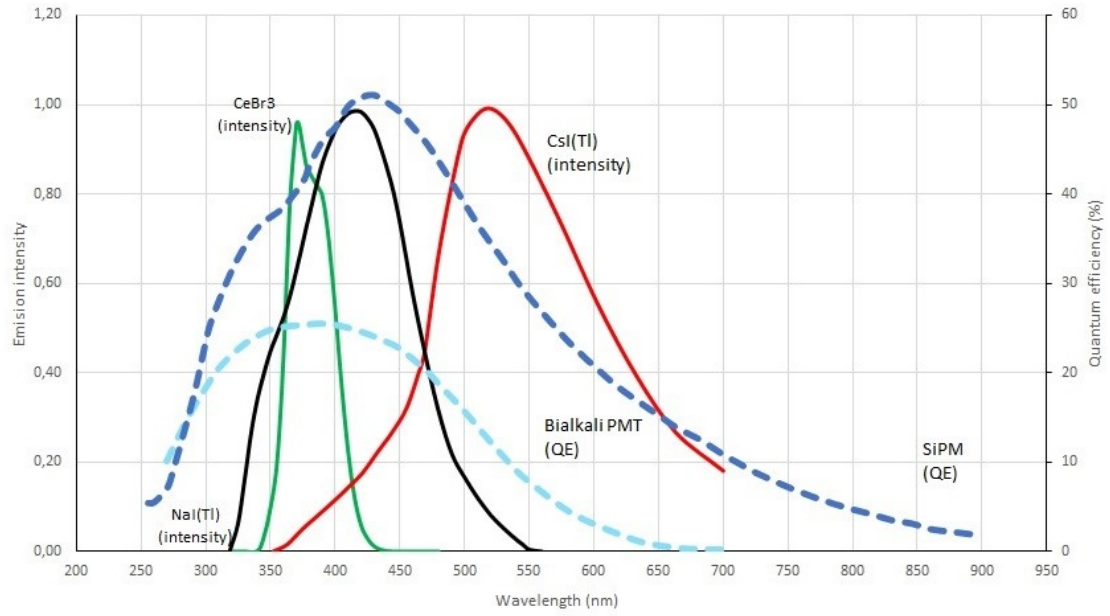

Figure 7. Emission spectrums of NaI(Tl), CsI(Tl), and $CeBr_3$ scintillators and spectral responses of bi-alkali PMT and Silicon photomultiplier (SiPM) versus wavelength [16].

When designing a scintillator detector, it is vital to verify that the emission spectrum of the scintillator used matches the spectral response of photosensor, which depends primarily on the photocathode material. Fig. 7 shows examples of emission

spectra of a few inorganic scintillators versus response spectrum of commonly used bi-alkali photocathode material. As we can see from the figure, the emission spectrum of NaI(Tl) and $CeBr_3$ matches closely with the spectral response of bi-alkali PMT. At the same time, CsI(Tl) does not provide a good match.

While plastic scintillators, in general, can be used to detect ionizing photon radiation, the efficiency to detect photons depends strongly on the thickness of the used PS and the incident photon energy. Fig. 8 shows the photon intensity (compared to the incident intensity) in PVT-based plastic scintillator as a function of penetration depth for different photon energies. As the figure depicts, photon intensity decreases exponentially as the penetration depth increases. For thin PS (thickness less than a few mm), photons are not attenuated considerably, meaning that thin PS are rather insensitive to ionizing photon radiation.

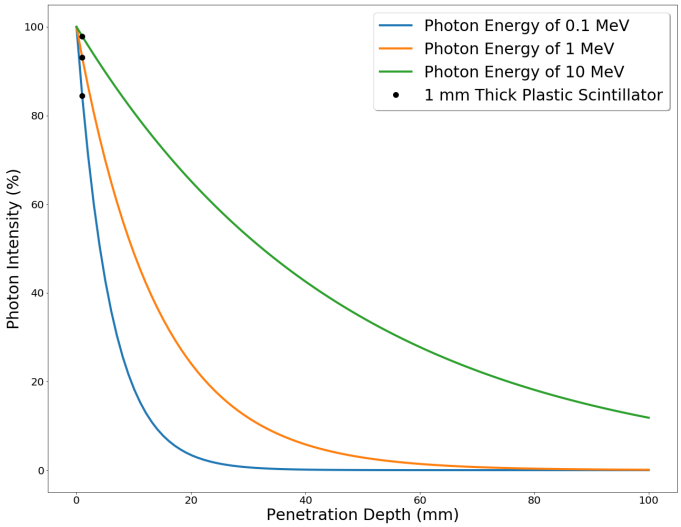

Figure 8. Photon intensity in PVT based plastic scintillator plotted against the penetration depth for different photon energies. Values calculated using NIST XCOM: Photon Cross Sections Database [17].

4.4 Light Collection and Scintillation Mounting

This section discusses the principles of light propagation inside scintillators, methods to improve light collection and procedures for mounting scintillators on photomultiplier tubes.

When assembling a scintillator system, the goal is to maximize the light collection efficiency to the photosensor and minimize spatial variations in light collection efficiency. Light can be lost inside the scintillator in two ways: first, light can leave scintillator from its surfaces, i.e., transmitted light. Second, light can be absorbed in the scintillating material. The self-absorption of light will start to dominate with large scintillators but can be neglected with the size of the plastic scintillator used in this thesis.

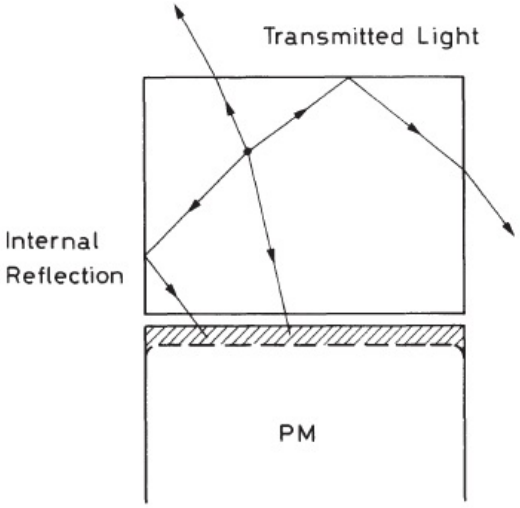

Figure 9. Principles of the light collection in the scintillator system. From Ref. [10].

Fig. 9 shows principles of the light collection in the scintillator system. A simple way to prevent transmitted light is to increase the internal reflection of light inside the scintillator. The internal reflection, which is depicted in Fig. 10, is a process whereby the light will undergo both reflection and transmission upon encountering the interface between two media with different refractive indexes. The amount of reflected and transmitted light depends on the refractive indexes of the media and angle of incidence, which is the angle between the light beam and the normal to the interface. When the angle of incidence is greater than the critical angle, the light will

undergo total internal reflection, meaning that the transmission component vanishes, and all light is reflected internally.

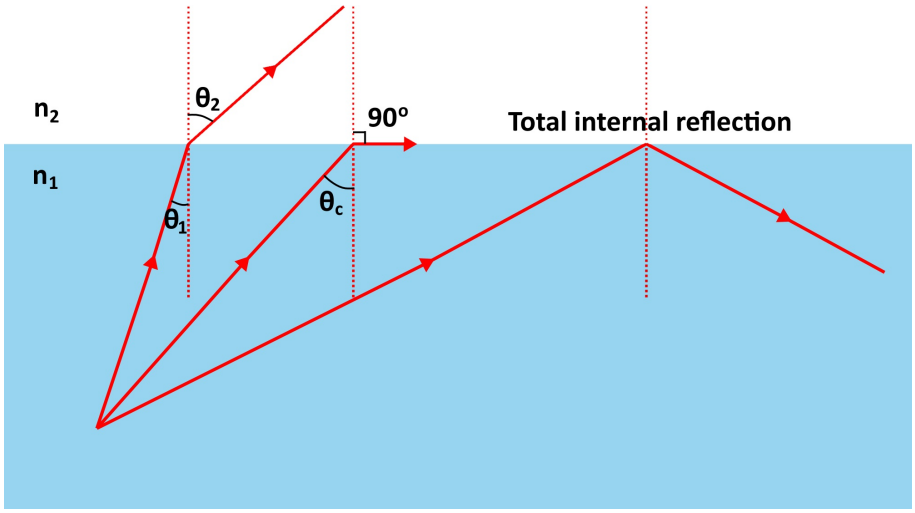

Figure 10. Process of internal reflection of light that is propagating from the scintillator (higher refractive index n_2) to the medium of lower refractive index n_1.

The equation for the critical angle can be derived from Snell's law:

$$\frac{\sin\theta_1}{n_1} = \frac{\sin\theta_2}{n_2} \tag{4}$$

where n_1 and n_2 are refractive indices of the media, and θ_1 and θ_2 are angles of incidence and refraction. As we can see from Fig. 10, the maximum angle of refraction is 90°. By setting the maximum angle of refraction and solving equation (4) for the critical angle θ_c, will result in the following equation:

$$\theta_c = \arcsin\frac{n_2}{n_1} \tag{5}$$

Internal reflection can be increased by decreasing the critical angle. As we can see from equation (5), the critical angle depends only on refractive indexes n_1 and n_2 of the media. Thus, the critical angle could be minimized by surrounding the scintillator with air, which has a refractive index of around 1. Internal reflection can also be increased by polishing surfaces of the scintillator. Rough surfaces tend to scatter internally reflected light and therefore reduce the probability for light to go in the direction of the PMT window. With polished surfaces, internal reflections are more mirror-like and thus will maintain the direction of propagation.

Even with completely smooth surfaces, the transmission of light through surfaces cannot entirely be prevented. Therefore, reflectors are used to direct transmitted light back towards the scintillator. Fig. 11 shows the principle of using reflectors to increase the light collection of the scintillator system. Two types of reflective materials are used in scintillators: specular reflectors and diffuse reflectors. Diffuse reflectors are usually oxide or dioxide (titanium, magnesium, or aluminum) containing paints or powders that are applied directly to surfaces of the scintillator. Also, Teflon (PTFE) tape is often used as a diffuse reflector. Diffuse reflectors reflect light by following Lambert's cosine law and are independent of the angle of incidence:

$$\frac{dI}{d\theta} \propto \cos\theta \tag{6}$$

where I is the intensity of reflected light and θ angle of reflection with respect to the normal of the surface.

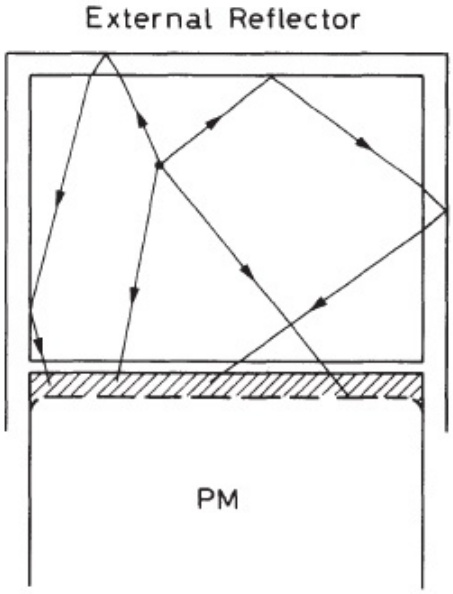

Figure 11. Effect of an external reflector on light collection in the scintillator system. From Ref. [10].

Specular reflectors reflect light, so that angle of reflection equals the angle of incidence, i.e., mirror-like reflections. Specular reflectors can be made from metalized thin films, such as aluminized Mylar, but simple aluminum foil can be used as a specular reflector as well. Diffuse reflectors are generally more efficient than specular

ones [10, p. 201]. However, when working with thin PS, it is recommended to use specular reflectors instead of diffuse reflectors [18].

In contrast to other edges of the scintillator, the scintillator edge facing the photosensor must be allowed to have maximum light transmission. If there is a layer of air between the PMT and the scintillator, internal reflection will prevent most of the light from reaching the photocathode. Thus, optical contact between the photosensor and the plastic scintillator should be made with a transparent material that has a similar index of refraction to that of the plastic scintillator and the PMT window (typical index of refraction of about 1.5). Therefore, optical grease with an index of refraction of 1.5 is commonly used.

5 Detector Contamination Monitoring System

In this section, the concept of the detector contamination monitoring system is introduced for the DEFACTO detector. The DEFACTO detector, which is presented in more detail in Section 2.2, can differentiate the airborne radioactive component from the radioactive fallout component. However, during severe nuclear and radiation incidents, significant amounts of airborne radioactive contamination can be deposited on the surface of the detector. The gamma radiation originating from this surface contamination may be falsely categorized as airborne.

As was described in Section 3.1, most radionuclides released in nuclear incidents undergo beta decay. Therefore, the surface contamination level could be estimated by measuring the beta radiation that originates from the surface of the detector. By default, the DEFACTO detector is not designed to measure beta radiation. However, beta radiation measurement capability could be implemented in the detector by utilizing a thin plastic scintillator.

5.1 Proposed Configurations

Two configurations of contamination monitoring systems were studied in this thesis: a top monitoring system and a side monitoring system. The conceptual design of the top monitoring configuration is shown in Fig. 12. The top monitoring configuration features a thin plastic scintillator stacked horizontally on top of the phoswich scintillator package. In the top monitoring system, the detector surface contamination is measured from the top of the detector through a circular-shaped beta window.

The second configuration, the side monitoring system, is presented in Fig. 13. The system features a hollow cylinder of plastic scintillator that is wrapped around the phoswich scintillator package. In the side monitoring configuration, surface contamination is measured from sides of the detector through two separate ring-shaped beta windows, which are placed above and below the collimator ring.

In both configurations, surface contamination is measured through beta windows,

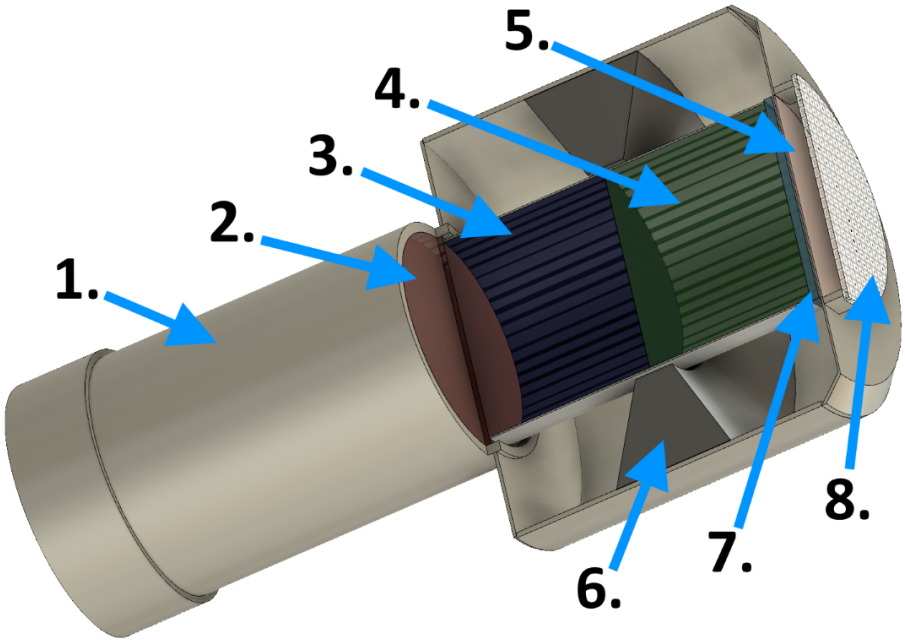

Figure 12. Cross-sectional view of the proposed top monitoring configuration. 1 - PMT, 2 - Photocathode, 3 - CsI(Na) scintillator, 4 - NaI(Tl) scintillator, 5 - Beta window, 6 - Collimator ring, 7 - Plastic scintillator, 8 - Protective grid.

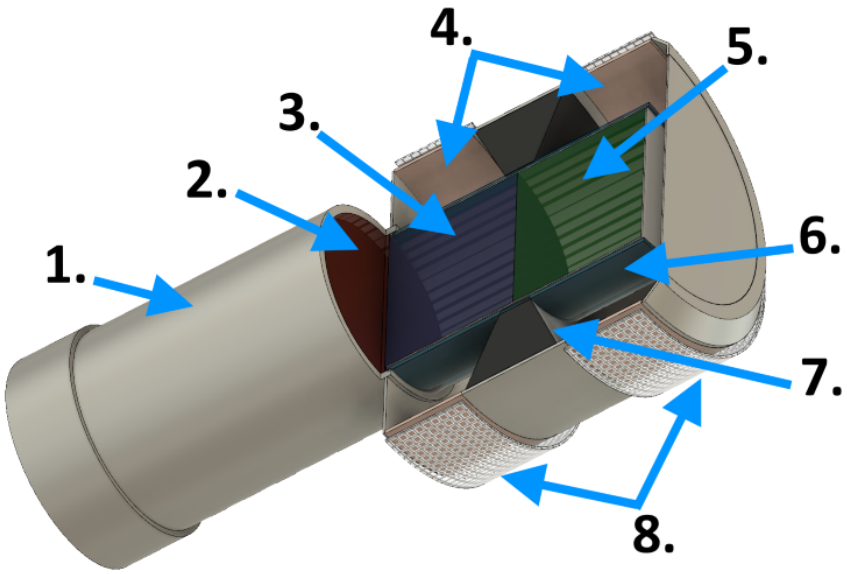

Figure 13. Cross-sectional view of the proposed side monitoring configuration. 1 - PMT, 2 - Photocathode, 3 - CsI(Na) scintillator, 4 - Beta windows, 5 - NaI(Tl) scintillator, 6 - Plastic scintillator, 7 - Collimator ring, 8 - Protective grid.

which have a small surface area compared to the whole detector. However, as described in Section 3.2, airborne radioactive contamination released in nuclear incidents tends to deposit evenly on surfaces. Therefore, by measuring the surface contamination from the small area of the detector, we could estimate the total surface contamination by scaling the measured contamination level with the total surface area of the detector.

As for beta windows, there are particular requirements for the selection of material and design. In general, the beta window should be made thin enough so that the beta particles will undergo little or no attenuation while penetrating the window. On the other hand, the beta window has to be thick enough to withstand outdoor conditions, such as precipitation, icing, corrosion, UV light, and impact of sharp objects, such as tree branches or birds. Depending on the final design of the DEFACTO detector, the beta window should also be gas-tight and possibly light-tight. Different beta window materials were not tested in this thesis.

5.2 Experimental Set-ups and Research Objectives

To investigating the feasibility of top and side monitoring configurations, three experimental set-ups were built for this thesis. The first set-up, the scintillator test system, is a simple set-up featuring a small piece of plastic scintillator mounted directly onto a PMT. Two versions of the simple system were built: horizontal set-up and vertical set-up, which are described in detail in Section 6.2

With the scintillator test system, three objectives were studied. The first objective was to study the impact of specular reflector material on the beta detection efficiency and light collection. Two materials were chosen for this experiment: aluminized Mylar with a thickness of 12 µm, and standard aluminum foil with a thickness of 16 µm. Both materials had their pros and cons: Mylar is composed mostly of plastic with a thin layer of aluminum and, therefore, will cause less energy loss for beta particles with less bremsstrahlung and smaller probability for backscattering. However, the Mylar cover is not fully light-tight and will result in a small loss of scintillation light. Also, Mylar is quite elastic, which makes it more difficult to wrap around objects. As with aluminum foil, it is thicker, denser, and has a higher atomic number than Mylar and will thus result in more substantial energy loss for beta particles and also generate more bremsstrahlung and electron backscattering. On the other hand, aluminum was completely light-tight and was easier to wrap around objects.

The second objective was to test the impact of scintillator polishing on the beta detection efficiency and light collection. The PS used in this thesis was received as a large sheet that was pre-polished in the factory. However, in our experimental setups, smaller pieces of PS were needed, and therefore we used a utility knife to cut a larger sheet of PS into smaller pieces. The edges contained a significant amount of surface roughness, which decrease the internal reflection of light, as was described in Section 4.4. A scintillator polishing procedure will significantly remove surface roughness and should, therefore, improve light collection.

The third objective was to test the impact of the orientation of the plastic scintillator on the beta detection efficiency and light collection. Orientation in this context means whether the PS is mounted to the PMT window through its knife-cut thin face (vertical orientation) or front/back face (horizontal orientation). The orientation is relevant when using thin PS because vertical mounting results in a drastic decrease of the surface to PMT area when compared to horizontally mounted PS. For example, in the scintillator test system, the surface to PMT area in vertical and horizontal set-ups was 60 mm^2 and 576 mm^2, respectively. This tenfold difference in surface to PMT area should have an impact on light collection efficiency.

The second set-up, a triple-layer phoswich design, which is described in Section 6.3, is an experimental version of the top monitoring configuration of the detector contamination monitoring system. The first objective of this set-up was to determine whether the signal separation between three different scintillation signals using pulse shape discrimination techniques (described in Section 6.5) is feasible. The second objective was to study how the inorganic crystals reduce the beta detection efficiency and light collection of the PS when placed as a triple-layer phoswich.

The third set-up, a cylindrical phoswich design, which is described in Section 6.4, was built as an experimental version of the side monitoring configuration of the detector contamination monitoring system. The first objective of this set-up was to test the effect of shaping (heat treating and bending) of the PS on the beta detection efficiency. The second objective was to test the uniformity of light collection in the PS.

6 Materials and Methods

Three different experimental set-ups were built for this thesis to test the contamination monitoring system. In this section, all three set-ups are presented in detail and how they were assembled is presented. We also describe the materials and equipment used in the measurements and illustrate the method of pulse shape discrimination for signal separation.

6.1 Equipment

6.1.1 Scintillating Materials

Three different scintillating materials are used in this thesis: polyvinyl toluene (PVT) based plastic scintillator (PS), thallium-activated sodium iodide (NaI(Tl)), and sodium-activated cesium iodide (CsI(Na)). The main emphasis is on PS, which is used as a beta counter in the detector contamination monitoring system. For this purpose, Eljen EJ-212 PS, which is produced by Eljen Technology, was deemed to be most suitable. EJ-212 is a general-purpose plastic scintillator that is specially designed to be used in thin sheets. It has a relatively large light yield of 10000 photons per MeVee (electron equivalent) and a high light attenuation length of 250 cm. However, EJ-212 can also be made in thicker sheets to be used in beta spectroscopy or as a detector for gamma rays. As we are interested only in beta detection purposes, and we also want to minimize gamma-ray interactions, EJ-212 PS with 1 mm thickness was ideal. Also, the emission spectrum of EJ-212 PS was suitable for our needs. With a peak emission wavelength of 423 nm, EJ-212 PS can be used with standard blue-sensitive bi-alkali photomultiplier tubes (PMT) and with inorganic NaI(Tl) and CsI(Na) scintillators. The specifications for EJ-212 PS are given in Tab. 3.

In contrast to PS, inorganic NaI(Tl) and CsI(Na) scintillators were used mainly to function as a gamma-ray detector in the triple-layer and cylindrical phoswich designs. For NaI(Tl) and CsI(Na) scintillators, we used the Scionix 25C25-CN-X10 model, for which specifications are given in Tab. 4 and Tab. 5. Both scintillators feature a

Table 3. Specifications for Eljen E-212 Plastic Scintillator [19].

Physical and Scintillation Constants	
Polymer Base	Polyvinyltoluene
Refractive Index	1.58
Light Yield, photons/MeV e^-	10000
Light Output, % Anthracene	65
Wavelenght of Max. Emission, nm	423
Rise Time, ns	0.9
Decay Time, ns	2.4
Pulse Width, FWHM, ns	2.7
Density, $g\,cm^{-3}$	1.023
Softening Point, °C	75
Light Output vs. Temperature	At 60 °C, L.O. = 95% of that at 20 °C. No change from 20 °C to −60 °C

cylindrical crystal with a diameter and a height of 25 mm. Because both crystals are hygroscopic (material that absorbs moisture from the surrounding environment), they were hermetically sealed with an aluminum container that has optical windows on both ends. The peak emission wavelength of NaI(Tl) is 415 nm vs. 420 nm for CsI(Na), which matches the spectral response of blue-sensitive bi-alkali PMT, and the emission spectrum of EJ-212 PS. Therefore, EJ-212 PS, NaI(Tl) and CsI(Na) can be used together as phoswich scintillator.

Table 4. Specifications for Scionix NaI(Tl) scintillator

Physical and Scintillation Constants	
Scintillation Material	Sodium Iodide (Thallium Activated)
Optical Window Thickness, mm	3
Crystal Diameter, mm	25
Crystal Height, mm	25
Wavelenght of Max. Emission, nm	415
Light Yield, photons/keVγ	38
Decay Time, ns	230
Density, $g\,cm^{-3}$	3.67
Hygroscopic	Yes

Table 5. Specifications for Scionix CsI(Na) scintillator

Physical and Scintillation Constants	
Scintillation Material	Cesium Iodide (Sodium Activated)
Optical Window Thickness, mm	3
Crystal Diameter, mm	25
Crystal Height, mm	25
Wavelenght of Max. Emission, nm	420
Light Yield, photons/keVγ	41
Decay Time, ns	630
Density, g cm^{-3}	4.51
Hygroscopic	Yes

6.1.2 Electronics

The main electronics used in measurements are a photomultiplier tube (PMT), PMT base, high voltage (HV) power supply, and digitizer. As for the photomultiplier tube, the Hamamatsu model R6231-100 PMT was used. The R6231-100 is a head-on type PMT with a 2-inch (51 mm) diameter tube size. The tube has eight dynode stages providing a typical anode gain of 2.7 x 10^5 and features super bialkali photocathode material with a borosilicate glass PMT window. Borosilicate glass provides the full transmittance of radiation from 350 nm to infrared and thus matches the emission light of the scintillators used. Super bialkali photocathode features a similar spectral response than bialkali photocathode (shown in Fig. 7) but enables significantly better quantum efficiency [20, p. 15]. Specifications of the Hamamatsu R6231-100 PMT are given in Table 6.

Table 6. Specifications for Hamamatsu R6231-100 PMT [21]

Properties	
Type	Head-on
Tube Size, ∅mm	51
Photocathode Area Size, ∅mm	46
Photocathode Material	Super Bialkali
Window Material	Borosilicate glass
Dynode Structure	Box and grid + Linear focused
Dynode Stages	8
Typical Dark Current, nA	2
Typical Anode Gain	2.7 x 10^5

The PMT was connected to the Hamamatsu E1198-27 PMT base, which functions

as a voltage divider for the PMT dynodes. The Hamamatsu E1198-27 is a D-type socket assembly that can be used for PMT's of diameter 51 mm to 76 mm and has maximum input voltage toleration of 1500 V (positive polarity).

High voltage for the PMT was supplied by a CAEN model DT5533E desktop power supply module, which has four HV output channels with two positive and negative polarities. The DT5533E can provide a maximum of four kV output voltage and three mA output current with four-watt maximum power. In measurements (see Section 7), the PMT was connected to the power supply using safe high voltage (SHV) coaxial cable, and the power supply was remotely controlled with a PC using CAEN GECO2020 control software.

For pulse height and pulse shape analysis, the CAEN model DT5730 desktop digitizer was used. The DT5730 has eight analog input channels with 50 Ω impedance and a USB interface for remote control. Analog to digital conversion is performed using a 14-bit flash ADC with a sampling rate of 500 Mega samples per second, which is equivalent to 2 ns per sample. Because the sampling rate is faster than the signal decay time of Eljen EJ-212 PS used in this thesis (2.4 ns), the DT5730 digitizer is well suited for reading the signal that comes from such a PS. In measurements (see Section 7), the PMT was connected to the digitizer using micro coaxial connector (MCX) cable, and digitizer was operated with CAEN CoMPASS data aqcuisition (DAQ) software. The output data given by the CAEN digitizer is in list-mode data format with the following entries: energies, channel numbers, times and pulse integration times.

6.1.3 Radiation Sources

In testing of the contamination monitoring system, deposited detector surface contamination was simulated using the following radioactive sources: ^{90}Sr, ^{137}Cs, ^{133}Ba, ^{207}Bi, for which activity calibration data are given in Tab. 7. The sources were unsealed calibration disk sources, in which radioactive the substance was protected with a thin Mylar film. ^{90}Sr was used as a pure beta emitter in the testing of light collection efficiencies of different measurement set-ups. ^{133}Ba, ^{137}Cs, and ^{207}Bi are regularly used conversion electron sources that emit distinguishable monoenergetic electrons. Internal conversion is a competing process with gamma-ray emission where emitted gamma-ray interacts with an inner electron (usually but not exclusively from K shell) of same nuclide resulting in ejected electron called conversion electron. Next,

an electron from a higher energy level replaces the void left by the ejected electron. This transition results in an x-ray photon, which is emitted at the same time with a conversion electron.

Table 7. Activity calibration data for radioactive sources used in studies

Radionuclide	Activity (Bq)	Reference Date
^{90}Sr	859.4	04/02/2003
^{133}Ba	281000	07/2002
^{137}Cs	281000	07/2002
^{207}Bi	397000	12/15/2008

6.2 Scintillator Test System

The beta detection efficiency and light collection of the thin plastic scintillator (PS) was first tested using a simple system. Two versions of the simple system were built: a horizontal set-up and a vertical set-up, which are depicted in Fig. 14 and Fig. 15 respectively. As the figures show, the difference between set-ups is the placement of PS on the PMT window: in the horizontal set-up, PS is coupled parallel with the window whereas in the vertical set-up, PS is placed perpendicularly to window. Also, the size of PS is different between set-ups with 1 mm x 24 mm x 24 mm in horizontal set-up vs. 1 mm x 40 mm x 60 mm in the vertical set-up.

Both systems are composed of Eljen EJ-212 PS with a thickness of 1 mm, a Hamamatsu R6231-01 model photomultiplier tube (PMT), and a Hamamatsu E1198-27 D-Type Socket Assembly base, which were introduced in Section 6.1. High voltage for the photomultiplier was supplied with a CAEN model DT5533E high voltage power supply, and data acquisition was made using a CAEN model DT5730 Digitizer. No preamplifiers or amplifiers were used in systems.

A plastic case to seal the PMT from ambient light was custom made for the scintillator test system. The case was 3D modeled using Autodesk Fusion 360 CAD design software and was subsequently 3D printed with an Ultimaker 3 printing device using black PLA (polylactic acid) thermoplastic polymer. The case had a wall thickness of at least 2 mm to prevent ambient light from reaching the PMT through the walls. Black wrapping tape was used to cover the seams of the case to ensure maximum light-tightness. The cap was made large enough to fit radiation sources inside.

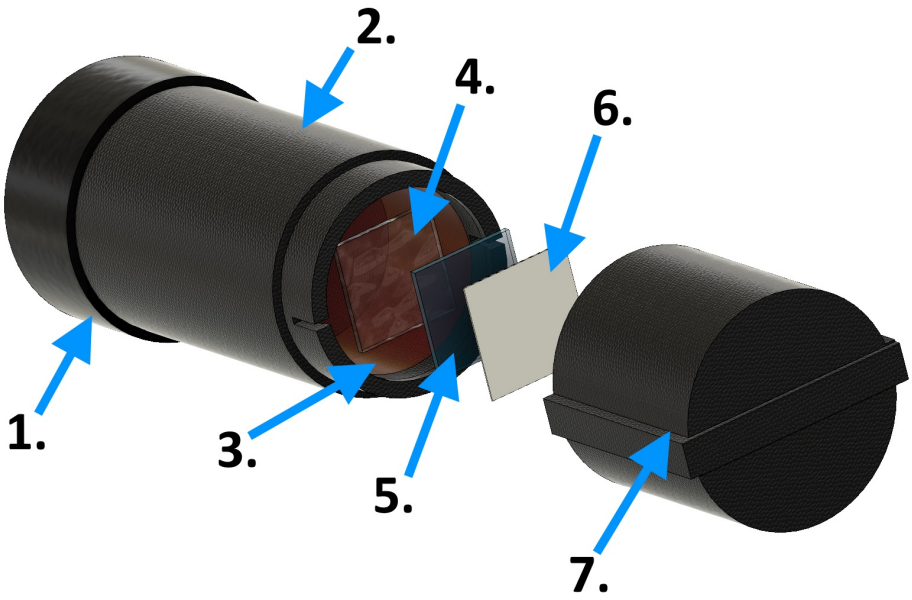

Figure 14. Exploded-view diagram of the scintillator test system (horizontal set-up). 1 - PMT base (Hamamatsu E1198-27), 2 - PMT (Hamamatsu R6231-100) and the custom-built plastic case, 3 - Photocathode, 4 - Optical grade silicon grease, 5 - Eljen EJ 212 PS, 6 - Specular reflector, 7 - Light-tight enclosure.

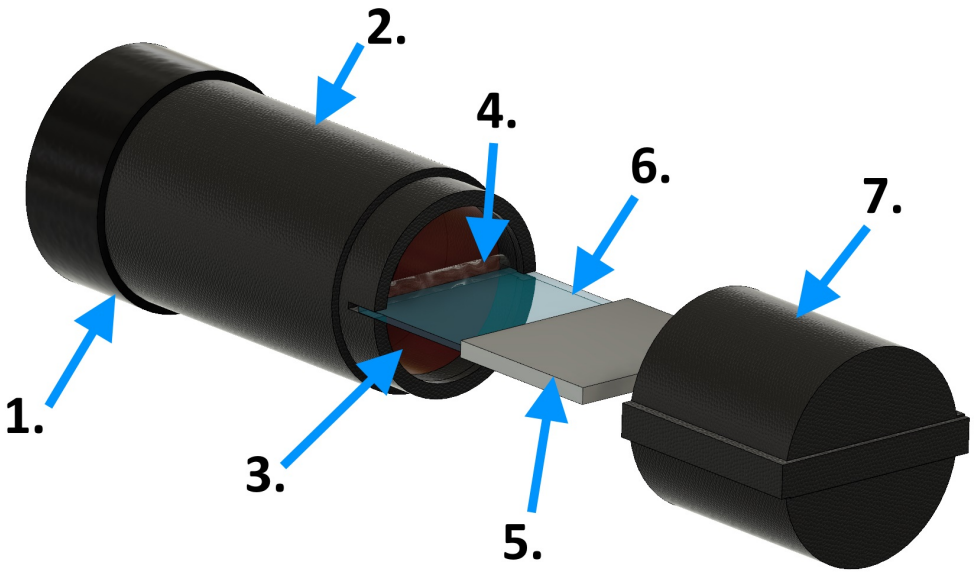

Figure 15. Exploded-view diagram of the scintillator test system (vertical set-up). 1 - PMT base (Hamamatsu E1198-27), 2 - PMT (Hamamatsu R6231-100) and the custom-built plastic case, 3 - Photocathode, 4 - Optical grade silicon grease, 5 - Specular reflector, 6 - Eljen EJ 212 PS, 7 - Light-tight enclosure.

The Eljen EJ-212 PS was received with a sheet sized 1mm x 150 mm x 200 mm. To fit into the plastic case, PS was cut into 1 mm x 40 mm x 60 mm and 1mm x 24 mm x 24 mm pieces using a utility knife. Cutting left the edges of the PS rough, which can be seen with a microscope in Fig. 16. The edges contained a considerable amount of surface roughness that decreases the internal reflection of light in PS, as described in Section 4.4. The rough edges were polished with sandpaper and a Novus plastic polishing kit to facilitate internal reflection. After the polishing procedure, the edges of the PS were considerably smoother, as shown in Fig. 16. As for the front and back surfaces of PS, no polishing was required since they were pre-polished in the factory.

After polishing, a specular reflector was applied to all surfaces except the surface coupling to the PMT window. Lastly, the optical coupling of PS and PMT window was done using Saint-Gobain BC-631 optical grade silicone grease with an index of refraction of 1.465, which is very close to the index of refraction of the PS (1.58) and PMT window (1.5).

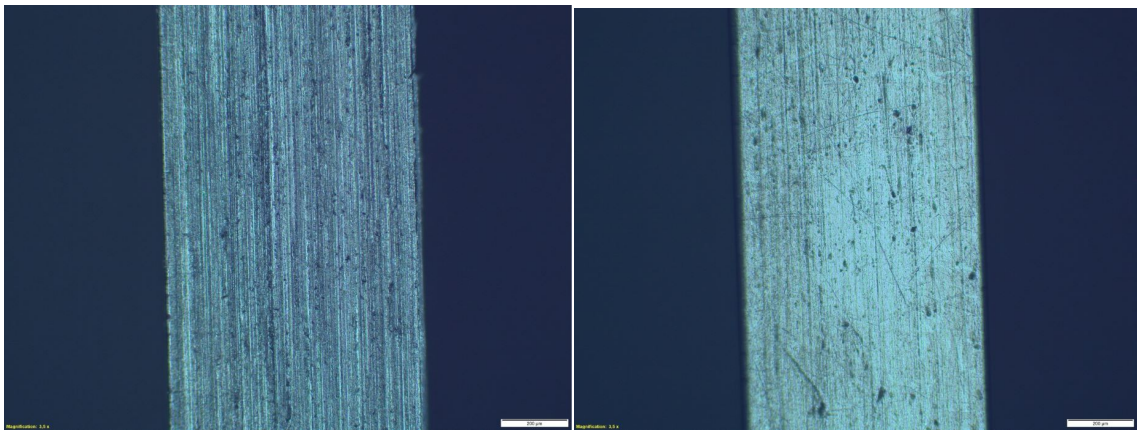

(a) **(b)**

Figure 16. (a): Surface roughness visible in the edge of PS. (b): Reduced surface roughness in the edge of PS after polishing.

6.3 Triple-Layer Phoswich Design

The triple-layer phoswich design presented here is a more sophisticated version of the simple scintillator system (horizontal set-up) described earlier. The system features a phoswich scintillation package together with PS and is closer to actual DEFACTO detector design. The triple-layer phoswich design is depicted in Fig. 17. The system is composed of the same piece of PS used in the scintillator test system (horizontal set-up) discussed previously. The system also includes NaI(Tl) and CsI(Na) scintillators.

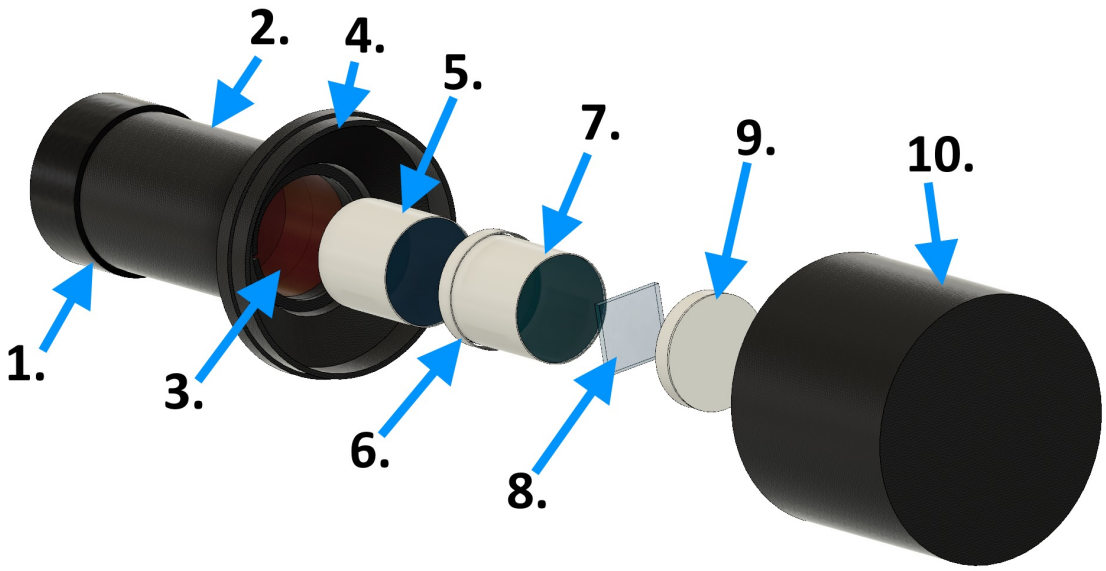

Figure 17. Exploded-view diagram of the triple-layer phoswich design. 1 - PMT base (Hamamatsu E1198-27), 2 - PMT (Hamamatsu R6231-100) and the custom-built plastic case, 3 - Photocathode, 4 - Plastic collar, 5 - CsI(Na) scintillator, 6 - Diffuse reflector, 7 - NaI(Tl) scintillator, 8 - Eljen EJ 212 PS, 9 - Specular reflector, 10 - Light-tight enclosure.

A bigger plastic case was needed to protect the PMT and scintillators from ambient light. The lower part of the case was taken from the simple scintillator system, but a substantially larger-cap was made to fit a 5 cm long scintillator package inside. The new cap and a collar was 3D modeled using Autodesk Fusion 360 CAD design software and were subsequently 3D printed with an Ultimaker 3 printing device using black PLA (polylactic acid) thermoplastic polymer. Black wrapping tape was used to cover the seam between case and cap to ensure maximum light-tightness.

The triple-layer phoswich design was assembled on top of the PMT. First, CsI(Na) scintillator was placed in the center of the PMT window with Saint-Gobain BC-631 optical grade silicone grease used in the coupling of scintillator and PMT windows. Secondly, NaI(Tl) scintillator was placed on top of the CsI(Na) scintillator, and silicone grease was placed between their optical windows. Next, the PS was placed on top of the NaI(Tl) optical window, and silicone grease was again placed in between to facilitate the transmission of light from the PS to the phoswich package. Lastly, a specular reflector of thin aluminized Mylar was wrapped on top of the PS, and a diffuse reflector of PFTE Teflon tape was wrapped to cover the seam between the CsI(Na) and NaI(Tl) scintillators.

6.4 Cylindrical Phoswich Design

As an alternative to the triple-layer phoswich design presented earlier, a cylindrical phoswich design was built to demonstrate contamination monitoring from the sides of the detector. The cylindrical phoswich design is depicted in Fig. 18. The system is composed of Eljen EJ-212 PS, which is bent into a hollow cylindrical shape. Otherwise, the same inorganic crystals and electronics are used in this design as in the previous designs.

The same plastic case from triple-layer phoswich design was used to seal the system from ambient light. To reshape the sheet of PS into a hollow cylinder shape, PS was first to cut into a 1 mm x 100 mm x 150 mm piece using a utility knife. The aim was first to heat the PS to its softening point and then to bent the PS around a support matrix. Before the heating process, an aluminum tube with an diameter of 46 mm was made to serve as a support matrix for PS. The diameter of 46 mm was chosen because the cylindrical PS needed to be smaller than the PMT window (51 mm diameter) but wider than the 38 mm CsI(Na) and NaI(Tl) scintillators. One layer of Teflon (PFTE) tape was applied to support the matrix to prevent the PS from sticking to the support matrix during the heating process. Heating was performed using an environmental chamber.

The chamber was first heated close to the softening point of the PS (75 °C, according to manufacturer). Reshaping was first tried at this temperature, but the PS was still too stiff to be bent around the support matrix. The temperature was then increased in steps, and bending was attempted between every step. Reshaping finally succeeded at a temperature above 90 °C. After reshaping, the PS was left

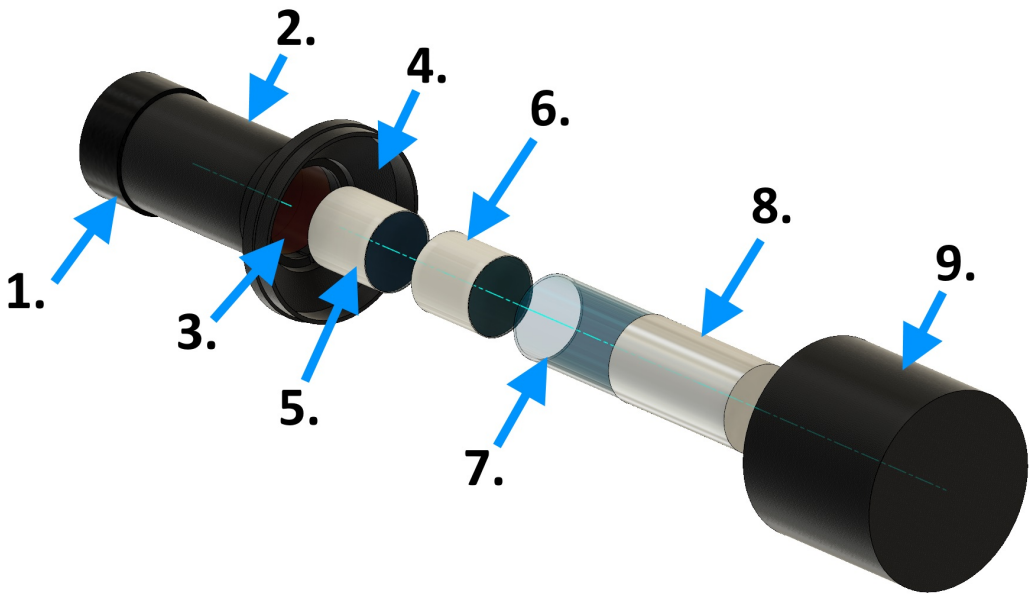

Figure 18. Exploded-view of the cylinder-shaped phoswich design. 1 - PMT base (Hamamatsu E1198-27), 2 - PMT (Hamamatsu R6231-100) and the custom-built plastic case, 3 - Photocathode, 4 - Plastic collar, 5 - CsI(Na) scintillator, 6 - NaI(Tl) scintillator, 7 - Cylinder-shaped Eljen EJ 212 PS, 8 - Specular reflector, 9 - Light-tight enclosure.

to cool to room temperature. Afterward, the edges of the PS were polished with sandpaper and a Novus plastic polishing kit to facilitate internal reflection.

After polishing, the specular reflector was applied to all surfaces except the surface coupling to the PMT window. In contrast to previous designs, standard household aluminum foil was used as the specular reflector, as it was easier to wrap onto the hollow cylindrical PS. Thin aluminized Mylar was too stiff to be wrapped into such a shape.

When the cylindrical PS was finished, assembly of the cylindrical phoswich design could begin. First, CsI(Na) scintillator was connected to the center of the PMT window using Saint-Gobain BC-631 optical grade silicone grease. Secondly, the NaI(Tl) scintillator was connected on top of the CsI(Na) scintillator, and optical grade silicone grease was again used in the coupling. Then, diffuse reflector (PFTE Teflon tape) was used to cover the coupling point of scintillators, and the optical window of NaI(Tl) scintillator. Lastly, cylindrical PS was placed around the CsI(Na), and NaI(Tl) phoswich scintillator and optical coupling of the PS and PMT window were done using optical grade silicone grease.

6.5 Pulse Shape Discrimination

Pulse Shape Discrimination (PSD) is a commonly used technique for separating scintillation signals, which is essential when trying to identify the nature of interacting particles, e.g., neutrons in a flux of gamma rays. PSD is typically used for neutron-gamma signal discrimination, where radiation type can be separated by identifying signal responses in the single scintillating material. PSD can also be used for the separation of alpha-gamma, beta-gamma, or alpha-beta signals, which often involves using two different scintillation materials. A common practice is to combine slow scintillator with a fast scintillator, e.g., inorganic and plastic.

PSD is based on the scintillation signal shape, which is unique for different scintillation materials. The intensity of the scintillation light pulse at a time t has an exponential form that can be described with the following equation [11]

$$I = I_0(e^{-t/\tau_2} - e^{-t/\tau_1}) \tag{7}$$

where I_0 the intensity of light at time $t = 0$ and τ_1 and τ_2 are time constants of scintillator signal rise and decay times. By measuring the shape of each signal pulse, signals can be separated and analyzed independently.

There are various means to carry out PSD. Commonly implemented methods are rise-time discrimination and charge integration [11]. Rise-time discrimination or zero-crossing is a technique where the time difference between the beginning of a pulse (pulse amplitude above zero at some threshold) and zero crossover point, i.e., the point where the pulse amplitude returns to the same level prior the pulse, is integrated using an analog integrator circuit. The resulting time difference is then transformed into a pulse amplitude, which can be used to discriminate the nature of the interacting particle.

In charge integration, the signal pulse is integrated over two different time regions: short and long. Signal pulses are then categorized by their response to integrations. In essence, signals fitting within the short time region are classified as fast signals, and likewise, signals matching a long time region are categorized as slow signals. Charge integration can be done with an analog integrator circuit or with digital signal processing (DSP). The latter method is preferred nowadays because digital discriminators can be integrated into digitizers, which eliminates the need for extra electronic modules and therefore simplifies measurement setups.

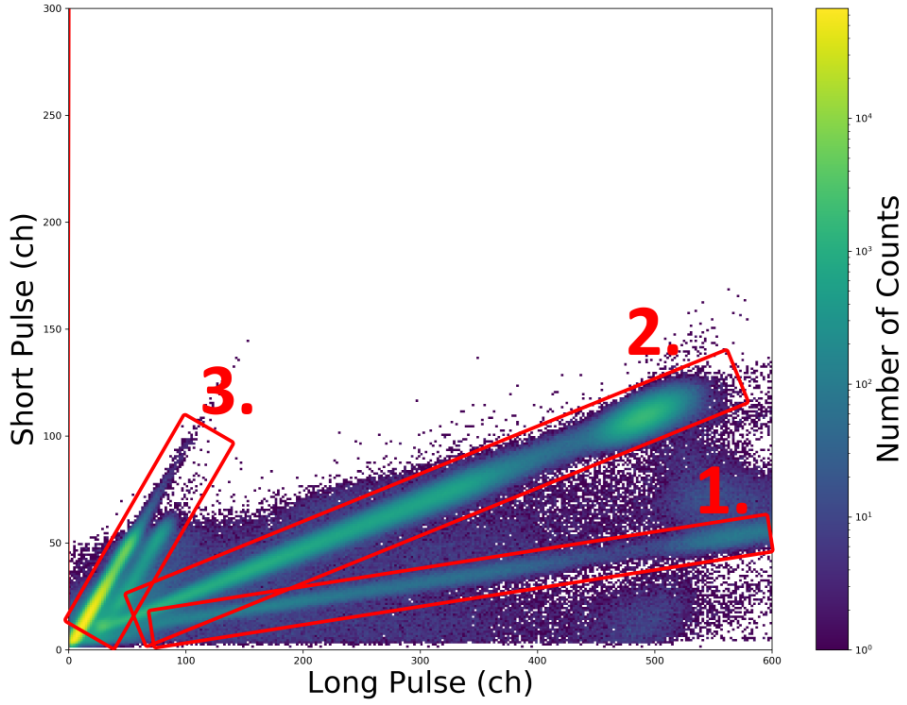

Figure 19. PSD plot showing the separated scintillation signals: 1 - CsI(Na), 2 - NaI(Tl), 3 - PS.

In this thesis, PSD analysis is done by using the charge integration method, which is implemented with a built-in discriminator in the CAEN DT5730 digitizer. In the CAEN DT5730, charge integration is realized with DSP, which is controlled by defining short and long integration regions, i.e., short gate and (long) gate. When the signal is recorded, each pulse is integrated over the defined short and long time regions. The digitizer outputs the integrated values of both time regions for each event and the data can be read from list-mode data file recorded by the digitizer.

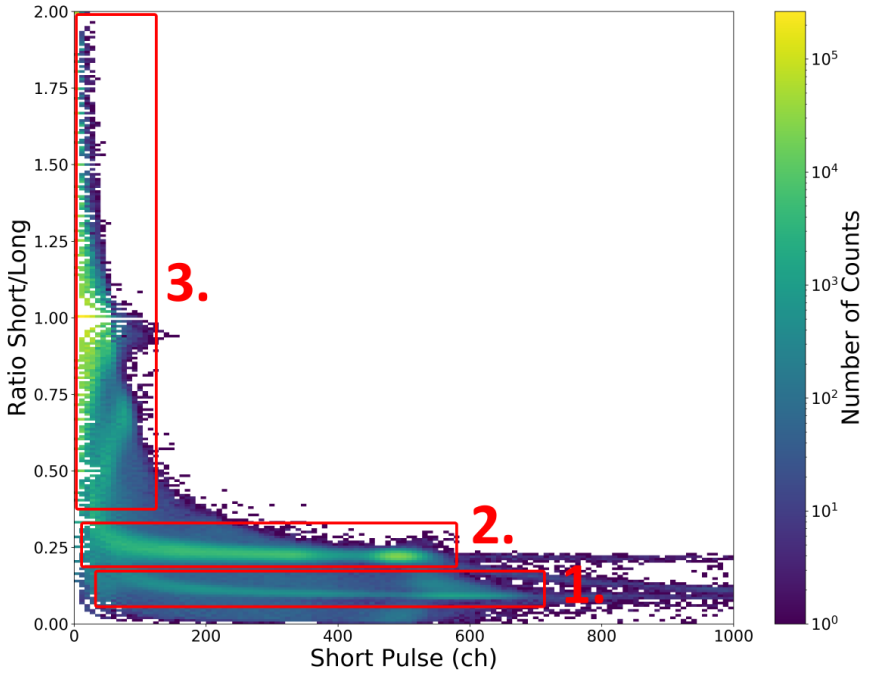

Figure 20. PSD ratio plot depicting the separated scintillation signals: 1 - CsI(Na), 2 - NaI(Tl), 3 - PS.

After recording, a Python script was used to plot the distribution of the values integrated over the short and long time region. Fig. 19 shows an example plot of PSD analysis depicting the response of the triple-layer phoswich (see Section 6.3) to ^{137}Cs source. As the figure shows, there are three distinctive lines, each representing a different scintillating material. The two lower lines are slow inorganic scintillator signals, and the upper line is a fast PS signal.

Now, by plotting the ratio of short and long integration ranges as a function of the long pulse, we can specify the PSD cut parameter to enable discrimination of scintillator signals. Fig. 20 shows an example plot of the ratio of short and long integration ranges recorded with the triple-layer phoswich. From the figure, we can

see three different scintillation signals: lower lines representing CsI(Na) and NaI(Tl) scintillators and everything above is PS signal. By specifying the PSD cut parameter to around 0.45, the fast PS signal could be separated from the slow inorganic signals. Likewise, inorganic signals could be further separated with a PSD cut parameter of around 0.17.

7 Measurement Results

This section is divided into three subsections. The preliminary studies section covers the measurements done with the scintillator test system. Studies with the top monitoring configuration section present the measurements done with the triple-layer phoswich design. Similarly, studies with the side monitoring configuration section show the results done with the cylindrical phoswich design.

7.1 Preliminary Studies

7.1.1 Time Coincidence Analysis

The objective of this test was to verify the location of the full energy conversion electron peak in the measured energy spectrum of the ^{137}Cs source. To find the location of the full energy peak of ^{137}Cs 624 to 661 keV conversion electrons, time coincidence analysis was used to filter out non-relevant events (betas and photons) and only to observe conversion electrons that are coincident with x-rays.

Table 8. Parameters for x-ray/conversion electron coincidence measurement. See CAEN DT5730 manual for description of the following parameters [22].

Parameters	Scintillator Test System	NaI(Tl) scintillator
Measurement Time, s	300	300
Voltage, V	750	900
Discriminator Mode	Leading Edge	Leading Edge
Threshold, lsb	15	70
Trigger Holdoff, ns	200	2000
Input Smoothing, samples	16	16
Energy Coarse Gain, fC/lsb	2.5	2.5
Gate, ns	80	800
Short Gate, ns	30	200
Pre-Gate, ns	30	100

The coincidence measurement was done using the vertical set-up of the scintillator test system depicted in Section 6.2. The detailed measurement set-up and parameters used in the coincidence test are described in Fig. 21 and Table 8. The scintillator

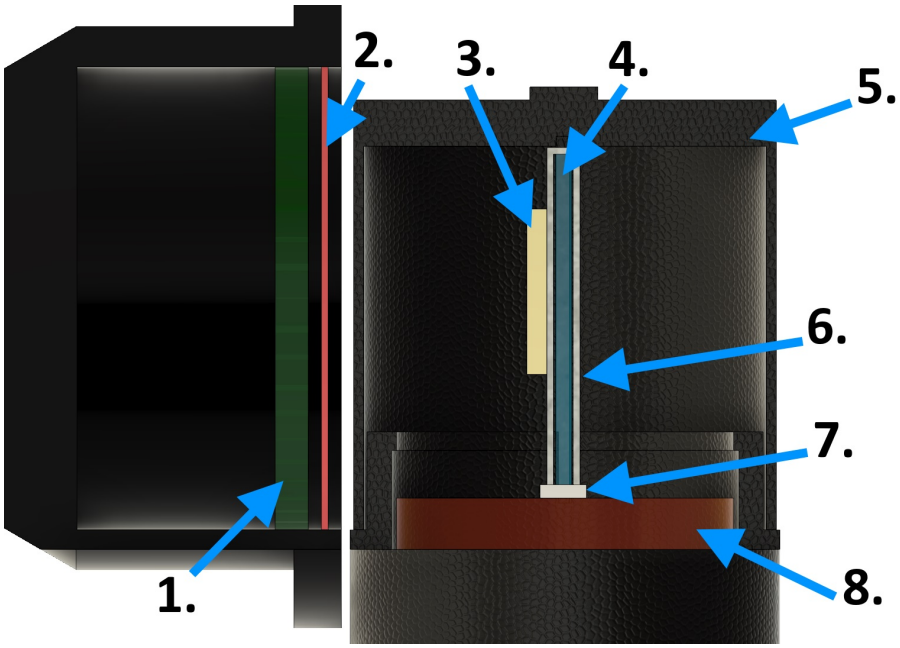

Figure 21. Time coincidence measurement set-up. 1 - Scionix 102BD4/33-X NaI(Tl) scintillator, 2 - Beryllium window, 3 - Calibration source, 4 - Eljen EJ 212 plastic scintillator, 5 - Light-tight enclosure, 6 - Specular reflector, 7 - Optical grade silicone grease, 8 - PMT window.

test system was used to measure conversion electrons from the ^{137}Cs source, which was attached directly to the PS. X-rays were measured using a Scionix 102 BD4/33-X scintillator, which features a 4 mm thin NaI(Tl) crystal with a beryllium entrance window. The window of the NaI(Tl) scintillator was placed directly outside the light-tight enclosure of the scintillator test system. High voltage for photomultipliers was supplied with a CAEN model DT5533E high voltage power supply, and data acquisition was performed using the CAEN model DT5730 Digitizer.

Coincidence analysis was done using a Python script. The script takes the list-mode data file recorded by the CAEN Digitizer as input and finds the coincidence time-difference of the signals recorded in both detectors. First, the script is run without specifying a time coincidence cut to plot the time difference between all events that both detectors register. Using this plot (Fig. 22), we can determine the timecut-parameter, which defines the coincidence time window that we are interested in. From the plot, we can see the peak of events falls between a time difference of -250 to 0 ns, which is used as a parameter to select the coincident events.

The result of the time coincidence analysis is shown in Fig. 23. As the figure shows, in both plots, there are two visible peaks: a larger peak at a channel number

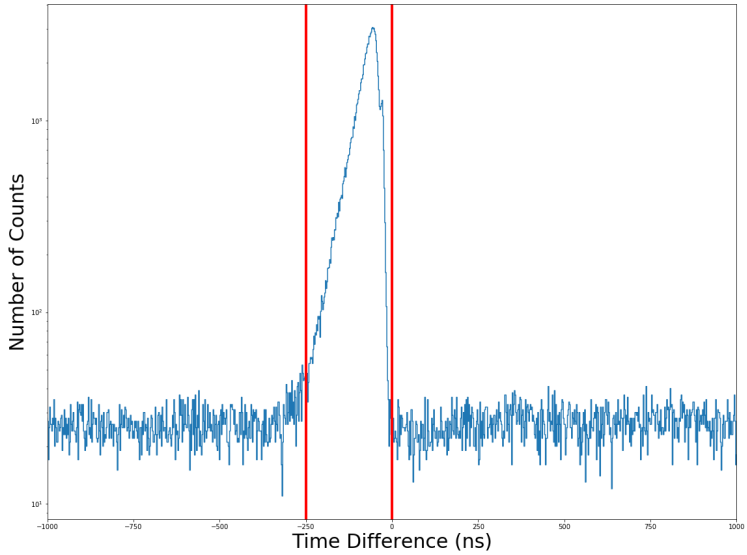

Figure 22. Time coincidence analysis plot used to determine width of the selection window.

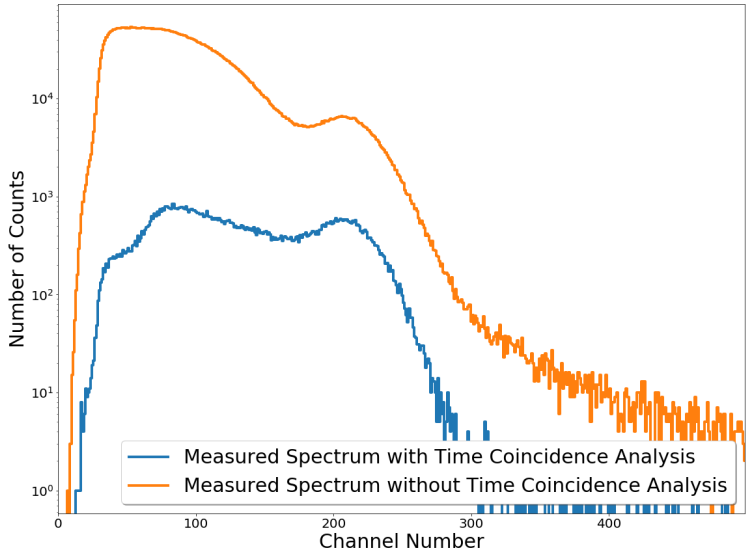

Figure 23. The result of time coincidence analysis for ^{137}Cs source.

of around 100 and a smaller peak at a channel number of about 200. The peak on the lower energy can be identified as the punch-through peak representing both beta particles and conversion electrons because its height is significantly reduced by the coincidence analysis, i.e., most of the filtered events are in the lower energy peak. The peak on the higher energy is the full energy peak representing only 624 keV to 661 keV conversion electrons that were stopped entirely in the plastic scintillator.

In conclusion, the location of the full energy conversion electron peak can be identified from the ^{137}Cs spectrum even without time coincidence analysis. Presumably, full energy conversion electron peaks can be distinguished from other sources, such as ^{133}Ba and ^{207}Bi, as well. Thus, these conversion electron sources can be used for energy calibration of the thin plastic scintillator setups. However, determination of the location of the punch through peak is difficult without a coincidence measurement.

7.1.2 Impact of Reflector Material

The impact of specular reflector material on the beta detection efficiency and light collection capability of the system was tested using the vertical set-up of the scintillator test system that was introduced in Section 5.2. Two specular reflector materials were tested: Aluminized Mylar film with a thickness of 12 µm and standard household aluminum foil with a thickness of 16 µm.

The following tests were performed with the measurement set-up depicted in Fig. 24 and using the measurement parameters given in Table 9. The impact of reflector material was tested using the ^{90}Sr source, for which calibration data is given in Table 7. Measurement data for both specular reflector materials is shown in Fig. 25. As the figure shows, with Mylar film, slightly more recorded counts in the region between channel numbers 100 to 400 than with aluminum foil can be observed.

To calculate the beta detection efficiency or the intrinsic efficiency, we must first determine the absolute and geometric efficiency of the system. Absolute efficiency is defined as follows

$$\epsilon_{\text{abs}} = \frac{\text{number of recorded counts}}{\text{number of radiation quanta emitted by source}} = \frac{C}{A \cdot t}, \tag{8}$$

where the C is the number of counts recorded in the spectrum, A is the activity of source, and t is live time of the measurement (that is real time - dead time). Now,

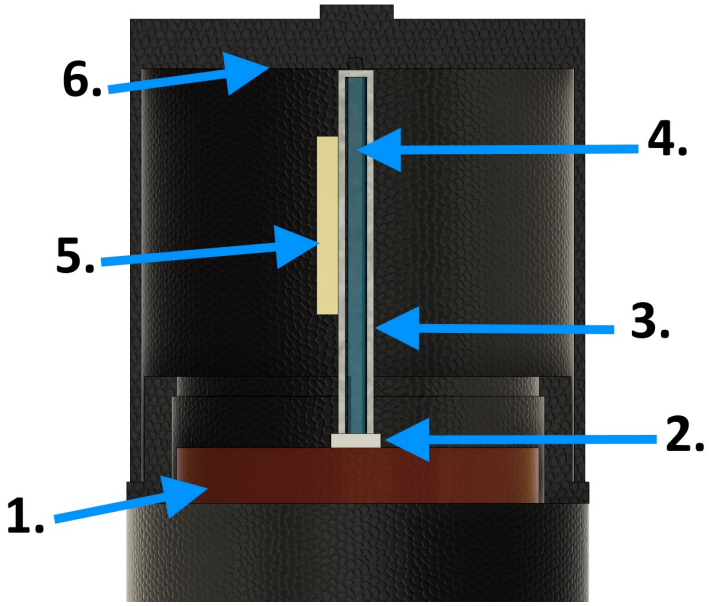

Figure 24. Cross-sectional view of the measurement set-up. 1 - Photocathode, 2 - Optical grade silicon grease, 3 - Specular reflector, 4 - Eljen EJ 212 plastic scintillator, 5 - Radioactive calibration source, 6 - Light-tight enclosure.

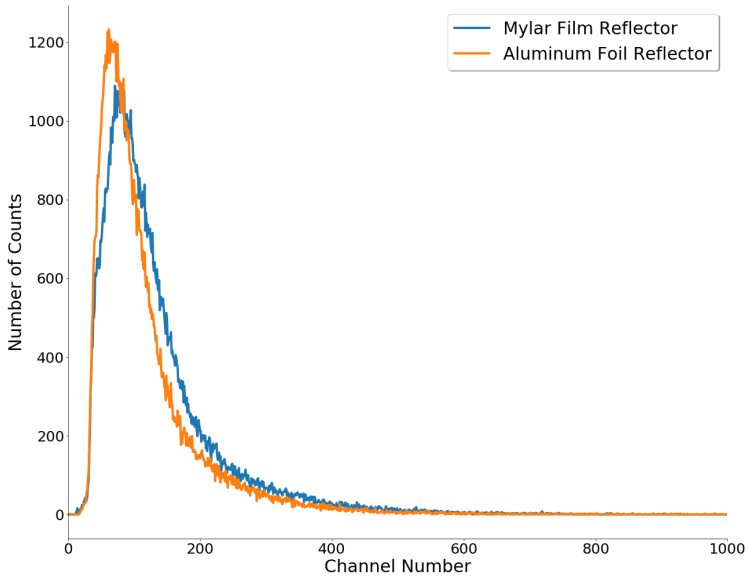

Figure 25. The measured spectrum of ^{90}sr. Total recorded counts for Mylar reflector: 127680, for aluminum foil reflector: 116862. The measurement time was set to 300 s in both measurements.

Table 9. Parameters for the measurement. See CAEN DT5730 manual for description of the following parameters [22].

Parameter	
Measurement Time, s	300
Voltage, V	750
Discriminator Mode	Leading Edge
Threshold, lsb	15
Trigger Holdoff, ns	200
Input Smoothing, samples	16
Energy Coarse Gain, fC/lsb	2.5
Gate, ns	80
Short Gate, ns	30
Pre-Gate, ns	30

for absolute efficiency, the following definition applies

$$\epsilon_{\text{abs}} = \epsilon_{\text{int}} \cdot \epsilon_{\text{geom}}. \tag{9}$$

The geometrical efficiency ϵ_{geom} can be defined as:

$$\epsilon_{\text{geom}} = \frac{\Omega}{4\pi}, \tag{10}$$

where Ω is solid angle facing detector and the radioactive source. However, as we are using a measurement set-up where the source is placed in contact with a plastic scintillator, we can estimate that geometrical efficiency is close to 50 % (2π efficiency). In this thesis, we are using two different kinds of sources: ones that are sealed between Mylar films and ones that are sealed in an aluminum plate. The Mylar covered sources (^{137}Cs and ^{133}Ba) have a thicker outer ring, which slightly reduces geometric efficiency. Also, the reflector material that is placed between source and detector will further reduce geometrical efficiency. Therefore, geometrical efficiency for ^{137}Cs and ^{133}Ba sources can be estimated to be (40 ± 5) %. For the ^{207}Bi and ^{90}sr sources, the geometrical efficiency is closer to 50 %. However, the aluminum backface will cause electron backscattering, which increases the probability of electrons to hit the detector and thus increase the geometrical efficiency of set-up. Electron backscattering can be estimated using Muller formula [23, p. 118]

$$R = aZ + b, \tag{11}$$

where a and b are constants that depend on the element of absorber material, and Z is the atomic number of absorber material. The Muller formula does not account for the electron energy or incident angle and therefore serves as a crude estimate of the fraction of backscattering. For aluminum, a and b are 0.96731 and 0.476 [23, p. 118]. Using the equation, we can estimate the backscattering of electrons and betas to be 13 % for the ^{207}Bi and ^{90}Sr sources. Therefore, geometrical efficiency for ^{207}Bi and ^{90}Sr source (63 ± 10) %.

The beta detection efficiency of the detector can be estimated by calculating the intrinsic efficiency using equations of geometrical efficiency (10) and absolute efficiency (8) as

$$\epsilon_{\text{int}} = \frac{C}{2At \cdot \epsilon_{\text{geom}}}. \tag{12}$$

The multiplier of 2 in the above equation results from ^{90}Y, which is daughter nuclide of ^{90}Sr and is in equilibrium with parent nuclide. Measurement with the ^{90}Sr source was done on November 11th, 2019, and the activity of the source then was calculated to be 573.7 Bq. The measurement time was 300 s. The total counting efficiency with the Mylar reflector was

$$\epsilon_{\text{int}} = \frac{127680 \text{ counts}}{2 \cdot 575.9\,\text{Bq} \cdot 300.152\,\text{s} \cdot 0.63} = 0.5862245593.$$

The uncertainty on the beta detection efficiency can be estimated using the propagation of uncertainty where the partial derivative of the equation is taken with respect to error causing variables. For equation (12), the uncertainty is produced from geometrical efficiency, activity, live time estimate and the number of recorded counts estimate. Now, taking the partial derivative of equation of beta detection efficiency with respect to number of counts, geometrical efficiency, activity and measurement time results in

$$\frac{\partial \epsilon_{\text{int}}}{\partial C} = \frac{1}{2At \cdot \epsilon_{\text{geom}}} = \frac{1}{2 \cdot 575.9\,\text{Bq} \cdot 300.152\,\text{s} \cdot 0.63} = 4.591\,357\,763\,989\,576 \times 10^{-6}.$$

$$\frac{\partial \epsilon_{\text{int}}}{\partial \epsilon_{\text{geom}}} = -\frac{C}{2At \cdot \epsilon_{\text{geom}}^2} = -\frac{127680 \text{ counts}}{2 \cdot 575.9\,\text{Bq} \cdot 300.152\,\text{s} \cdot 0.63^2} = -0.9305151735018872.$$

$$\frac{\partial \epsilon_{\text{int}}}{\partial A} = -\frac{C}{2At \cdot A^2} = -\frac{127680 \text{ counts}}{2 \cdot (575.9\,\text{Bq})^2 \cdot 300.152\,\text{s} \cdot 0.63} = -1.017\,927\,694\,575\,775\,2 \times 10^{-3}.$$

$$\frac{\partial \epsilon_{\text{int}}}{\partial t} = -\frac{C}{2At \cdot t^2} = -\frac{127680 \text{ counts}}{2 \cdot 575.9\,\text{Bq} \cdot (300.152\,\text{s})^2 \cdot 0.63} = -1.953\,092\,297\,589\,851 \times 10^{-3}.$$

As the ^{90}Sr source was made in STUK and no estimation of the uncertainty of the activity was given with the source. Therefore, I estimate the uncertainty of the source activity to be 5 percent. As for measurement time, the uncertainty comes from the quartz oscillator, which typical frequency uncertainty is 1×10^{-9} Hz [24, p. 18-4] and for number of counts, I estimate one percent error in the results. The uncertainty of beta counting efficiency can be calculated using the variance formula

$$\begin{aligned}
\delta\epsilon_{\text{int}} &= \left(\left(\frac{\partial \epsilon_{int}}{\partial C} \cdot \delta C \right)^2 + \left(\frac{\partial \epsilon_{int}}{\partial \epsilon_{\text{geom}}} \cdot \delta \epsilon_{\text{geom}} \right)^2 + \left(\frac{\partial \epsilon_{int}}{\partial A} \cdot \delta A \right)^2 + \left(\frac{\partial \epsilon_{int}}{\partial t} \cdot \delta t \right)^2 \right)^{\frac{1}{2}} \\
&= \left(\left(4.591\,357\,763\,989\,576 \times 10^{-6} \cdot 0.01 \right)^2 + \left(-0.9305151735018872 \cdot 0.10 \right)^2 \right. \\
&+ \left(-1.017\,927\,694\,575\,775\,2 \times 10^{-3} \cdot 0.05 \right)^2 \\
&+ \left. \left(-1.953\,092\,297\,589\,851 \times 10^{-3} \cdot 1 \times 10^{-9} \right)^2 \right)^{\frac{1}{2}} \\
&= 0.09305153126959578.
\end{aligned}$$

As a result, beta detection efficiency for Mylar reflector is (0.6 ± 0.1). Next, beta detection efficiency for aluminum foil reflector can be calculated in a similar manner and results in (0.54 ± 0.09).

Finally, the light collection capability of the system was examined for both reflectors. The light collection capability can be estimated from the gradient or slope of the energy calibration curve, i.e., less gradient, better light collection capability. Since the energy calibration was not done for the given systems in this measurement, the alternative solution for examining the light collection capability is to investigate how quickly the intrinsic efficiency curve decays as a function of minimum pulse

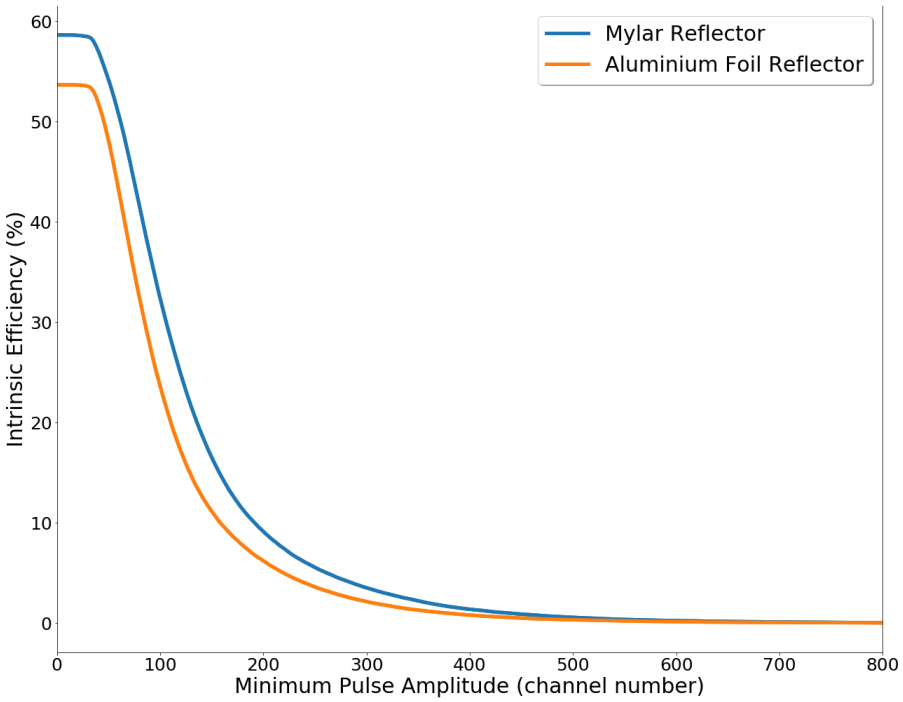

Figure 26. Intrinsic efficiency plotted against the minimum pulse amplitude for different specular reflector materials.

amplitude in channels and is depicted in Fig. 26. The following curves were made by summing up the intrinsic efficiency,i.e., recorded counts in the spectrum divided by the calculated incident quanta over an interval of channels while gradually decreasing the summation interval. The system with the lower light collection capability shows a more rapidly decaying intrinsic efficiency curve. The summation was made with the Python script that is shown in Appendix A.

As was calculated earlier, Mylar reflector provides marginally better beta detection efficiency. Improved beta detection efficiency is likely due to Mylar being thinner and less dense, which therefore induce less backscattering and electron attenuation. Also, as we can see from Fig. 26, the intrinsic efficiency curve of the Mylar reflector decays slightly slower, which indicates that the Mylar reflector provides slightly better light collection. In conclusion, Mylar is a marginally better reflector material than aluminum foil because it offers better beta detection efficiency and improved light collection capability.

7.1.3 Impact of Scintillator Polishing

In this measurement, the objective was to test the impact of plastic scintillator polishing on the beta detection efficiency and light collection capability of the system. The edges of the PS contained a significant amount of surface roughness, which presumably reduces the internal reflection of light inside the PS and, therefore, should negatively impact beta detection efficiency and light collection capability.

The measurement are performed with the same measurement set-up and parameters that were described in Fig. 24 and Table 9. The ^{90}Sr source, the calibration data of which is given in Table 7, was used as a source of beta particles. Measurement data for both unpolished and polished scintillator is shown in Fig. 27. As the figure presents, there is little difference between the spectra, even though there are slightly more recorded counts with the polished scintillator.

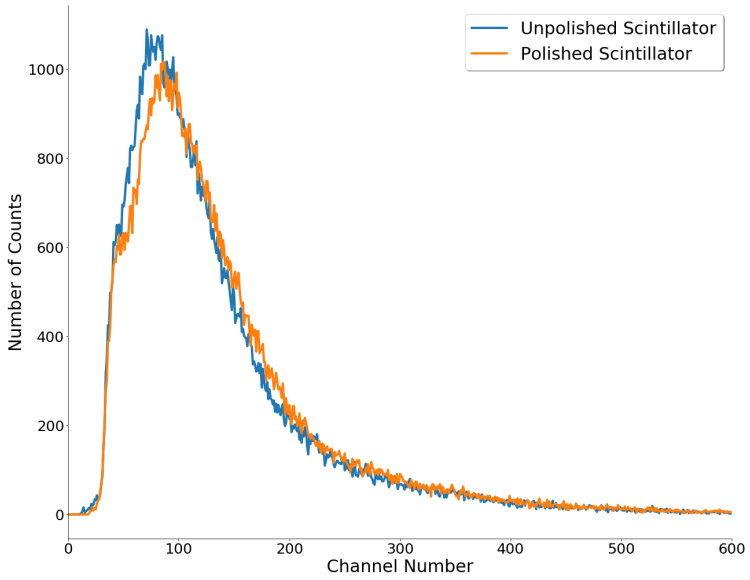

Figure 27. The measured spectrum of ^{90}Sr. Total recorded counts for unpolished scintillator: 127680, for polished scintillator: 128386.

The beta detection efficiency can be calculated using equation 12 that was derived in Section 7.1.2. For the polished scintillator, beta detection efficiency is

$$\epsilon_{\text{int}} = \frac{128386 \text{ counts}}{2 \cdot 575.6\,\text{Bq} \cdot 300.212\,\text{s} \cdot 0.63} = 0.5896554135.$$

As in the previous Section, the uncertainty of beta detection efficiency can be estimated by using propagation of uncertainty where equation (12) is partially

differentiated with respect to error causing variables which results in

$$\frac{\partial \epsilon_{\text{int}}}{\partial C} = \frac{1}{2At \cdot \epsilon_{\text{geom}}} = \frac{1}{2 \cdot 573.7\,\text{Bq} \cdot 300.152\,\text{s} \cdot 0.63} = 4.592\,832\,656\,599\,723 \times 10^{-6}.$$

$$\frac{\partial \epsilon_{\text{int}}}{\partial \epsilon_{\text{geom}}} = -\frac{C}{2At \cdot \epsilon_{\text{geom}}^2} = -\frac{127680\ \text{counts}}{2 \cdot 573.7\,\text{Bq} \cdot 300.152\,\text{s} \cdot 0.63^2} = -0.9359609737304952.$$

$$\frac{\partial \epsilon_{\text{int}}}{\partial A} = -\frac{C}{2At \cdot A^2} = -\frac{127680\ \text{counts}}{2 \cdot (573.7\,\text{Bq})^2 \cdot 300.152\,\text{s} \cdot 0.63} = -1.024\,418\,716\,904\,468\,3 \times 10^{-3}.$$

$$\frac{\partial \epsilon_{\text{int}}}{\partial t} = -\frac{C}{2At \cdot t^2} = -\frac{127680\ \text{counts}}{2 \cdot 573.7\,\text{Bq} \cdot (300.152\,\text{s})^2 \cdot 0.63} = -1.964\,130\,059\,592\,928\,7 \times 10^{-3}.$$

The uncertainty of beta detection efficiency can now be calculated using the variance formula

$$\begin{aligned}
\delta\epsilon_{\text{int}} &= \left(\left(\frac{\partial \epsilon_{int}}{\partial C} \cdot \delta C \right)^2 + \left(\frac{\partial \epsilon_{int}}{\partial \epsilon_{\text{geom}}} \cdot \delta \epsilon_{\text{geom}} \right)^2 + \left(\frac{\partial \epsilon_{int}}{\partial A} \cdot \delta A \right)^2 + \left(\frac{\partial \epsilon_{int}}{\partial t} \cdot \delta t \right)^2 \right)^{\frac{1}{2}} \\
&= \left(\left(4.592\,832\,656\,599\,723 \times 10^{-6} \cdot 0.01 \right)^2 + \left(-0.9359609737304952 \cdot 0.10 \right)^2 \right. \\
&+ \left(-1.024\,418\,716\,904\,468\,3 \times 10^{-3} \cdot 0.05 \right)^2 \\
&+ \left. \left(-1.964\,130\,059\,592\,928\,7 \times 10^{-3} \cdot 1 \times 10^{-9} \right)^2 \right)^{\frac{1}{2}} \\
&= 0.09359611138851734.
\end{aligned}$$

As a result, beta detection efficiency for polished scintillator is (0.6 ± 0.1). Next, beta detection efficiency for unpolished scintillator can be calculated in a similar manner and results (0.6 ± 0.1).

The light collection capability of the system was examined similarly to in the previous Section by plotting the intrinsic efficiency as a function of the minimum

pulse amplitude for unpolished and polished scintillators, and the results are depicted in Fig. 28. As the figure illustrates, intrinsic efficiency curves decay almost at an equal pace, which indicates that the polishing of the plastic scintillator did not improve the light collection capability of the system. But it is worth noticing that the polishing was done on thin edges of PS and thus represented only a tiny part of the total surface area of the scintillator. Presumably, if major surfaces (front and back) of PS had had substantial surface roughness, scintillator polishing would have a more significant effect on beta detection efficiency and light collection capability of the system.

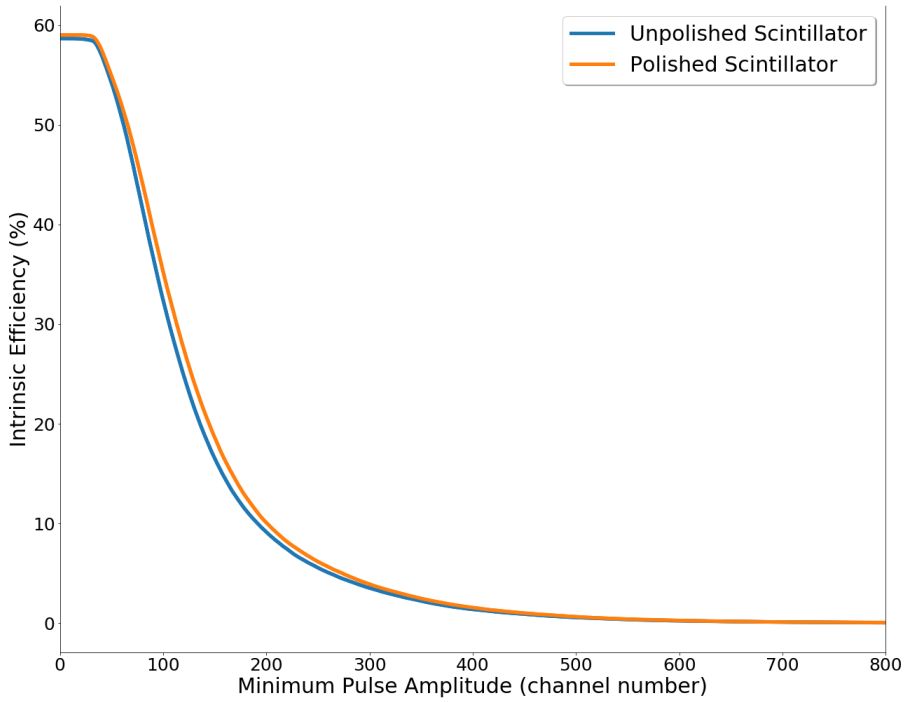

Figure 28. Intrinsic efficiency plotted against the minimum pulse amplitude for the unpolished and polished scintillator.

7.1.4 Impact of Scintillator Orientation

The objective of this measurement was to test the impact of the plastic scintillator orientation on the beta detection efficiency and light collection capability of the system. The orientation in this context means whether the PS is mounted to the PMT window through its thin face (vertical orientation) or front/back face (horizontal orientation). The horizontal and vertical set-ups of the scintillator test system (see Section 6.2) were used in this experiment. Since the setups serve as a simplified version of the top monitoring and side monitoring configurations, this experiment should provide insight into which configuration performs better as the contamination monitoring system. Details of the measurement set-ups and parameters are shown in Fig. 24, Fig. 29 and Table 9. As in previous measurements, ^{90}Sr was used as a source of beta particles.

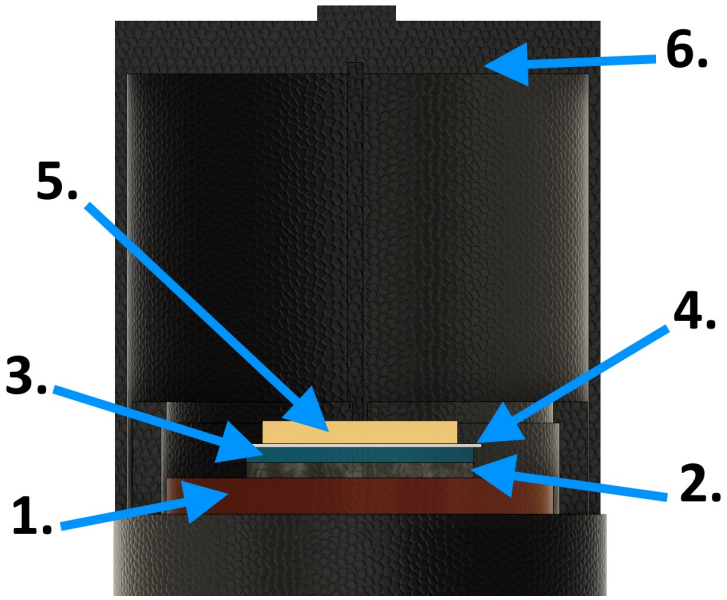

Figure 29. Cross-sectional view of the horizontal measurement set-up. 1 - Photocathode, 2 - Optical grade silicon grease, 3 - Eljen EJ 212 plastic scintillator, 4 - Specular reflector, 5 - Radioactive calibration source, 6 - Light-tight enclosure.

Fig. 30 shows the spectra of the ^{90}Sr source measured with the horizontal and vertical set-ups. A quick examination of the figure shows that with horizontal set-up, the measured spectrum is shifted drastically to the higher energy, indicating better light collection capability. The energy calibration was done for each set-up using conversion electron sources. For the horizontal set-up, following conversion electrons

were used: 320 keV (^{133}Ba), 482 keV (^{207}Bi), 624 keV (^{137}Cs) and 976 keV (^{207}Bi).

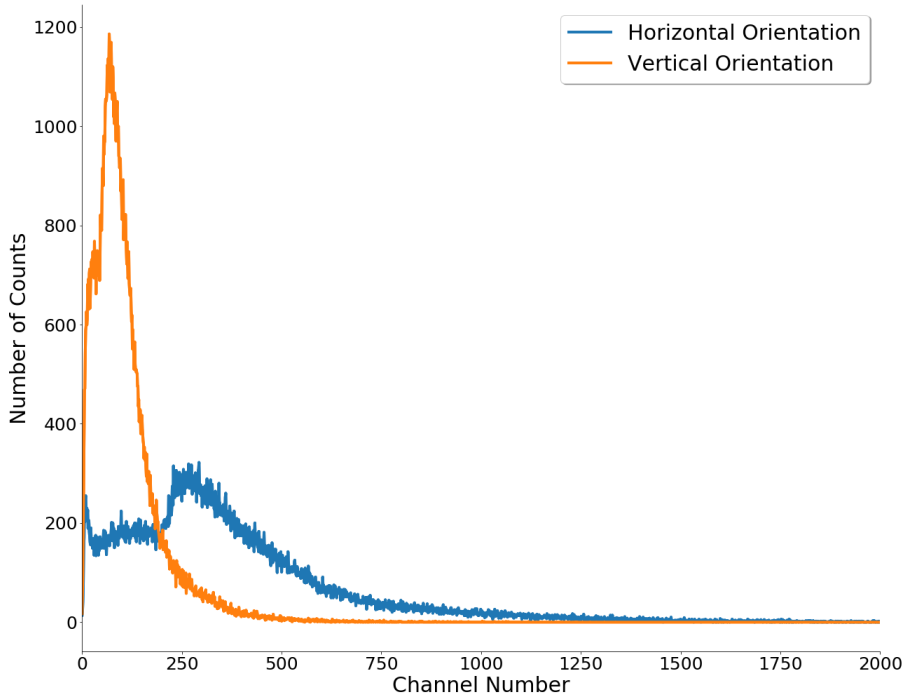

Figure 30. The measured spectrum of ^{90}Sr. Total recorded counts for horizontal orientation: 128503, for vertical orientation: 141338.

Fig. 31 depicts measured spectra of ^{133}Ba, ^{137}Cs, and ^{207}Bi sources measured with the horizontal setup. The asymmetric least squares method, which is introduced in detail in Appendix B, was used to parametrize background from spectra to enable easier Gaussian fitting of conversion electron peaks.

Now, the energy calibration curve can be made by plotting the centroids of Gaussian fitted peaks with matching conversion electron energy values and performing a linear fit to the plot, which is shown in Fig. 32. The uncertainty in the energy calibration curve results from Gaussian peak fitting (x-axis error) and conversion electron energy range (y-axis error). For instance, the ^{137}Cs source emits conversion electrons with a multiple conversion lines from 624 keV to 661 keV with the strongest in relative intensity of 624 keV. Therefore, the y-axis error for ^{137}Cs conversion electron energy is the subtraction of energy range, i.e., 37 keV.

In contrast to horizontal set-up, the energy calibration of the vertical set-up was done using only ^{137}Cs and ^{207}Bi sources. ^{133}Ba was not used because the ^{133}Ba spectrum did not feature any recognizable peaks. The measured spectra are shown in Fig. 33 and an energy calibration curve is shown in Fig. 34.

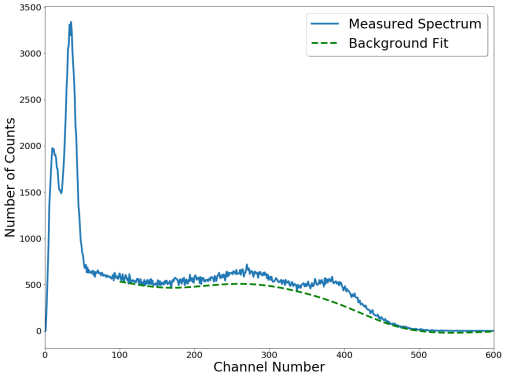

(a) Measured spectrum of ^{133}Ba

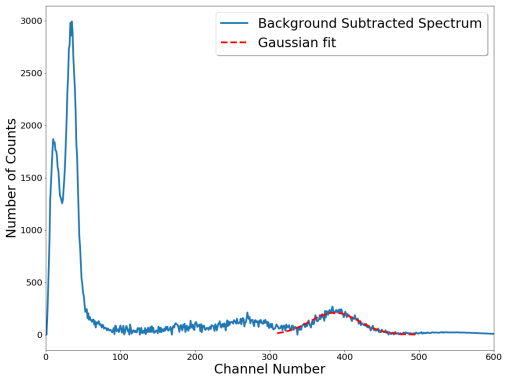

(b) Peak location of ^{133}Ba 320 keV conversion electron lines on 387 channel

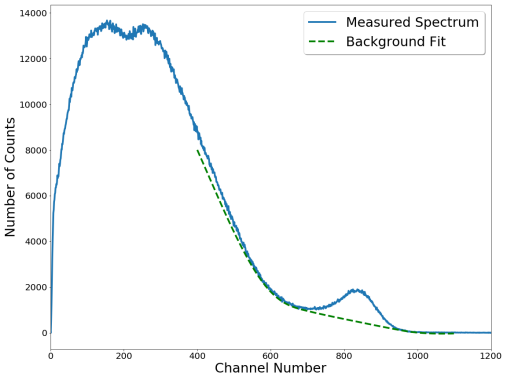

(c) Measured spectrum of ^{137}Cs

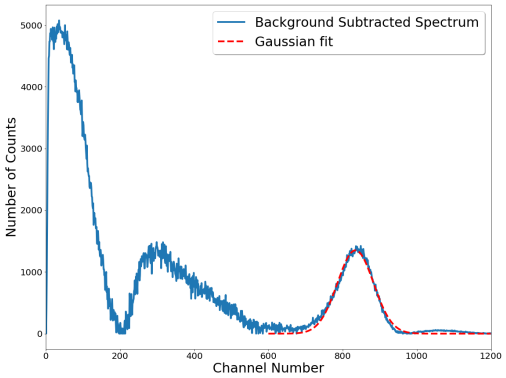

(d) Peak location of ^{137}Cs 624 keV conversion electron lines on 834 channel

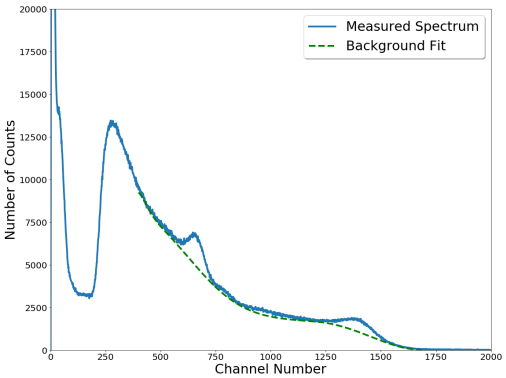

(e) Measured spectrum ^{207}Bi

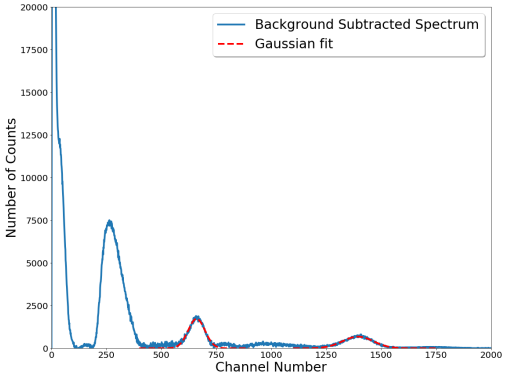

(f) Peak locations of ^{207}Bi 481 keV and 975 keV conversion electron lines on channels 660 and 1394

Figure 31. Measured spectra of ^{133}Ba, ^{137}Cs, and ^{207}Bi sources used for the energy calibration of the horizontal set-up. Figures on left show measured spectra of sources with background fit. Figures on the right depict background subtracted spectra of sources with a Gaussian fitted conversion electrons peaks.

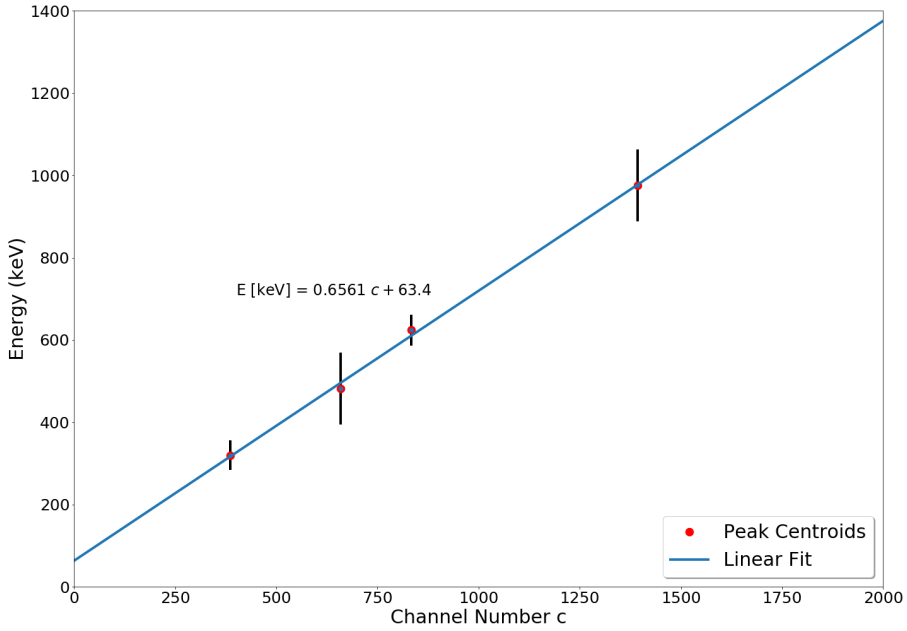

Figure 32. Graph depicting the energy calibration curve of the horizontal set-up. The energy calibration function resulting from the linear fit is E (keV) $= 0.6561c + 63.4$.

The beta detection efficiency can be estimated using equation (12) and for the horizontal set-up results in

$$\epsilon_{\text{int}} = \frac{128503 \text{ counts}}{2 \cdot 572.8\,\text{Bq} \cdot 300.149\,\text{s} \cdot 0.5} = 0.7474348727.$$

In previous sections, the geometrical efficiency of vertical setup was estimated to be (63 $\pm$ 10) percent. However, as for horizontal set-up, geometrical efficiency is estimated to be slightly less, due to the smaller sized PS used in the set-up. In the above equation, the geometrical efficiency of (50 $\pm$ 10) percent was used. Uncertainty of the total beta detection efficiency can be estimated using the propagation of uncertainty which result in

$$\frac{\partial \epsilon_{\text{int}}}{\partial C} = \frac{1}{2At \cdot \epsilon_{\text{geom}}} = \frac{1}{2 \cdot 572.8\,\text{Bq} \cdot 300.149\,\text{s} \cdot 0.5} = 5.807\,353\,319\,903\,871 \times 10^{-6}.$$

$$\frac{\partial \epsilon_{\text{int}}}{\partial \epsilon_{\text{geom}}} = -\frac{C}{2At \cdot \epsilon_{\text{geom}}^2} = -\frac{128503 \text{ counts}}{2 \cdot 572.8\,\text{Bq} \cdot 300.149\,\text{s} \cdot 0.5^2} = -1.4925246473352143.$$

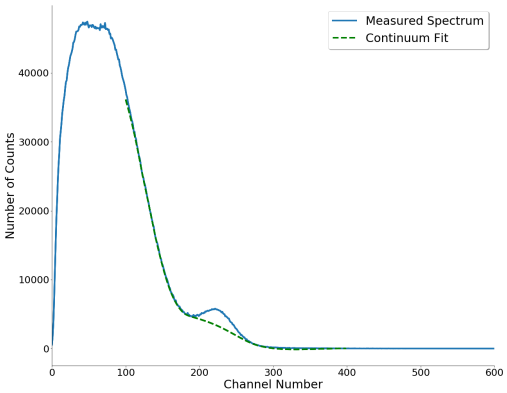

(a) Measured spectrum of ^{137}Cs

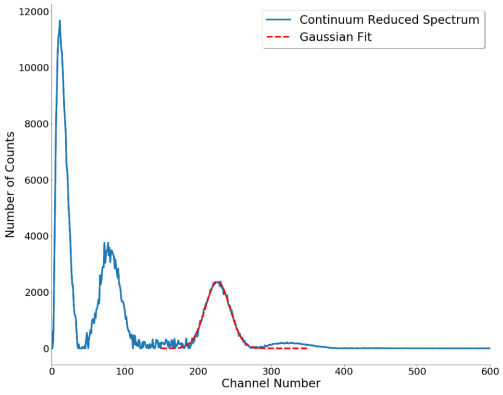

(b) Peak location of ^{137}Cs 624 keV conversion electron lines in 227 channel

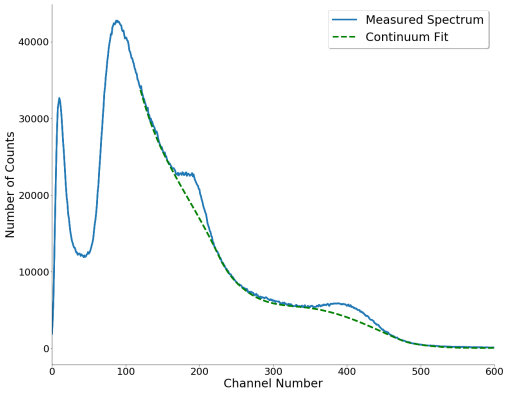

(c) Measured spectrum ^{207}Bi

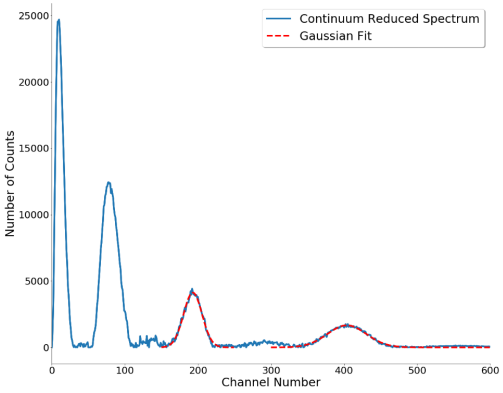

(d) Peak locations of ^{207}Bi 481 keV and 975 keV conversion electron lines in channels 193 and 404

Figure 33. Measured spectra of ^{137}Cs, and ^{207}Bi sources used for the energy calibration of the vertical set-up. Figures on left show measured spectra of sources with background fit. Figures on the right depict background subtracted spectra of sources with a Gaussian fitted conversion electrons peaks.

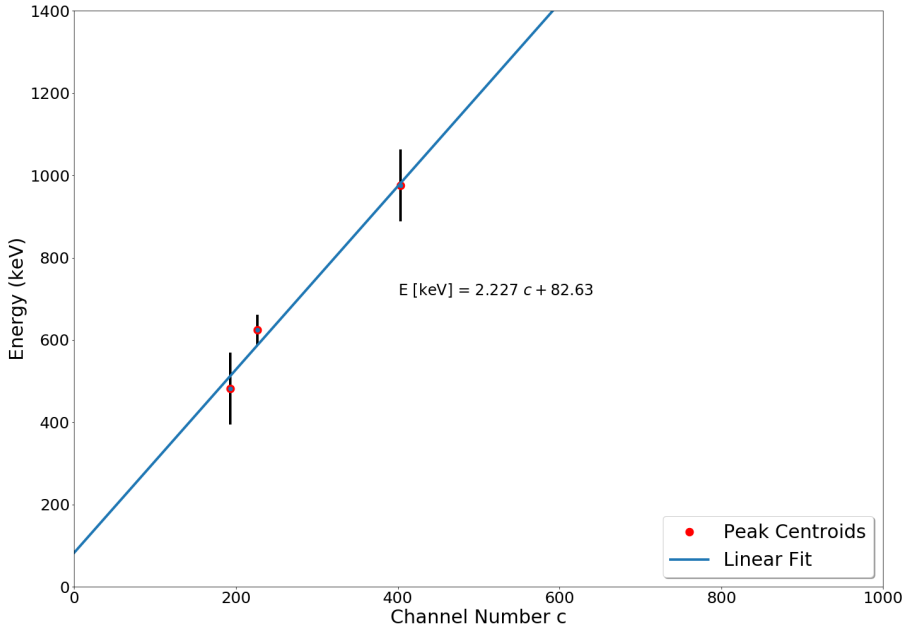

Figure 34. Graph depicting the energy calibration curve of the vertical set-up. The energy calibration function resulting from the linear fit is E (keV) = 2.227c + 82.63, where c is the channel number.

$$\frac{\partial \epsilon_{\text{int}}}{\partial A} = -\frac{C}{2At \cdot A^2} = -\frac{128503 \text{ counts}}{2 \cdot (572.8\,\text{Bq})^2 \cdot 300.149\,\text{s} \cdot 0.5} = -1.300\,788\,432\,399\,524\,2 \times 10^{-3}.$$

$$\frac{\partial \epsilon_{\text{int}}}{\partial t} = -\frac{C}{2At \cdot t^2} = -\frac{128503 \text{ counts}}{2 \cdot 572.8\,\text{Bq} \cdot (300.149\,\text{s})^2 \cdot 0.5} = -2.486\,362\,134\,726\,66 \times 10^{-3}.$$

The uncertainty of beta detection efficiency can now be calculated using the variance formula

$$
\begin{aligned}
\delta\epsilon_{\text{int}} &= \left(\left(\frac{\partial\epsilon_{int}}{\partial C}\cdot\delta C\right)^2+\left(\frac{\partial\epsilon_{int}}{\partial\epsilon_{\text{geom}}}\cdot\delta\epsilon_{\text{geom}}\right)^2+\left(\frac{\partial\epsilon_{int}}{\partial A}\cdot\delta A\right)^2+\left(\frac{\partial\epsilon_{int}}{\partial t}\cdot\delta t\right)^2\right)^{\frac{1}{2}} \\
&= \left(\left(5.807\,353\,319\,903\,871\times10^{-6}\cdot0.01\right)^2+\left(-1.4925246473352143\cdot0.10\right)^2\right. \\
&+ \left(-1.300\,788\,432\,399\,524\,2\times10^{-3}\cdot0.05\right)^2 \\
&+ \left.\left(-2.486\,362\,134\,726\,66\times10^{-3}\cdot1\times10^{-9}\right)^2\right)^{\frac{1}{2}} \\
&= 0.14925247890457563.
\end{aligned}
$$

As a result, the beta detection efficiency for the horizontally oriented scintillator is (0.75 ± 0.15). The beta detection efficiency for the vertically oriented scintillator can be calculated similarly and results in (0.65 ± 0.11). Results were rounded using the 15-unit rule.

The light collection capability of the set-ups was estimated by comparing the numerical value of the slope of the energy calibration curve. The energy calibration curve with a lesser slope means better light collection capability. As was determined earlier, the slope of the energy calibration curve of the horizontal set-up was 0.6561. For the vertical set-up, the slope was 2.227, which relates around 3.4 times better light collection capability for the horizontal set-up. Also, by plotting the intrinsic efficiency as a function of the minimum pulse amplitude (see Fig. 35), we can again see that the orientation has such a drastic effect on the light collection capability of the system.

In conclusion, the beta detection efficiency of the horizontal set-up was slightly better than with the vertical set-up. However, the difference was about ten percentage points, which still falls within the margin of error. However, the light collection capability of the horizontal set-up was approximately 3.4 times better than with the vertical set-up, which suggests that the top monitoring configuration might be a better option for the contamination monitoring system than the side monitoring configuration.

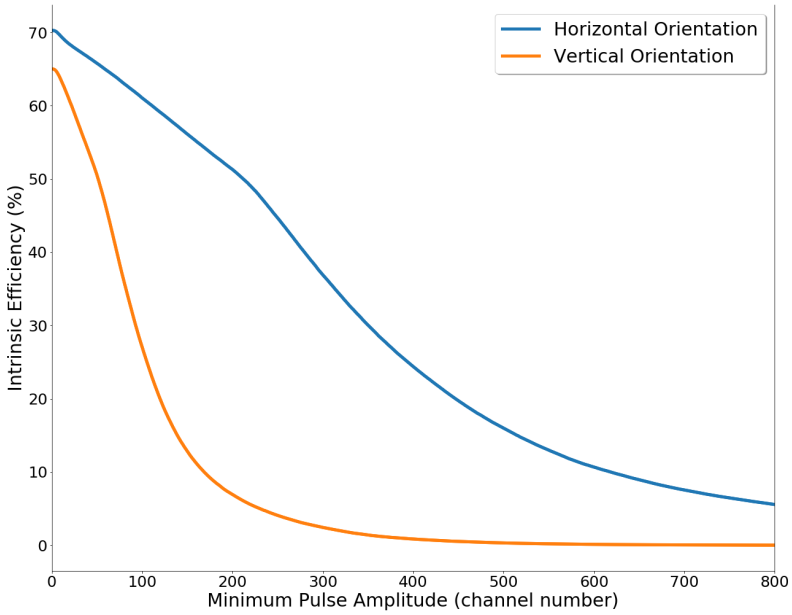

Figure 35. Intrinsic efficiency plotted against the minimum pulse amplitude for the horizontally and vertically oriented set-ups.

7.2 Studies with the Top Monitoring Configuration

7.2.1 Signal Separation Using Pulse Shape Discrimination

The goal of this experiment was to test the separation of scintillation signals by using the PSD technique explained in Section 6.5. Signal separation was investigated with both experimental set-ups: the triple-layer phoswich design (see Section 6.3) and the cylindrical phoswich design (see Section 6.4). The measurement set-ups for the triple-layer phoswich and cylindrical phoswich designs are depicted in Figs. 37 and 36 and measurement parameters are shown in Table 10. For this experiment, ^{137}Cs was used as a radioactive source.

The spectrum of the ^{137}Cs source measured with the triple-layer phoswich design is depicted in Fig. 39a. Because no PSD analysis was performed to produce the plot, the spectrum contains scintillation signals from three different scintillating materials. From the figure, it is easy to identify the 662 keV gamma-ray peak at channel number of around 500. It would be impossible to deduce beta detection efficiency of the plastic scintillator because the spectrum contains gamma-ray counts from the inorganic scintillators.

Performing PSD analysis with using a Python script and by plotting the short/long

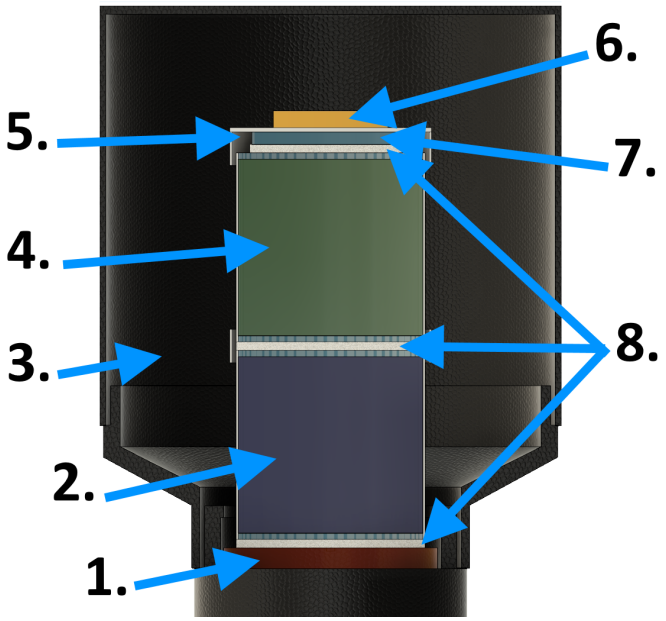

Figure 36. Cross-sectional view of the measurement set-up using triple-layer phoswich design. 1 - Photocathode, 2 - CsI(Na) scintillator, 3 - Light-tight enclosure, 4 - NaI(Tl) scintillator, 5 - Specular reflector, 6 - Radioactive calibration source, 7 - Eljen EJ-212 plastic scintillator, 8 - Optical grade silicon grease.

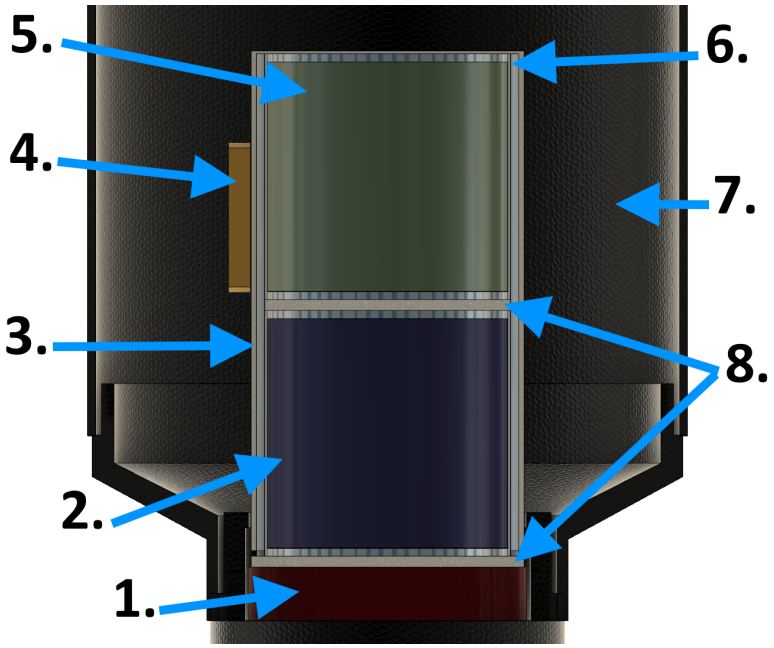

Figure 37. Cross-sectional view of the measurement set-up using cylindrical phoswich design. 1 - Photocathode, 2 - CsI(Na) scintillator, 3 - Specular reflector, 4 - Radioactive calibration source, 5 - NaI(Tl) scintillator, 6 - Eljen EJ-212 plastic scintillator, 7 - Light-tight enclosure, 8 - Optical grade silicon grease.

Table 10. Parameters for measurement. See CAEN DT5730 manual for description of the following parameters [22].

Parameter	
Measurement Time, s	300
Voltage, V	750
Discriminator Mode	Leading Edge
Threshold, lsb	15
Trigger Holdoff, ns	200
Input Smoothing, samples	16
Energy Coarse Gain, fC/lsb	10
Gate, ns	1600
Short Gate, ns	150
Pre-Gate, ns	100

pulse ratio as a function of the long pulse (as was described in Section 6.5) results in Fig. 38a. From the plot, we can see three regions of pulses: the lowest region is the CsI(Na) scintillation signal, which has the longest pulse time. On top of the CsI(Na) signal area is NaI(Tl) signal region, and the PS signal part can be seen closest to the y-axis. From Fig. 38b, we can estimate that a pure PS spectrum can be obtained by accepting only pulses with PSD parameter greater than 0.4 (shown by the red line in Fig. 43 b)

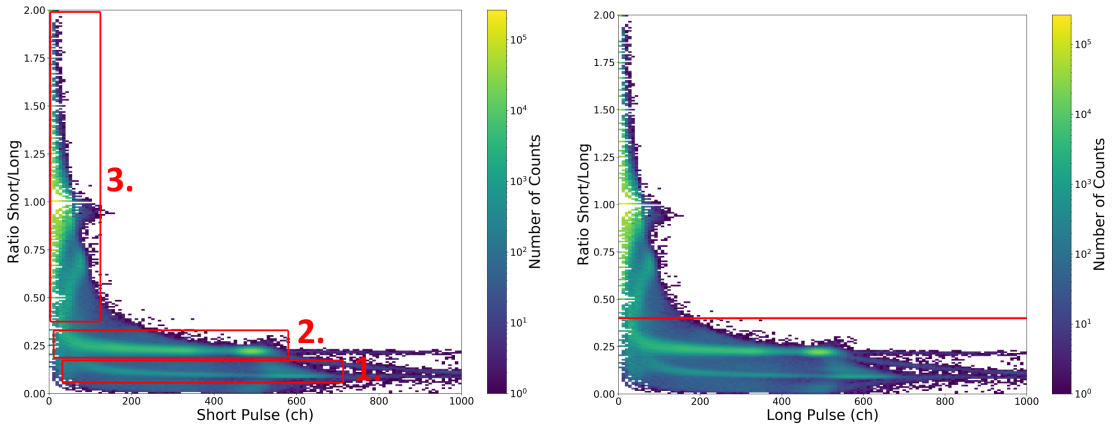

(a) **(b)**

Figure 38. Figure (a): PSD ratio plot depicting the separated scintillation signals for triple-layer phoswich design: 1 - CsI(Na), 2 - NaI(Tl), 3 - PS. Figure (b): PSD ratio plot showing the defined PSD cut parameter of 0.4 (red line).

By plotting the measured energy spectrum with PSD cut parameter values of 0.4 - 2.0 results in Fig. 39b which shows the beta/conversion electron spectrum of ^{137}Cs measured with the PS. On the other hand, plotting the measured energy spectrum with PSD cut parameter values of 0.0 to 0.4 results in Fig. 39c, which shows the gamma-ray spectrum measured with both NaI(Tl) and CsI(Na) scintillators. We could further separate inorganic scintillator signals by specifying the PSD cut parameter to be around 0.2, which results in Figs. 40b and 40c.

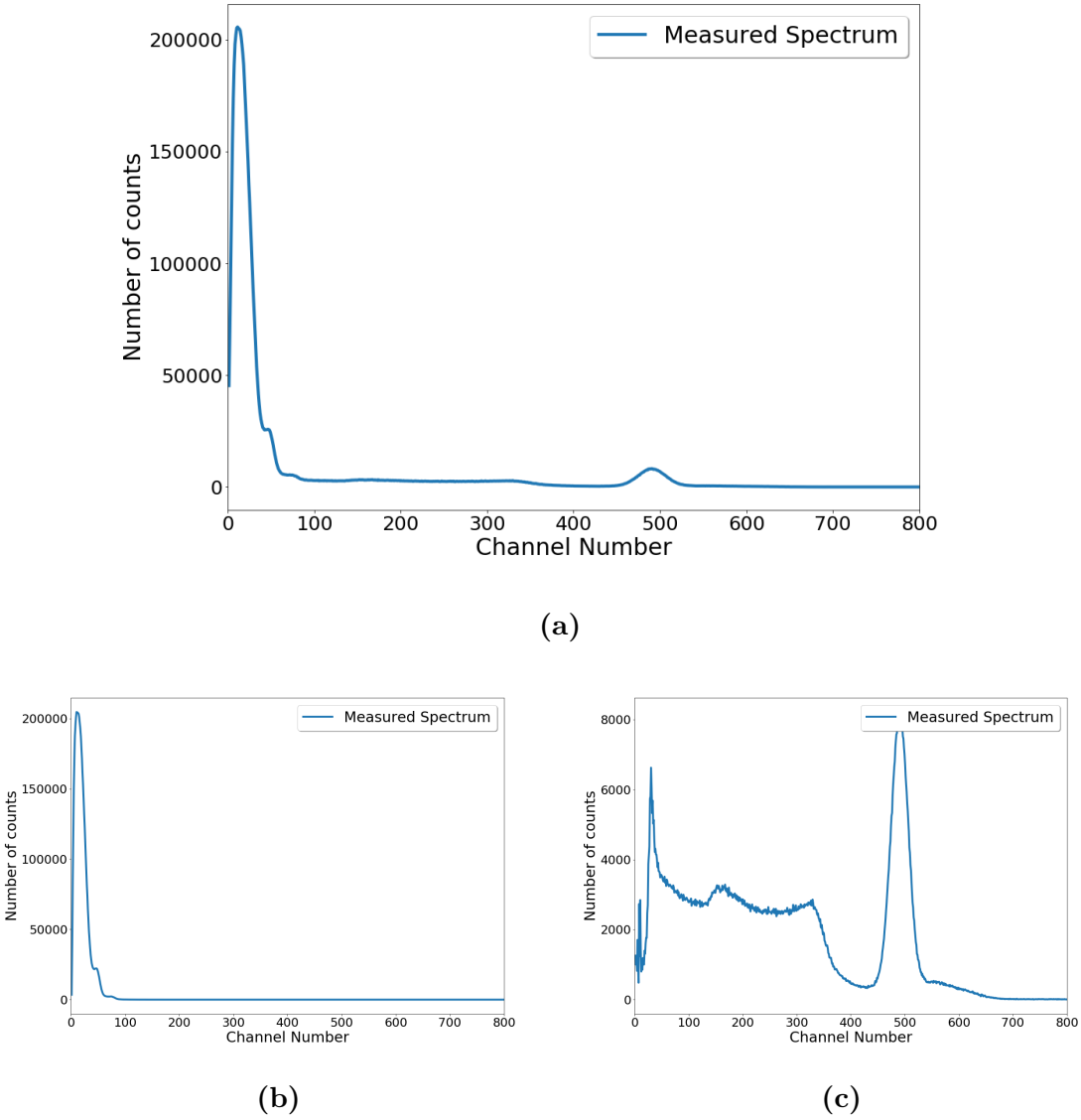

Figure 39. Result of the PSD analysis for triple-layer phoswich design. Figure (a): ^{137}Cs spectrum without PSD analysis. Figure (b): Separated beta/conversion electron spectrum of ^{137}Cs using PSD cut parameter of 0.4 to 2.0. Figure (c): Separated gamma spectrum of ^{137}Cs using PSD cut parameter of 0.0 to 0.4.

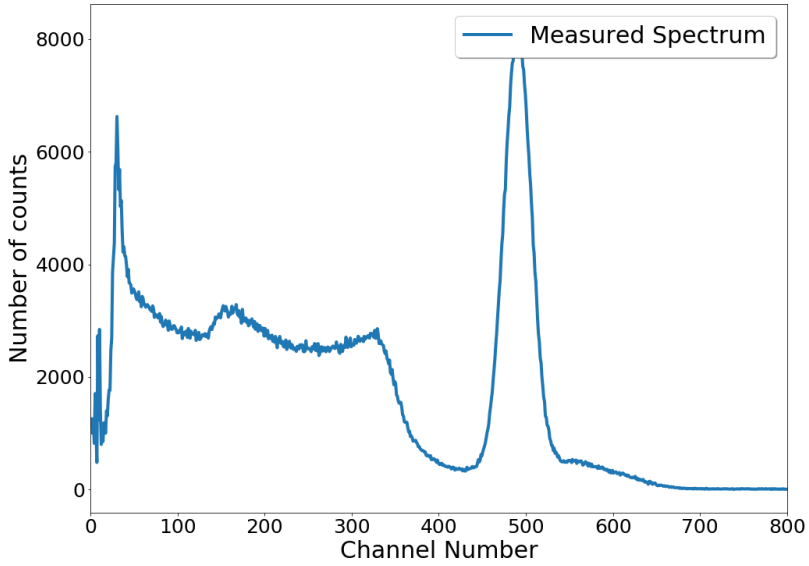

(a)

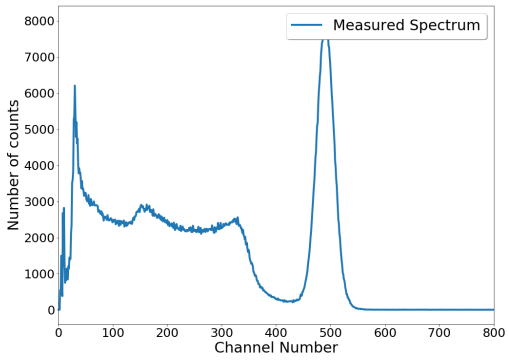

(b)

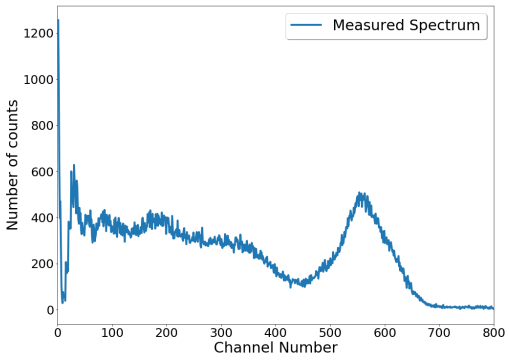

(c)

Figure 40. Result of the PSD analysis for triple-layer phoswich design. Figure (a): Separated gamma spectrum of ^{137}Cs using PSD cut parameter of 0.0 to 0.4. Figure (b): Separated gamma spectrum of ^{137}Cs measured with NaI(Tl) scintillator using PSD cut parameter of 0.2 to 0.4. Figure (c): Separated gamma spectrum of ^{137}Cs measured with CsI(Na) scintillator using PSD cut parameter of 0.0 to 0.2.

Similarly, the same procedure for separating scintillator signals with the cylindrical phoswich design was tested. Fig. 42a shows the measured energy spectrum of ^{137}Cs by using the given design. Application of PSD analysis results in the plots shown in Figs. 41a and 41b.

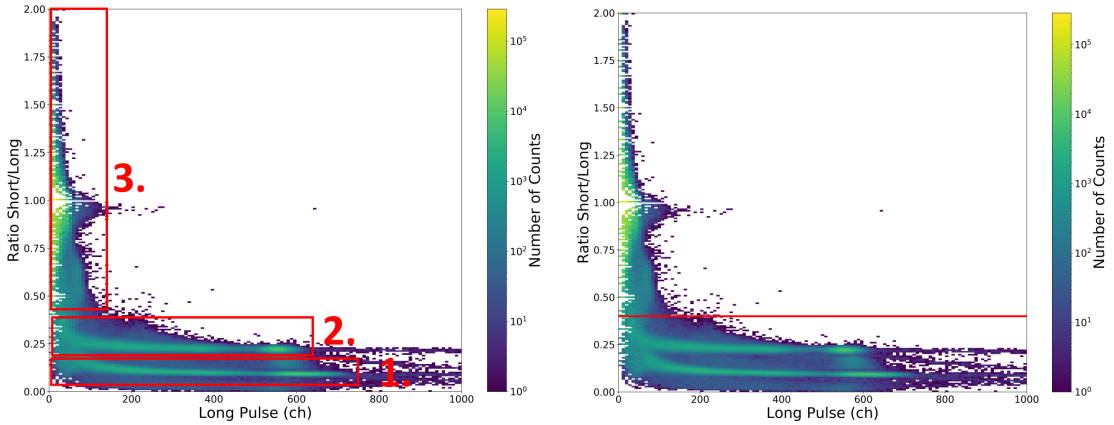

Figure 41. Figure (a): PSD ratio plot depicting the separated scintillation signals for cylindrical phoswich design: 1 - CsI(Na), 2 - NaI(Tl), 3 - PS. Figure (b): PSD ratio plot showing the defined PSD cut parameter of 0.4 (red line).

From the Fig. 41b, the PSD cut parameter can be specified to be around 0.4. Applying a PSD cut parameter range of 0.4 to 2.0 results in the beta/conversion electron spectrum of the PS shown in Fig. 42b. The gamma-ray spectrum measured by the inorganic scintillators can be plotted by applying a PSD cut parameter range of 0.0 to 0.4 and the results is depicted in Fig. 42c.

In conclusion, separating the scintillation signals by using PSD in both the triple-layer phoswich design and the cylindrical phoswich design was feasible.

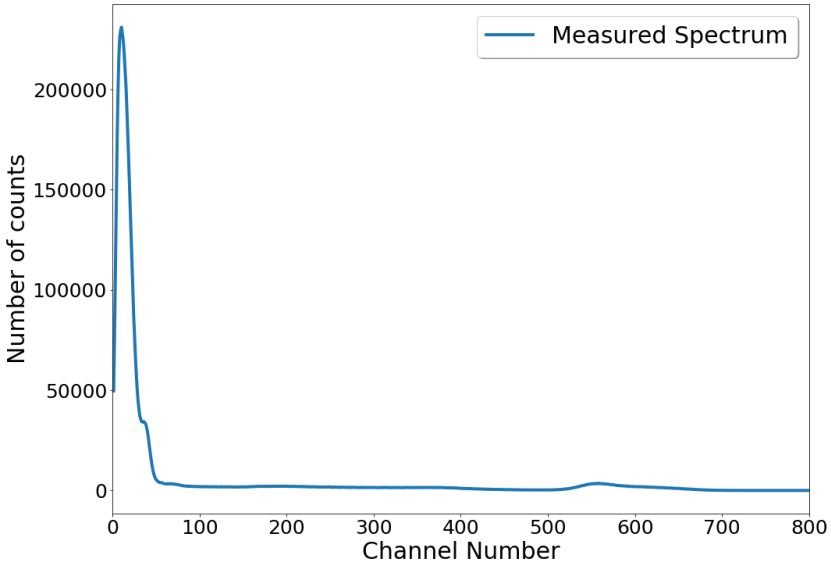

(a)

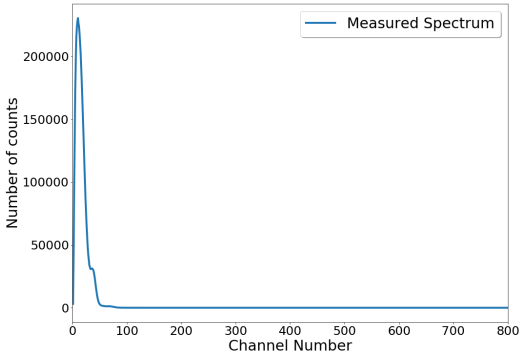

(b)

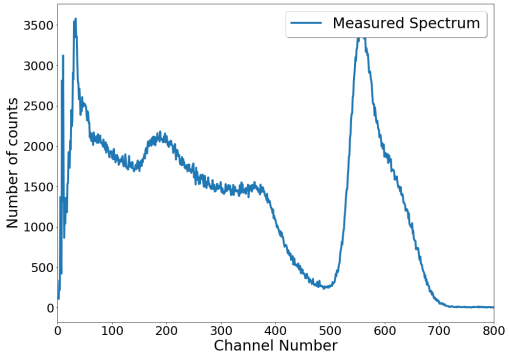

(c)

Figure 42. Result of the PSD analysis for cylindrical phoswich design. Figure (a): ^{137}Cs spectrum without PSD analysis. Figure (b): Separated beta/conversion electron spectrum of ^{137}Cs uing PSD cut parameter of 0.4 to 2.0. Figure (c): Separated gamma spectrum of ^{137}Cs using PSD cut parameter of 0.0 to 0.4.

7.2.2 Impact of the Gamma-ray Detector

The objective of this measurement was to test the impact of the gamma-ray detector on the beta detection efficiency and the light collection capability of the plastic scintillator when the scintillating materials are stacked as phoswich. The test was performed with the triple-layer phoswich design (see Section 6.3), for which detailed measurement set-up and parameters are depicted in Fig. 37 and Table 10. The horizontal set-up of the scintillator test system (see Section 6.2), which has no gamma-ray detector, was used as a reference set-up for comparison of results. ^{90}Sr was used as the source of beta particles.

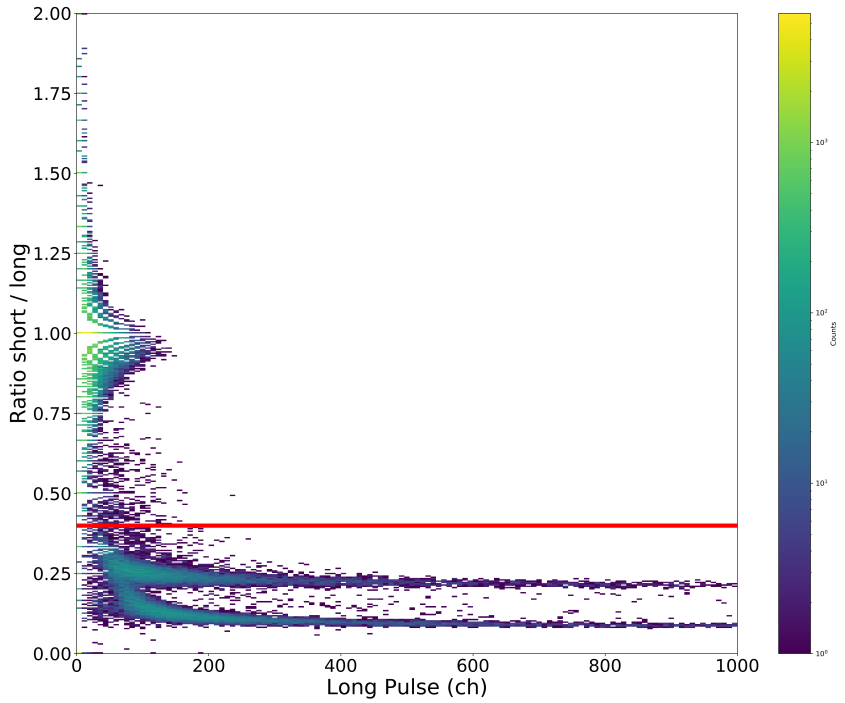

Figure 43. PSD ratio plot showing defined PSD cut parameter of 0.42 (red line).

After the measurement, PSD analysis was performed on the data to separate the counts caused by background radiation interacting in the inorganic scintillators. Fig. 43 depicts the resulting plot from PSD analysis, and it clearly shows that a scintillation response was observed in all three scintillating materials. Therefore, the signal separation was necessary to calculate the counts recorded in the plastic scintillator. From the figure, the PSD cut parameter was estimated to be 0.42. Plotting the measured ^{90}Sr spectrum with PSD cut parameter of 0.42 results in Fig.

44

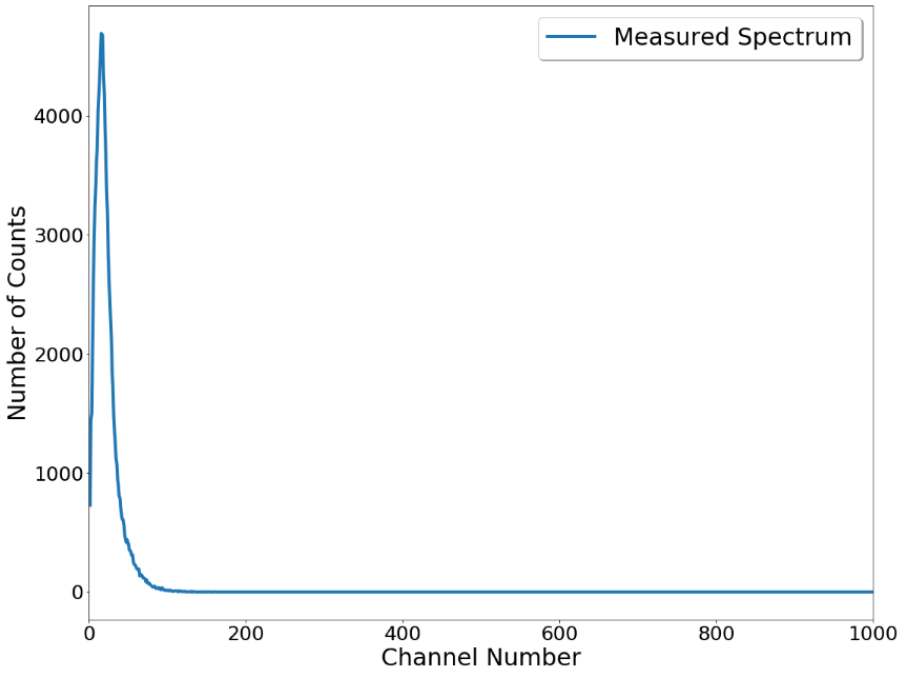

Figure 44. The measured spectrum of ^{90}Sr using the PSD cut parameter of 0.42. Total recorded counts: 115201.

As can be seen from the plot, the spectrum of ^{90}Sr is shifted to very low energies, and the effect is even more exaggerated than what was seen in Section 7.1.4 when the impact of scintillator orientation was examined. The energy calibration was done for the triple-layer phoswich design to evaluate the light collection capability of the system. The energy calibration was done using ^{137}Cs and ^{207}Bi conversion electron sources, which measured spectra are shown in Fig. 45

Asymmetric least squares method was used to account for the background in the spectra to enable easier Gaussian fitting of the conversion electron peaks. Plotting the centroids of the peaks with matching conversion electron energy value and performing linear fit to data results in the energy calibration curve depicted in Fig. 46.

The beta detection efficiency can be estimated using equation (12) and results in

$$\epsilon_{\text{int}} = \frac{115201 \text{ counts}}{2 \cdot 570.4\,\text{Bq} \cdot 297.594\,\text{s} \cdot 0.50} = 0.6786604821.$$

In the above equation, the geometric efficiency of (0.50 ± 0.1) was used. Uncertainty for beta detection efficiency can be estimated using propagation of uncertainty where the partial derivative of the above equation is taken with respect to error

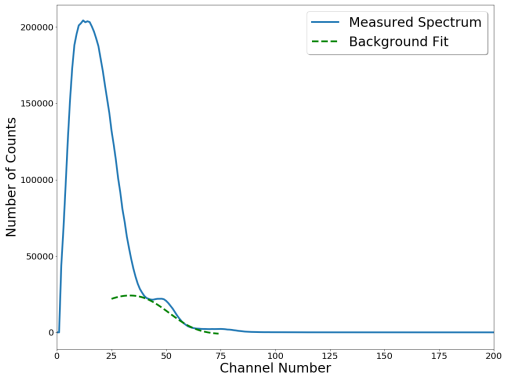

(a) Measured spectrum of ^{137}Cs

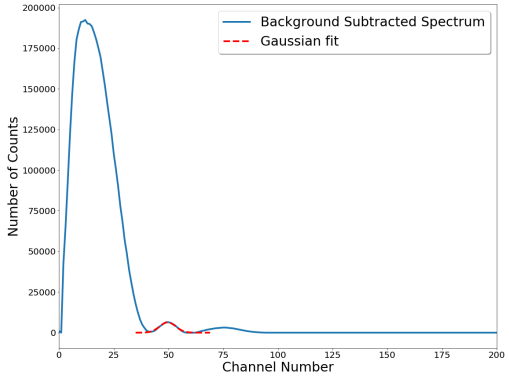

(b) Peak location of ^{137}Cs 624 keV conversion electron line on channel number 49

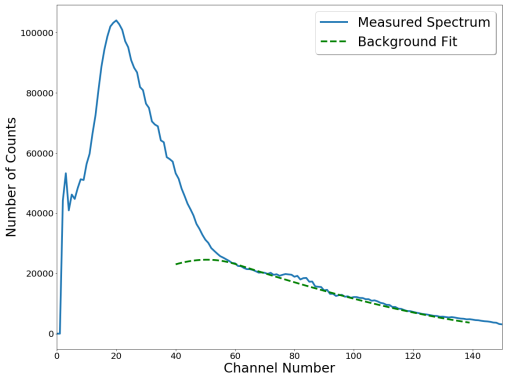

(c) Measured spectrum ^{207}Bi

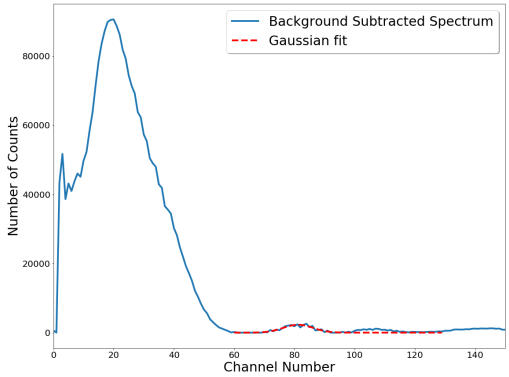

(d) Peak location of ^{207}Bi 975 keV conversion electron line on channel number 83

Figure 45. Measured spectra of ^{137}Cs, and ^{207}Bi sources used for the energy calibration of the triple-layer phoswich design. Figures on left show measured spectra of sources with background fit. Figures on the right depict background subtracted spectra of sources with a Gaussian fitted conversion electrons peaks.

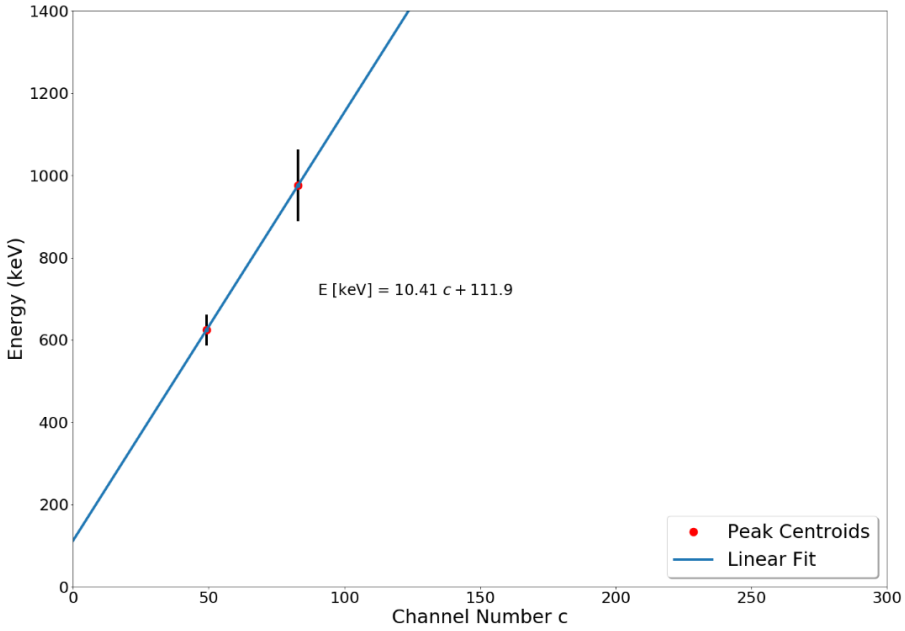

Figure 46. Energy calibration curve of triple-layer phoswich design. Energy calibration function resulting from linear fit is E (keV) $= 10.41c + 111.9$, where c is the channel number.

causing variables. For equation (12), uncertainty is produced from geometrical efficiency, activity, and estimates of live time and number of recorded counts in the spectrum. Now, taking the partial derivative of equation of beta counting efficiency with respect to the number of counts, geometrical efficiency, activity and live time leads into

$$\frac{\partial \epsilon_{\text{int}}}{\partial C} = \frac{1}{2At \cdot \epsilon_{\text{geom}}} = \frac{1}{2 \cdot 570.4\,\text{Bq} \cdot 297.594\,\text{s} \cdot 0.5} = 5.891\,098\,880\,435\,775 \times 10^{-6}.$$

$$\frac{\partial \epsilon_{\text{int}}}{\partial \epsilon_{\text{geom}}} = -\frac{C}{2At \cdot \epsilon_{\text{geom}}^2} = -\frac{115201\ \text{counts}}{2 \cdot 570.4\,\text{Bq} \cdot 297.594\,\text{s} \cdot 0.5^2} = -1.3573209642501634.$$

$$\frac{\partial \epsilon_{\text{int}}}{\partial A} = -\frac{C}{2At \cdot A^2} = -\frac{115201\ \text{counts}}{2 \cdot (570.4\,\text{Bq})^2 \cdot 297.594\,\text{s} \cdot 0.5} = -1.189\,797\,479\,181\,419\,6 \times 10^{-3}.$$

$$\frac{\partial \epsilon_{\text{int}}}{\partial t} = -\frac{C}{2At \cdot t^2} = -\frac{115201 \text{ counts}}{2 \cdot 570.4\,\text{Bq} \cdot (297.594\,\text{s})^2 \cdot 0.5} = -2.280\,491\,146\,075\,128 \times 10^{-3}.$$

The uncertainty of beta counting efficiency can now be calculated using the variance formula

$$\begin{aligned}
\delta\epsilon_{\text{int}} &= \left(\left(\frac{\partial \epsilon_{int}}{\partial C} \cdot \delta C \right)^2 + \left(\frac{\partial \epsilon_{int}}{\partial \epsilon_{\text{geom}}} \cdot \delta \epsilon_{\text{geom}} \right)^2 + \left(\frac{\partial \epsilon_{int}}{\partial A} \cdot \delta A \right)^2 + \left(\frac{\partial \epsilon_{int}}{\partial t} \cdot \delta t \right)^2 \right)^{\frac{1}{2}} \\
&= \left(\left(5.891\,098\,880\,435\,775 \times 10^{-6} \cdot 0.01 \right)^2 + \left(-1.3573209642501634 \cdot 0.10 \right)^2 \right. \\
&+ \left(-1.189\,797\,479\,181\,419\,6 \times 10^{-3} \cdot 0.05 \right)^2 \\
&+ \left. \left(-2.280\,491\,146\,075\,128 \times 10^{-3} \cdot 1 \times 10^{-9} \right)^2 \right)^{\frac{1}{2}} \\
&= 0.1357321094619048.
\end{aligned}$$

As a result, the beta detection efficiency for triple-layer phoswich design was (0.68 ± 0.14). The result was rounded using the 15-unit rule. For comparison, the beta detection efficiency of the horizontal setup was determined to be (0.75 ± 0.15) (see Section 7.1.4).

The light collection capability of the triple-layer phoswich design was estimated by comparing the numerical value of the slope of the energy calibration curve. The energy calibration curve with a lesser slope means better light collection capability. As was determined earlier, the slope of the energy calibration curve of the triple-layer phoswich design was 10.41. For comparison, the horizontal set-up in Section 7.1.4, the slope was 0.6561, which relates around 16 times better light collection capability for the horizontal set-up. Also, by plotting the intrinsic efficiency as a function of the minimum pulse amplitude (see Fig. 47), we can again see that the gamma-ray detector has such a drastic effect on the light collection capability of the system.

In conclusion, the beta detection efficiency of the plastic scintillator was not strongly affected by the gamma-ray detector. Compared to the horizontal setup in Section 7.1.4, the beta detection efficiency was around 7 percent lower. However, the light collection from the plastic scintillator was severely impacted by the gamma-ray

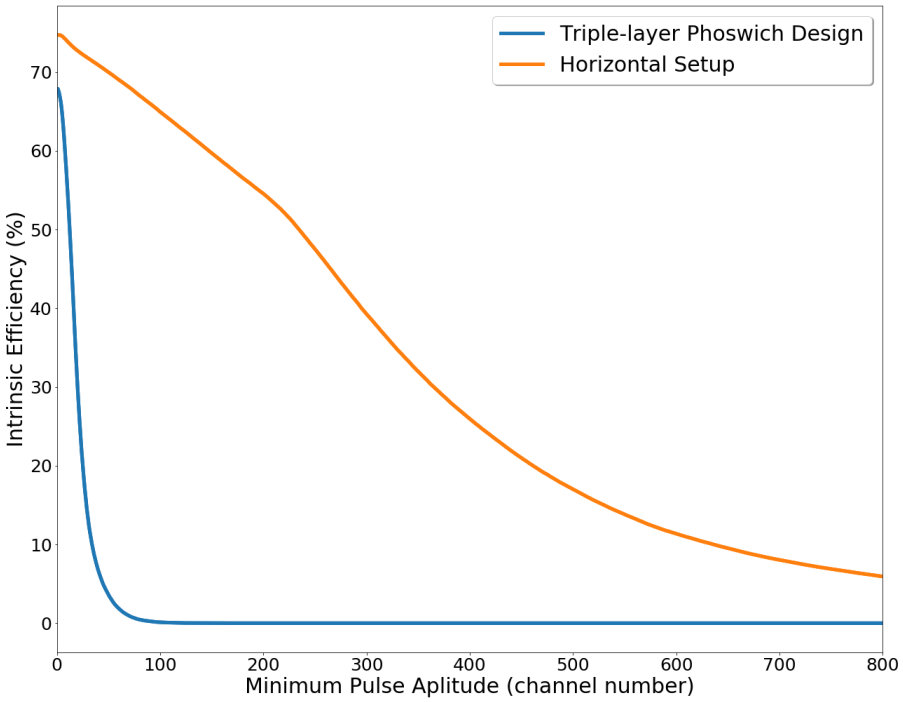

Figure 47. Intrinsic efficiency graph as a function of channel number for triple-layer phoswich design and horizontal setup.

detector leading to almost 16 times worse light collection than without the gamma-ray detector. This inferior light collection capability is presumably caused by the plastic scintillation light being attenuated inside the crystals and entrance windows of the gamma-ray detector. Therefore, to use the top-monitoring configuration as the contamination monitoring system, optically high-quality crystals, and entrance windows should be used to compensate for the strong attenuation of scintillation light in the gamma-ray detector.

7.3 Studies with the Side Monitoring Configuration

7.3.1 Impact of Scintillator Shaping and Uniformity of Light Collection

The objective of this measurement was to test the effect of the plastic scintillator shaping on the beta detection efficiency. As described in Section 6.4, for the cylindrical phoswich design, a sheet of PS was first heated to the softening point of material and then was bent into a hollow cylinder shape, which might have altered the performance of PS.

The secondary objective of this measurement was to test the uniformity of light

collection in the cylindrical phoswich design. The uniformity of light collection in this context means how much light the PMT collects when the radioactive source is moved across the cylinder wall of the PS. The measurement was made for three different locations an cylinder wall: the upper, center, and lower parts, which are shown in Fig. 48. The parameters used in this measurement are depicted in Table 10. ^{90}Sr was used as a source of beta particles.

Similar to the triple-layer phoswich design, PSD analysis was needed to separate scintillation signals in the phoswich system. By performing the signal separation, a separated spectrum from the PS can be obtained, as in Fig. 49

As the figure depicts, the spectra vary considerably between the upper section of the PS in contrast to center and lower parts, which indicates a difference in the light collection. Subsequently, the beta detection efficiency was calculated for each measurement set-up using equation (12) and for upper section results in

$$\epsilon_{\text{int}} = \frac{100546 \text{ counts}}{2 \cdot 570.4\,\text{Bq} \cdot 292.321\,\text{s} \cdot 0.46} = 0.6554467856.$$

For the cylindrical phoswich design, the geometrical efficiency was estimated to be (0.46 ± 0.10), which is the lowest among experimental set-ups used in this thesis. The low geometrical efficiency is the result of a cylinder face, which reduces the solid angle compared to the flat face. As observed in the previous sections, the uncertainty of total beta detection efficiency results from geometrical efficiency, activity, live time estimate, and counts in the spectrum estimate. Using propagation of uncertainty and taking partial derivatives with respect to its error causing variables results

$$\frac{\partial \epsilon_{\text{int}}}{\partial C} = \frac{1}{2At \cdot \epsilon_{\text{geom}}} = \frac{1}{2 \cdot 570.4\,\text{Bq} \cdot 292.321\,\text{s} \cdot 0.46} = 6.518\,874\,799\,429\,111 \times 10^{-6}.$$

$$\frac{\partial \epsilon_{\text{int}}}{\partial \epsilon_{\text{geom}}} = -\frac{C}{2At \cdot \epsilon_{\text{geom}}^2} = -\frac{100546 \text{ counts}}{2 \cdot 570.4\,\text{Bq} \cdot 292.321\,\text{s} \cdot 0.46^2} = -1.4248843164856508.$$

$$\frac{\partial \epsilon_{\text{int}}}{\partial A} = -\frac{C}{2At \cdot A^2} = -\frac{100546 \text{ counts}}{2 \cdot (570.4\,\text{Bq})^2 \cdot 292.321\,\text{s} \cdot 0.46} = -1.149\,100\,255\,230\,363\,4 \times 10^{-3}.$$

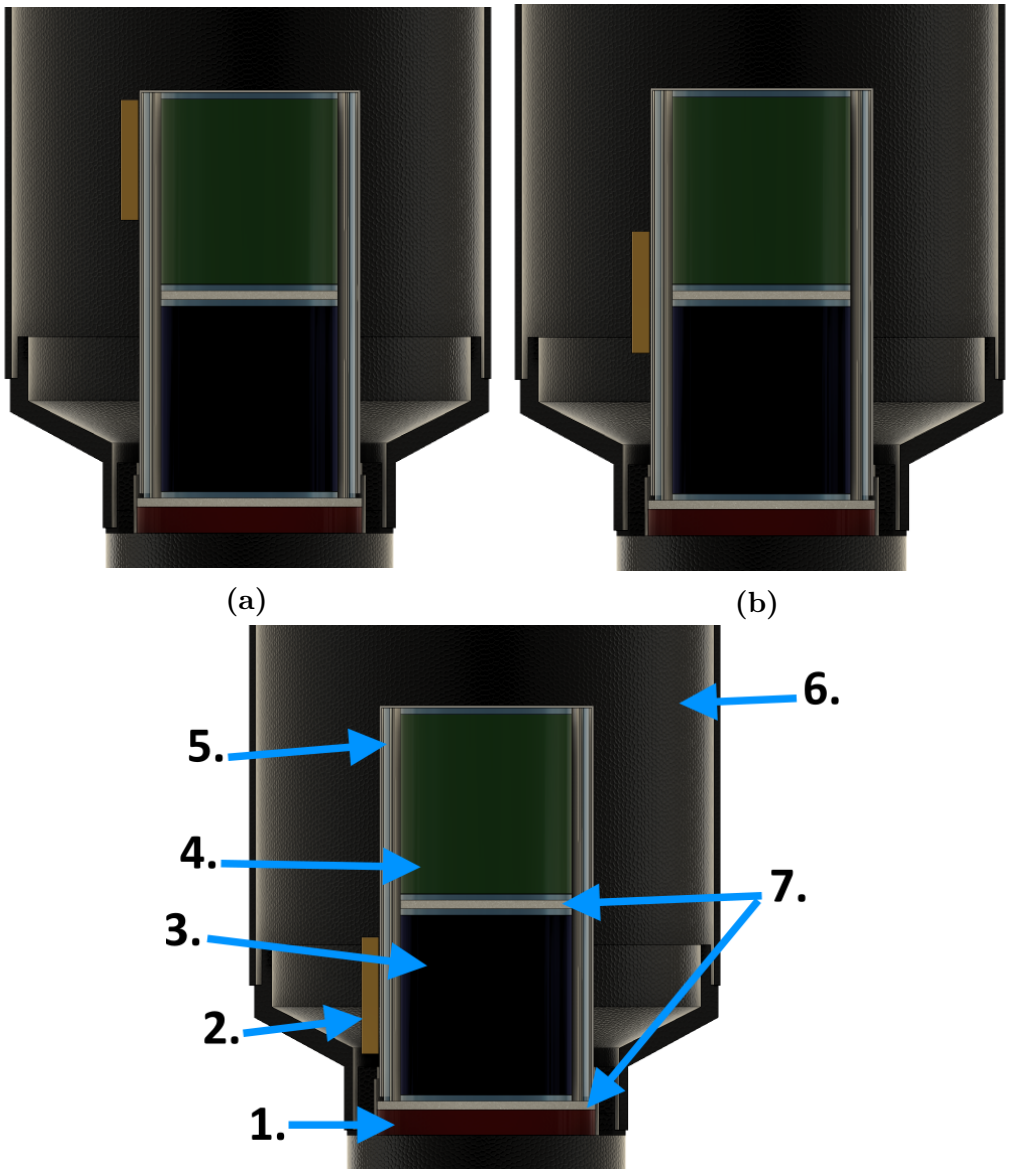

Figure 48. Cross-sectional view of the measurement set-up. 1 - Photocathode, 2 - Radioactive calibration source, 3 - CsI(Na) scintillator, 4 - NaI(Tl) scintillator, 5 - Eljen EJ-212 plastic scintillator, 6 - Light-tight enclosure, 7 - Optical grade silicon grease.

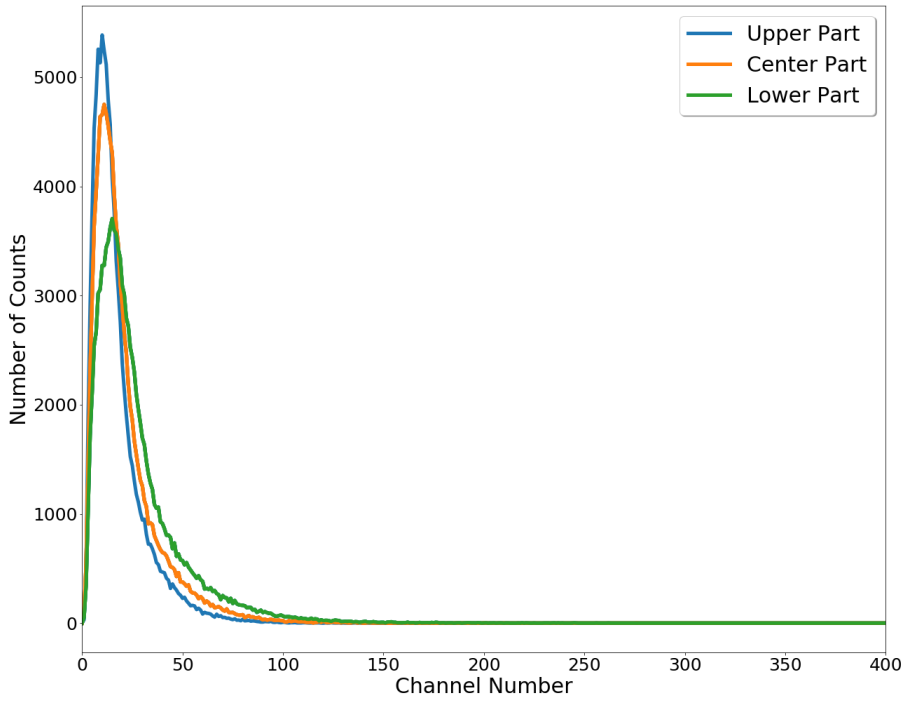

Figure 49. The measured spectrum of ^{90}Sr using the PSD cut parameter of 0.45. Total recorded counts in the spectrum for upper part: 100546, for center part: 106764 and for lower part: 109868.

$$\frac{\partial \epsilon_{\text{int}}}{\partial t} = -\frac{C}{2At \cdot t^2} = -\frac{100546 \text{ counts}}{2 \cdot 570.4\,\text{Bq} \cdot (292.321\,\text{s})^2 \cdot 0.46} = -2.242\,215\,870\,852\,245\,4 \times 10^{-3}.$$

Now, the uncertainty of beta detection efficiency can be calculated using variance formula

$$
\begin{aligned}
\delta\epsilon_{\text{int}} &= \left(\left(\frac{\partial\epsilon_{int}}{\partial C}\cdot\delta C\right)^2+\left(\frac{\partial\epsilon_{int}}{\partial\epsilon_{\text{geom}}}\cdot\delta\epsilon_{\text{geom}}\right)^2+\left(\frac{\partial\epsilon_{int}}{\partial A}\cdot\delta A\right)^2+\left(\frac{\partial\epsilon_{int}}{\partial t}\cdot\delta t\right)^2\right)^{\frac{1}{2}} \\
&= \left(\left(6.518\,874\,799\,429\,111\times10^{-6}\cdot0.01\right)^2+\left(1.4248843164856508\cdot0.10\right)^2\right. \\
&+ \left(-1.149\,100\,255\,230\,363\,4\times10^{-3}\cdot0.05\right)^2 \\
&+ \left.\left(-2.242\,215\,870\,852\,245\,4\times10^{-3}\cdot1\times10^{-9}\right)^2\right)^{\frac{1}{2}} \\
&= 0.14248844323225146.
\end{aligned}
$$

As a result, the total beta detection efficiency of the upper part was (0.66 ± 0.15). Similarly, the overall beta detection efficiency of the center and lower parts were (0.7 ± 0.2) and (0.7 ± 0.2). The result was rounded using the 15-unit rule

The uniformity of light collection capability was studied by plotting the intrinsic efficiency graph as a function of a minimum pulse amplitude for upper, center and lower parts of the PS and the results are shown in Fig. 50. As the figure shows, the intrinsic efficiency graph of the upper part and center part undergoes a quicker drop in efficiency compared to the lower part, which indicates that the light collection capability drops when the beta particles interact in the PS further away from the PMT window.

In conclusion, the beta detection efficiency of the cylindrical PS was not weakened by the shaping of the PS. Therefore, as there are currently no factory-made hollow cylindrical plastic scintillators available, the shaping procedure introduced in Section 6.4 could be used to make such cylindrical PS for the contamination monitoring system. Also, the beta detection efficiency was relatively homogeneous in the whole length of the cylinder. However, because the light collection capability was not uniform in the plastic scintillator, it could be problematic if a considerably longer cylindrical PS is needed in the side monitoring configuration of the contamination monitoring system.

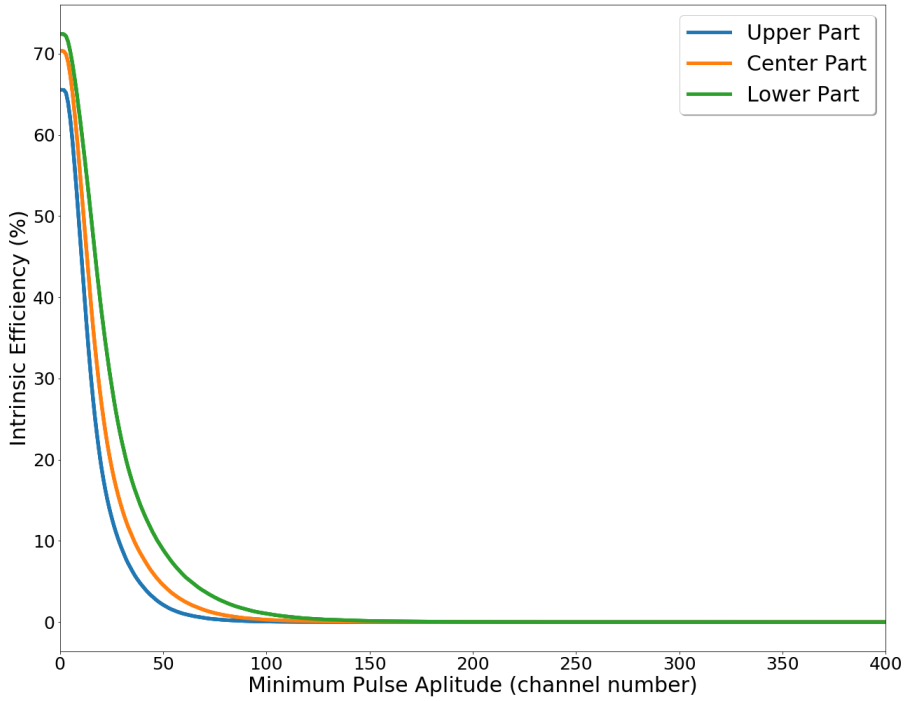

Figure 50. Intrinsic efficiency graph as a function of minimum pulse amplitude in channels.

8 Conclusions

This MSc thesis investigated a prototype contamination monitoring system to be installed in the detector of the next generation radiation monitoring station planned for the Finnish radiation early warning network. Two configurations were studied: top monitoring and side monitoring configurations. In the results, both configurations were seen as feasible options for a contamination monitoring system. However, both configurations had severe drawbacks that must be addressed before the contamination monitoring system could be deployed.

The major drawback of top monitoring configuration was weak light collection from the plastic scintillator. In the top monitoring configuration, the scintillation light from the plastic has to be transmitted through the gamma-ray detector. It was shown in the experiments that most of the light generated in the plastic was either attenuated or lost in the gamma detector leaving only a weak signal to be collected by the electronics following the PMT. In this thesis, the gamma-ray detector was made from separate CsI(Na) and NaI(Tl) scintillators, which were optically coupled together using silicone grease. This setup was relatively complicated and contained several gaps where the light could escape. In addition to this, the optical quality of the inorganic scintillators was relatively poor. Therefore, if the triple-layer phoswich scintillator were to be optically coupled in a factory with high-quality components, it would most likely provide better light collection.

On the other hand, the major drawback in the side monitoring configuration was the non-homogenous light collection from the cylindrical plastic scintillator. In the results, the upper part of the cylinder had a dramatic drop in light collection compared to the lower part of the cylinder. It should be further studied whether the effect was a result of the shaping, or was it due to the improper reflector in the upper part of the cylinder or some other design issue. If light collection is indeed weakened as much, then the side monitoring configuration should be modified to contain a shorter cylindrical PS, and the contamination should be monitored from below the collimator ring, as is shown in the conceptual figure below.

Further research is needed on studying the effects of the plastic scintillator on

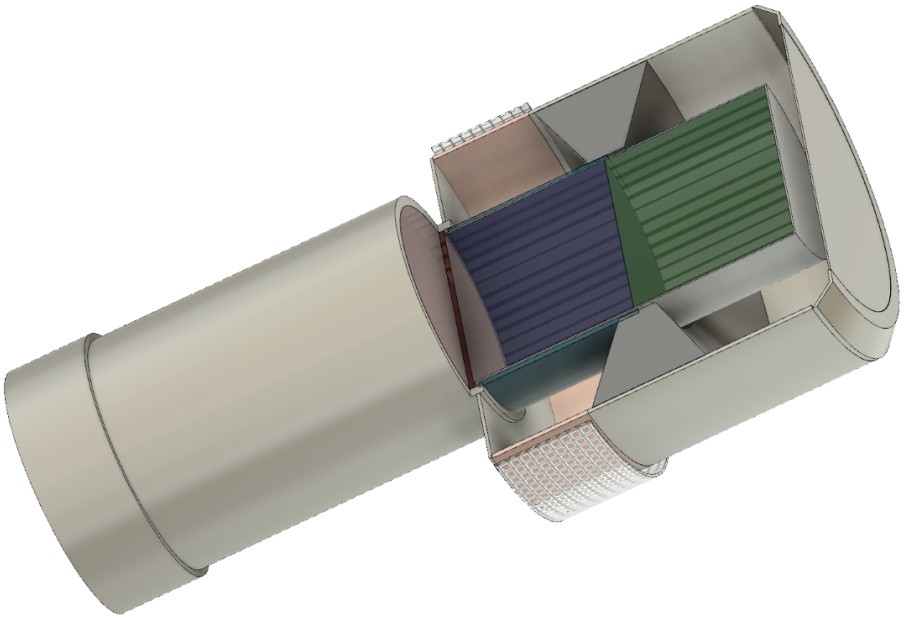

Figure 51. A modified version of the side monitoring configuration of the contamination monitoring system featuring a single beta window.

gamma-ray resolution of the gamma-ray detector in the top monitoring configuration. As the performance of the gamma-ray detector is a number one priority in designing the novel detector, any decrease in gamma-ray resolution is not acceptable. In the side monitoring configuration, the PS should not have any impact on the gamma-ray resolution because the plastic scintillator is not optically coupled to the gamma-ray detector. Therefore, the side monitoring configuration remains a viable option if the top monitoring configuration fails in further studies.

Also, more research should be focused on the implementation of the beta window, which was mostly ignored in this thesis. Design aspects such as window material, support structure, and external protection grid should be studied when designing the beta window for the contamination monitoring system. As for the material aspect, there are at least two potential materials for the window: titanium foil and muscovite mica sheet. With both materials, the window can be made thin enough so that beta radiation can pass it without attenuation and yet be tolerant for extreme environmental conditions. However, because of the thinness of the beta window, in both configurations, an external protective grid would be needed to cover the beta window from impacts by debris or landing of birds, etc. Also, the side monitoring configuration would require a support structure for the beta window as otherwise, the weight of the detector housing would cause the collapse of the beta window. As

for the top monitoring configuration, no support structure is needed because the plastic scintillator would support the beta window.

Lastly, further research is needed on optimizing the reflector material to enable maximum beta efficiency and light collection in the plastic scintillator. In this thesis, metalized Mylar film was found to be a better reflector material than aluminum foil, but no research was done to optimize the thickness of the reflector material. In the experiments, Mylar film with a thickness of 12 µm was used, but metalized Mylar can be made even two µm thick, which would enable lesser attenuation of beta radiation. However, two µm thick film would not be light-tight and could, therefore, weaken the light collection from the plastic scintillator.

In the end, as was demonstrated in this thesis, the contamination monitoring system could be easily incorporated on the planned detector. Because the contamination monitoring system is composed only of thin plastic scintillator and the beta window structure, the system could be integrated at low cost and not significantly increase the complexity of designing and building the detector. In the case of nuclear incidents, the contamination monitoring system would improve the operational capability and reliability of the detector and would, therefore, improve radiation safety in Finland.

References

[1] *The Federal Office for Radiation Protection (Bundesamt für Strahlenschutz, BfS) website*. URL: https://www.bfs.de/EN/topics/ion/environment/air-soil/odl/odl_node.html (visited on 02/07/2020).

[2] K. Hoffman. *Säteilyturvakeskuksen historia 1958 - 2008*. Säteilyturvakeskus, 2008.

[3] J. Lahtinen and J. Koivukoski. "EXTERNAL DOSE RATE MONITORING IN FINLAND: HISTORY, EXPERIENCES AND A GLIMPSE AT THE FUTURE". In: *Radiation Protection Dosimetry* (July 2019). ncz159. ISSN: 0144-8420. DOI: 10.1093/rpd/ncz159. eprint: https://academic.oup.com/rpd/advance-article-pdf/doi/10.1093/rpd/ncz159/28903376/ncz159.pdf. URL: https://doi.org/10.1093/rpd/ncz159.

[4] *Radiation and Nuclear Safety Authority (STUK), Radiation today, website*. URL: https://www.stuk.fi/aiheet/sateily-ymparistossa/sateilytilanne-tanaan (visited on 09/07/2020).

[5] J. Hanafee. *Analysis of beryllium parts for cosmos 954*. Tech. rep. California Univ., 1978. URL: https://inis.iaea.org/search/search.aspx?orig_q=RN:10465597 (visited on 02/03/2020).

[6] *Japan Atomic Energy Agency, Nuclear Data Center, website*. URL: https://wwwndc.jaea.go.jp/cgi-bin/FPYfig (visited on 09/07/2020).

[7] *Radioactive Particles in the Environment: Sources, Particle Characterization and Analytical Techniques*. INTERNATIONAL ATOMIC ENERGY AGENCY, 2011. URL: https://www-pub.iaea.org/MTCD/Publications/PDF/TE_1663_web.pdf (visited on 02/03/2020).

[8] R. Pöllänen et al. *Transport of large particles released in a nuclear accident*. Tech. rep. Finnish Centre for Radiation and Nuclear Safety (STUK), 1995. URL: https://inis.iaea.org/search/search.aspx?orig_q=RN:27040846 (visited on 03/19/2020).

[9] T. Valmari and R. Pöllänen. "Radioaktiiviset aineet ulkoilmassa". In: (2003). URL: http://urn.fi/URN:NBN:fi-fe2014120247803 (visited on 03/19/2020).

[10] W. R. Leo. *Techniques for nuclear and particle physics experiments: a how-to approach*. Springer Science & Business Media, 2012.

[11] G. F. Knoll. *Radiation detection and measurement*. John Wiley & Sons, 2010.

[12] H. Bethe. "Bremsformel für elektronen relativistischer geschwindigkeit". In: *Zeitschrift für Physik* 76.5-6 (1932), pp. 293–299.

[13] S. M. Seltzer and M. J. Berger. "Bremsstrahlung spectra from electron interactions with screened atomic nuclei and orbital electrons". In: *Nuclear Instruments and Methods in Physics Research Section B: Beam Interactions with Materials and Atoms* 12.1 (1985), pp. 95–134.

[14] M. J. Berger et al. *ESTAR, PSTAR, and ASTAR: Computer Programs for Calculating Stopping-Power and Range Tables for Electrons, Protons, and Helium Ions (version 1.2.3)*. National Institute of Standards and Technology, Gaithersburg, MD. URL: http://physics.nist.gov/Star (visited on 01/02/2020).

[15] S. Derenzo et al. *Scintillation Properties*. Lawrence Berkeley National Laboratory. URL: http://scintillator.lbl.gov/ (visited on 02/03/2020).

[16] *Scionix, Scintillation Crystals, website*. URL: https://scionix.nl/scintillation-crystals/ (visited on 09/07/2020).

[17] M. J. Berger et al. *XCOM: Photon Cross Section Database (version 1.5)*. National Institute of Standards and Technology, Gaithersburg, MD. URL: http://physics.nist.gov/xcom (visited on 01/30/2020).

[18] *Detector Assembly Materials*. Saint-Gobain Crystals. URL: https://www.crystals.saint-gobain.com/sites/imdf.crystals.com/files/documents/detector-assembly-materials_69673.pdf (visited on 02/03/2020).

[19] *Eljen Technology, website*. URL: https://eljentechnology.com/images/products/data_sheets/EJ-200_EJ-204_EJ-208_EJ-212.pdf (visited on 09/07/2020).

[20] *PHOTOMULTIPLIER TUBES AND ASSEMBLIES: For scintillation counting & high energy physics*. Hamamatsu Photonics K.K. URL: https://www.hamamatsu.com/resources/pdf/etd/High_energy_PMT_TPMZ0003E.pdf (visited on 02/11/2020).

[21] *PHOTOMULTIPLIER TUBES: Photomultiplier tubes and related products*. Hamamatsu Photonics K.K. URL: https://www.hamamatsu.com/resources/pdf/etd/PMT_TPMZ0002E.pdf (visited on 02/11/2020).

[22] *CAEN DT5730 Digitizer Manual*. URL: https://www.caen.it/products/dt5730/ (visited on 04/01/2020).

[23] J. Kónya and N. M. Nagy. *Nuclear and radiochemistry*. Elsevier, 2018.

[24] J. Webster. *The Measurement, Instrumentation, and Sensors: Handbook*. Electrical engineering handbook series. CRC Press, 1999. ISBN: 9783540648307. URL: https://books.google.fi/books?id=b7UuZzf9ivIC.

[25] P. H. Eilers. "A perfect smoother". In: *Analytical chemistry* 75.14 (2003), pp. 3631–3636.

[26] E. T. Whittaker. "On a New Method of Graduation". In: *Proceedings of the Edinburgh Mathematical Society* 41 (1922), pp. 63–75. DOI: 10.1017/S0013091500077853.

[27] P. H. Eilers and H. F. Boelens. "Baseline correction with asymmetric least squares smoothing". In: *Leiden University Medical Centre Report* 1.1 (2005), p. 5.

A Python Script for Estimation of the Light Collection Capability

Listing 1. Python script for the plotting of intrinsic efficiency as a function of minimum pulse amplitude

```
import numpy as np
import matplotlib as plt

Intrinsic_efficiency = []        #Create empty list
Calculated_incident_quanta = value #Define the number of beta particles
    incident on detector,i.e., 2*A*t*geometrical efficiency

for i in channels:               #Execute summation for every channel
    number
    Interval = y[int(i):len(x)]/Calculated_incident_quanta #Define
        summation interval
    Sum = np.sum(Interval)      #Execute sum up over interval
    Intrinsic_efficiency.append(Sum*100) #Add item to list

plt.plot(channels,Intrinsic_efficiency)    #Plot the intrinsic efficiency
    as a function of channel number
```

B Asymmetric Least Squares Method for Background Subtraction

Asymmetric least squares (ALS) is a digital filter used for smoothing data affected by signal or background noise. The ALS is especially suitable for baseline correction, i.e., background elimination in multiple types of spectroscopy techniques such as Raman and infrared spectroscopy. In this thesis, ALS is utilized for the removal of the background in the conversion electron energy region of the spectrum measured with the thin plastic scintillator. Background subtraction ensures easier Gaussian fitting of conversion electron peaks, which can be used for energy calibration of plastic scintillator setups.

ALS filter is a modified version of the Whittaker-Henderson smoothing filter that was originally introduced by E.T.Whittaker in 1923 [26] but was later modified by Paul Eilers in 2003 [25]. Whittaker-Henderson smoothing filter is used in image processing, analytical chemistry, etc. and is based on the penalized least-squares regression method where the function is fitted to the set of data points, and the best fit is found by minimizing the sum of squared residuals with an added penalty term. Whittaker-Henderson smoothing can be performed by minimizing the following penalized least squares function

$$S(z) = (y - z)^{\intercal} W (y - z) + \lambda z^{\intercal} D^{\intercal} D z, \tag{13}$$

where y is the measured spectrum, which is sampled at equally spaced bins, z is the smoothened spectrum, D is the difference matrix of first or higher-order, W is the weight matrix and λ is the penalty term. Minimizing the above function by taking a partial derivative in respect of z and setting the result to zero results in an explicit function for z

$$\begin{aligned} \frac{\partial S}{\partial z} &= -2W(y - z) + 2\lambda D^{\intercal} D z = 0, \\ z &= (W + \lambda D^{\intercal} D)^{-1} W y. \end{aligned}$$

In the ALS method, weight elements in the matrix W are assigned asymmetrically for positive and negative residuals as following

$$w_i = \begin{cases} p & y_i > z_i \\ 1-p & y_i < z_i \end{cases}$$

ALS smoothing can be easily implemented with most programming languages [27]. In this thesis, ALS was executed with a Python script that is shown below.

```
#Estimate background with asymmetric least squares
import numpy as np
from scipy import sparse

def background (y,lambda,p)
    iterations = 10
    L = len(y)
    D = sparse.diags([1,-2,1], [0,-1,-2], shape=(L, L-2))
    w = np.ones(L)
    for i in range(iterations):
        W = sparse.spdiags(w, 0, L, L)
        Z = W + lambda * D.dot(D.transpose())
        w = p * (y > z) + (1 - p) * (y < z)
    return z
```

The script takes the measured spectrum as a parameter along with user-defined penalty term λ and asymmetric weight p. In this thesis, λ and p parameter values depend on the light collection of the test setup. Poor light collection causes quenching of spectrum, i.e., spectrum squeezes to the lower energies. Now, a more squeezed spectrum requires a lesser smoothing factor and thus smaller values for λ and p parameters and vice versa for less quenched spectrum.

Fig. 52 shows a typical quenched ^{137}Cs spectrum measured with the thin plastic scintillator setup that has a poor light collection. As can be seen, the ALS method works well for background subtraction in the ^{137}Cs 662 keV conversion electron region and thus enables easier peak fitting.

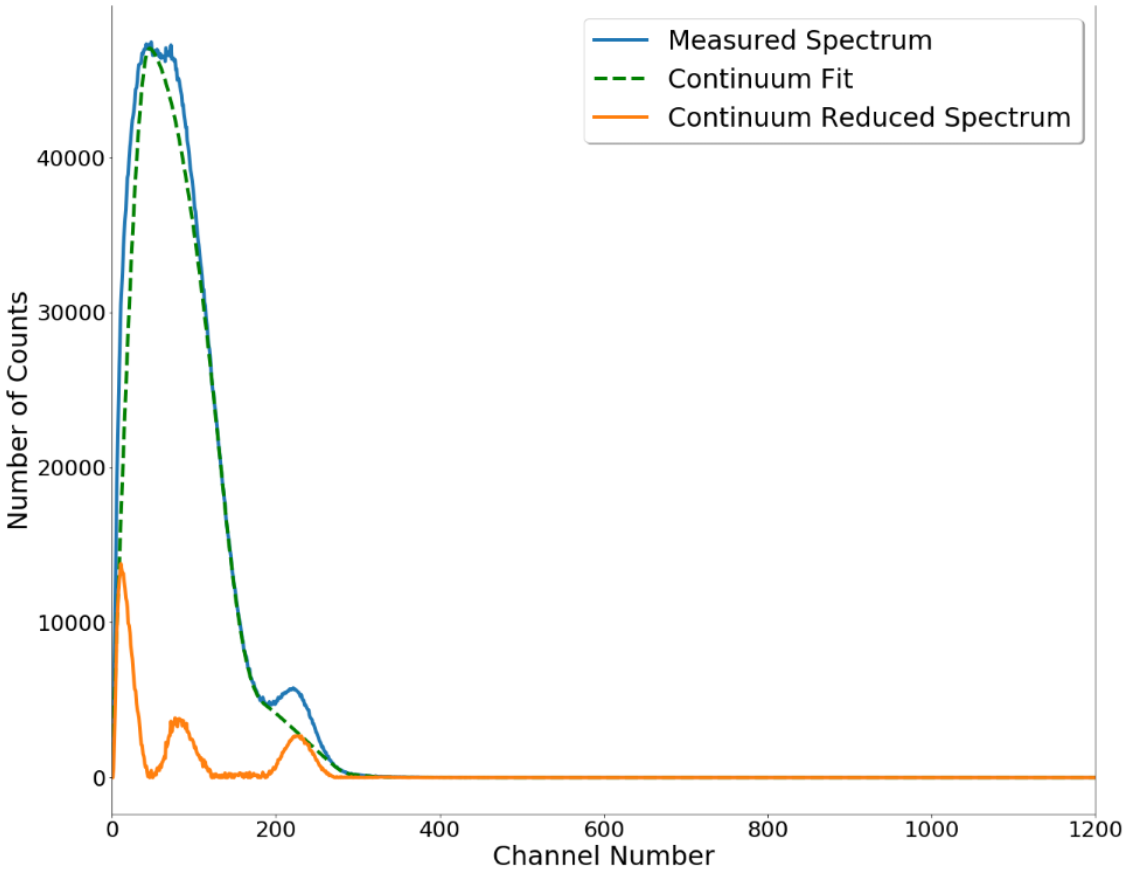

Figure 52. Example plot depicting the result of the asymmetric least squares method for background subtraction in the ^{137}Cs 662 keV conversion electron region. Parameters used in this plot were $\lambda = 34$ and $p = 0.000000001$.